# Trace element parameterisation for slab fluid composition from K-free oceanic crust

**Vili Boykova Grigorova**

**Supervisors:**

**Jeroen van Hunen**

**Pierre Bouilhol**

**Nicolas Riel**

A Dissertation presented for degree of

Master by Research




Department of Earth Science

University of Durham

England

May, 2017

*"The complacent manner in which geologists have produced their theories has been extremely amusing; for often, with knowledge (and that frequently inaccurate) not extending beyond a given province, they have described the formation of world with all the detail and air of eye-witnesses. That much good ensues, and that the science is greatly advanced, by the collision of various theories, cannot be doubted. Thus, new countries are explored, and old re-examined; facts come to light that do not suit either party; new theories spring up; and, in the end, a greater insight into the real structure of the earth's surface is obtained."*

Sections & Views, Illustrative of Geological Phaenomena

Henry Thomas De La Beche, (1830)

## Abstract

The geodynamical conditions of subduction zones make this tectonic environment essential for global geochemical cycles and for the heterogeneity of the Earth's mantle. A complex series of processes such as slab dehydration, melt/fluid percolation, sediment/mantle wedge melting and fractional crystallisation, is responsible for continental crust generation and the particular chemical signature of island arc basalts. Moreover, trace element signatures can be used as a proxy for the influence of each of these processes during the formation of island arc basalts. To quantify these signatures, it is necessary to use mineral–melt or mineral–fluid partition coefficients. While mineral–melt partition coefficients are well studied and used to identify different magmatic processes, slab–fluid interactions at different P-T-X conditions are poorly due to a lack of sufficient, integrated data on this subject.

An extensive compilation of experimental partition coefficient ($Di_{min/fluid}$) data for trace elements between a range of relevant K-free minerals and aqueous fluids was compiled in order to parameterise the partition coefficients at different temperatures. Most mineral–fluid partition coefficients have a negative correlation with temperature, where fluids become more enriched at higher P-T conditions in the subduction zone. The exception to this is zoisite, for which most of the trace element partition coefficients increase with increasing temperature, meaning larger concentrations of trace element are retained in zoisite.

The integration of partition coefficients in a combined geodynamical-thermodynamical subduction model allows prediction of the fluid trace element composition during mineral dehydration in a subduction process. This method was used to simulate the fluid composition resulting from K-free basaltic crustal dehydration in natural examples of a cold (Marianas) and a hot (Vanuatu) subduction zone. Generally, the fluids calculated in this work show enrichment in fluid-mobile (FM) elements and LILEs in comparison with REEs and HFSEs. Moreover, fluids released at shallow depth will be less enriched in trace elements in comparison with those released at greater depth.

Comparison of Ba/Yb and Ba/Th ratios of the fluids calculated here with arc basalts from the two natural subduction zones show similarities, which illustrates that fluids with a similar composition as those calculated in this dissertation were likely involved in the origin of the primitive IAB from these examples.

## List of Abbreviations

| | |
|---|---|
| ACT | Actinide (Th and U) |
| BAB | Back Arc Basalt |
| DMM | Depleted MORB Mantle |
| Di | Partition coefficient |
| FM | Fluid Mobile (Li and B) |
| HFSE | High Field Strength Element (Zr, Hf, Nb, Ta and Pb) |
| HREE | Heavy Rare-Earth Element (Tb, Dy, Ho, Y, Er, Tm, Yb and Lu) |
| IAB | Island Arc Basalt |
| LILE | Large – Ion Lithophile Element (Rb, Ba and Sr) |
| LREE | Light Rare-Earth Element (La, Ce, Pr, Nd, Eu and Gd) |
| MORB | Mid-Ocean Ridge Basalt |
| OIB | Ocean Island Basalts |
| PM | Primitive Mantle |
| PTM | Post-Transition Metal (Ga and Sn) |
| REE | Rare-Earth element (La, Ce, Pr, Sm, Nd, Eu, Gd, Tb, Dy, Ho, Y, Er, Tm, Yb and Lu) |
| TM | Transition Metal (V and Cr) |

## List of Tables

## List of Figures

## Table of Contents

# 1. Introduction

## 1.1 Geodynamic environment

Subduction zones are geodynamic environments where one tectonic plate subducts into the mantle below another (Figure 1). These environments are sites of earth global geochemical recycling, as they provide the return flow to the mantle from the atmosphere. Moreover, they are thought to be the site of the formation of most of the continental crust (van Huene & Scholl 1991; Rudnick 1995). During subduction, the oceanic plate (oceanic slab) is being metamorphosed, leading to its devolatilization and eclogitization (Tatsumi et al. 1986; Saunders et al. 1991; Manning 2004; Spandler & Pirard 2013). The $H_2O$ released from water-bearing minerals decreases the solidus of the mantle peridotite by ~200°C (Grove et al. 2006), causing partial melting of mantle wedge above the slab and creating magmas that will feed Island-arc systems, which are the building blocks of the continental crust (Tatsumi 1989; Hawkesworth et al. 1993; Stolper & Newman 1994; Grove et al. 2006; Spandler & Pirard 2013). Slab fluids and magma are the primary agents of chemical mass transport within a subduction system, and they generate the chemical characteristics of arc magmatism, and also recognized in the bulk continental crust. It is thus essential to constrain the geochemical signature of the slab derived-flux to better comprehend the resulting geochemical characteristics of subduction systems. Their characterisation will help for a better understanding of the geochemical and petrological evolution of continental crust, arc magma generation, associated volcanic hazards of subduction zones, and global $H_2O$ circulation (Iwamori 2004; Spandler & Pirard 2013, Ague 2014).

The magma generated in this environment has a distinct minor and trace element composition that differs from other tectonic settings. Numerous factors control the arc magma composition, which can be summarised as being the sum of a mantle wedge component and a slab component, comprising the sedimentary and/or igneous crust and the slab-mantle lithosphere (Peacock 1989; Hawkesworth et al. 1993; Poli & Schmidt 1995; Kimura & Yoshida 2006). Most magmas created in subduction zones are basaltic rocks, e.g. low–K tholeiites, calc-alkali basalts and shoshonites (Pearce & Cann 1973), with specific trace element characteristics. The trace element behaviour can deduce the regional magma source, tectonics settings and fractionation-contamination processes (Saunders et al. 1991). Stolz et al. (1996) discuss that high B/Be values provide evidence that the magmas result from a mantle melt that is modified by slab fluids. The low Ba/Th, Ba/Rb and Li/Rare-Earth Elements (REE) values in the arc magmas can be used as evidence for slab dehydration or the existence of phlogopite in the mantle region ( Elliott 2003; Pearce et al. 2005). High Th/La values represent the influence of slab fluids, and the low High Field Strength element (HFSE) content of IAB probably is inherited from fluids that were released from rutile-bearing assemblages (Elliott 2003; Pearce et al. 2005; Kimura & Yoshida 2006). Furthermore, high La/Nb and Th/Nb may result from sediments

dragged down by the subducting oceanic plate (Elliott et al. 1997; Plank & Langmuir 1998). IAB lavas are relatively depleted in HFSE compared to MORB or OIB, and enriched in Large-Ion Lithophile elements (LILE) and U in comparison with REE (Perfit et al. 1980; Edwards et al. 1991; Stolz et al. 1996; Plank 2005; Kimura & Yoshida 2006). The enrichment in LILE and depletion of HFSE can be explained by their origin from depleted peridotites that were enriched in LILEs by slab fluids (Ayers et al. 1997). There are many uncertainties about the influence of slab fluids on the formation of IAB magmas, and a better comprehension of the geochemical composition of these fluids is needed to provide new insight on this subject.

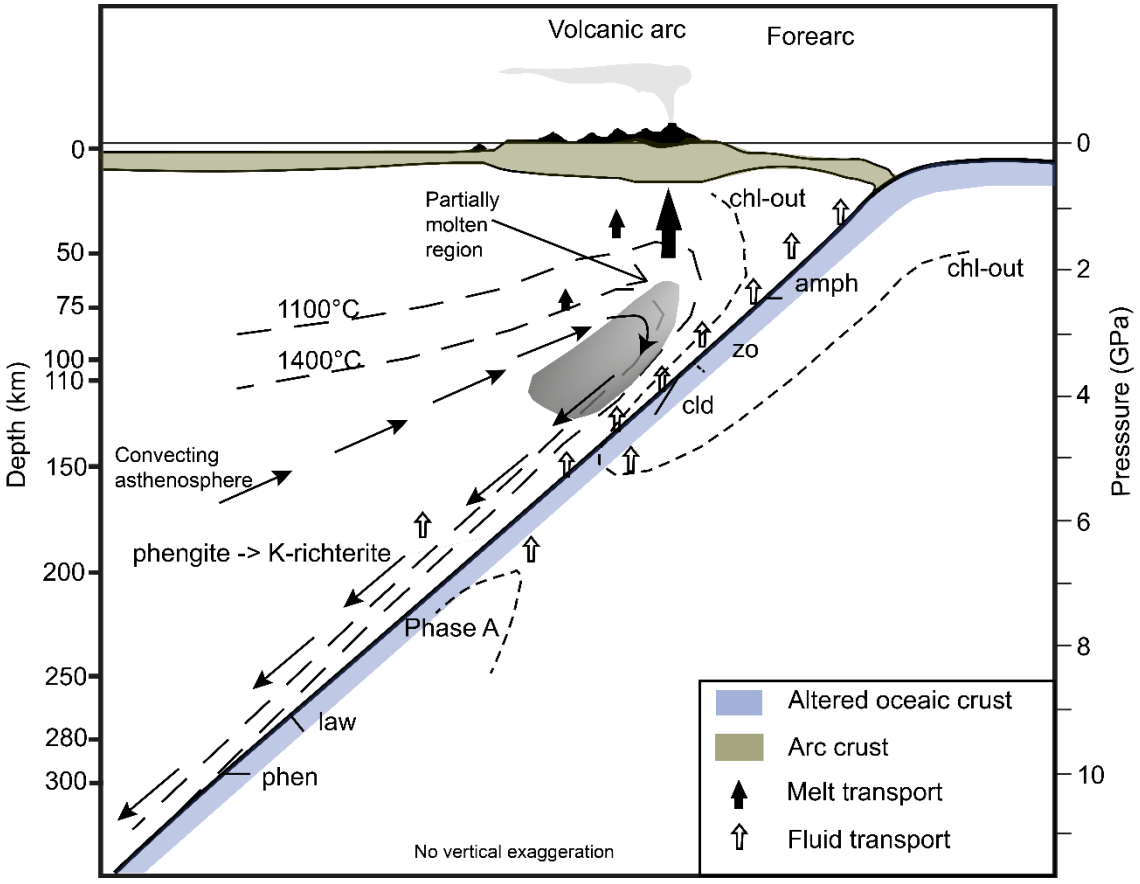


**Figure 1: Schematic representation of a cold subduction zone adapted from (Schmidt & Poli 1998).**

### 1.2 Water content and fluid transport within the subduction zone

The primary source of water, at depths below 40 km, is the breakdown of hydrous minerals such as zoisite, lawsonite, phengite and chloritoid (Saunders et al. 1991; Bebout 1991; Poli 1993; Hermann 2002; Feineman et al. 2007; Bloch et al. 2014). In mafic systems, the breakdown reactions are continuous, releasing fluids over a large range of PT conditions (Poli & Schmidt 2004). In basaltic and andesitic rocks, the amphibole (Amph) breakdown reaction can produce other hydrous phases like lawsonite, chloritoid or zoisite-clinozoisite. The following reactions from Poli & Schmidt (2004) show the transformation of one hydrous mineral phase to another between 300 and 1000˚C.

lawsonite + kyanite + grossular + coesite ⇄ zoisite (1.1)

zoisite ⇄ anorthite + grossular + corundum + $3H_2O$ (1.2)

Reaction (1.1) defines the upper-pressure stability of zoisite without free water in the system. In addition, reaction (1.2) represents the breakdown of zoisite under high temperature and low-pressure conditions.

At relatively low pressure and temperature (2 GPa and under 400°C), a basaltic system can retain more than 4 wt.% $H_2O$. Beyond 15 km depth, the oceanic crust enters into blueschist facies, with a capacity to retain up to 6 wt% $H_2O$ (Schmidt & Poli 2013). van Keken et al. (2011) calculated the average flux of water during ongoing subduction. They estimated that from the total water input into a subduction zone, in case of 2 wt% of $H_2O$ in the first 2 km of the uppermost mantle, 7% is in sediments, 62% in oceanic crust and 31% in the mantle wedge under the overriding plate. At 15 km depth within the subducting lithosphere, the global flux of water entering the subduction zones is $1.0x10^9$ Tg/Myr. From this amount, $0.32x10^9$ Tg/Myr are released between 15 and 100 km, $0.14x10^9$ Tg/Myr from 100 to 150 km and $0.2x10^9$ Tg/Myr in depths between 150 and 230 km. Beyond 230 km, the total flux of water entering the mantle is $0.34x10^9$ Tg/Myr estimated by van Keken et al. (2011) or $0.7x10^9$ Tg/Myr estimated by Magni et al. (2014). The range of depths where these fluids are released is large, and the chemical composition of the fluids will be influenced not only by the mineral assemblages (which generate the fluids) but also other factors such as pressure and temperature (which control the solubility and partition coefficient (*Di*) (see section 1.3)), fluid migration/propagation velocity and trace element characteristics.

The aqueous fluid migration through the oceanic crust and its interaction with the ductile mantle is a subject that needs to be analysed in more detail. Under subduction zone conditions, the fluids have a density of less than half of the surrounding rocks and will have a tendency to migrate upward (Peacock 1989), but it is unclear how they percolate through the rock. Ague (2013) and Connolly (2010) propose that the fluid transport is occurring by porous waves, while Zack & John (2007) and Engvik et al. (2001) suggest the main mechanism of transport to be through channels. The first school of thought argues that the migration of fluids occurs through self-propagation, i.e. the overpressure of the fluids creates or uses pre-existing fractures to migrate through impermeable domains (Connolly 2010; Connolly & Podladchikov 2014) and is controlled by crustal permeability (Connolly 2010). The fluid released from the minerals is largely trapped in the pores of the rock, where geochemical reactions between the fluid and the minerals will take place. Consequently, the fluid will be in equilibrium with the minerals at their boundaries (Iwamori 1998). The second school of thought proposes that the low permeability of the subducted oceanic crust and the high dihedral angles between the fluids and the minerals are not suitable for porous flow (Zack & John 2007).

During dehydration, the interstitial pressure increases and this will reduce the effective stress (Engvik et al. 2001) and create instant channel flow. In this case, non-equilibrium processes will control the fluid-mineral interaction ( Engvik et al. 2001; Zack & John 2007; Ikemoto & Iwamori 2014).

### 1.3 Physical and chemical factors that control the fluid composition

With increasing pressure and temperature, hydrous minerals start to break down and release aqueous fluids. Breeding & Ague (2002) estimated fluid flux of ~$10^4$-$10^5$ $m^3_{(fluid)}$ $m^{-2}_{(rock)}$ out of the subducted oceanic crust into the Otago Schist acretionary prism. During its transfer, the fluid will experience chemical exchange of elements with the surrounding rock, thereby changing its initial composition. There is no consensus whether the fluid has or has not a Charge and Radius Controlled (CHARAC) behaviour. CHARAC behaviour occurs when the geochemical reactions of an element are controlled only by its ionic charge and radius. Bau (1996) described the fluid as having non-CHARAC behaviour, contrary to melt systems. However, Stalder et al. (1998) argue that CHARAC behaviour of fluids may start to occur with the increase of PT conditions. Major elements such a Cl, Si and Na may influence the miscibility of the fluids (Manning 2004; Schmid & Poli 2013).

$$\mathrm{Si0_2} + \mathrm{H_2O} \rightleftarrows \mathrm{H_4SiO_4} \tag{1.3}$$

Reaction 1.3 shows that the monomer species $Si0_2$ can be dissolved in water at high PT condition (Brady 1953; Laudise & Ballman 1961; Walther & Helgeson 1977; Zotov & Keppler 2000). Still, high $SiO_2$ concentrations in the fluid only have a minor effect on mineral–fluid partition coefficient (Stalder et al. 1998). Banks et al. (1994) performed a study on inclusions from water-rich phases, exsolved from granitic melts, and concluded that the REE content of the fluid is independent of the salinity of the inclusions. Major and minor elements in the crust such as Si, Na and Cl are the dominant solutes in deep fluids (Manning 2004), but their abundance in fluids and influence on partition coefficients is poorly understood. In general, elements with large ionic radii are more compatible with aqueous fluids during dehydration (Tatsumi et al. 1986). Therefore, fluids have a LILE/HFSE ratio above 1 (Green and Adam 2002). HFSEs are incompatible with the fluid, the Nb/Ta ratio is above the mantle value, and, at high temperatures, Sr prefers the fluid over clinopyroxene (Cpx) (Stalder et al. 1998). The capacity of aqueous fluids to transport incompatible elements is used to explain the large quantities of incompatible elements in some mantle-derived magmas and xenoliths (Adam et al. 1997).

The trace element composition of aqueous fluids can be calculated using the partition coefficient (*Di)* between minerals and fluids under equilibrium conditions:

$$Di = \frac{X_{min}}{X_f} \tag{1.4}$$

where $X_{min}$ is the concentration of one element in the mineral and $X_f$ is the concentration of the same element in the fluid.

The concept of partition coefficients was proposed by chemist Berthelot (1872). He found that when an object is immersing in a solution of two solvents, the solvents will dissolve it simultaneously and partitioning it between the two of them, independently of the relative volume of the solvents. The amount of dissolved body in some volume of solvents is a constant and he named it *coefficient de partage* (partition coefficient). Twenty years later, von Nernst (1891) defined the partition coefficient as independent of the volume and concentration of the solvents. However, at the moment, there are still two major shortcomings in using partition coefficients to calculate the distribution of trace elements between fluids and minerals. The first is the uncertainty of *Di* between minerals and fluids, which is larger than the uncertainty of *Di* between minerals and melts, due to the difference of the number of conducted studies. The second is that the *Di* depends on many different parameters, such as the acidic composition of the fluid phase, pressure, temperature, oxygen fugacity and even solid solutions of some minerals (McIntire 1963). Nonetheless, the partition coefficient is a powerful tool, and geologists are using it for geologic thermometry and barometry, criteria of equilibrium isotherms and isobars in metamorphic terranes, the trace element distribution during crystallisation or separation of an aqueous phase from the magma, composition of ore-forming fluids, the origin of granite bodies, as guides for mineral deposits, and for the determination of paleosalinity (McIntire 1963).

During ongoing subduction, the first elements that are released from the slab to the mantle wedge are LILEs and light rare earth elements (LREEs), which are compatible in hydrous phases like amphiboles and phlogopites (Kogiso et al. 1997). The HFSEs are incompatible with hydrous fluids and relatively insoluble in hydrous melts, so they remain in the slab until larger depths (Saunders et al. 1991). The quantity of these elements is controlled by the mineral assemblage of altered oceanic crust (Table 1). Even minor and residual phases are important, since, e.g., rutile (Rt) will control the HFSE budget.

Potassic hydrous phases such as phengite and biotite in sediments greatly control the geochemical composition of the sediment-derived fluids (Schmidt & Poli 2013). Sediments can retain water until 6 GPa if phengite does not break down completely (Schmidt & Poli 2013). However, there is not enough available data to create a temperature-dependent regression for the calculation of partition coefficients between these minerals and the aqueous fluids. For this reason, the influence of the sediments is not addressed in the calculation of the bulk partition coefficients of the slab fluids in this dissertation.

| Mineral | Hosted elements | Papers |
|---|---|---|
| amphibole | HREE, Ta, Nb, Sr, Zr and LILE | Ionov & Hofmann (1995), Adam & Green (2006), Davidson et al. (2007) and Lesnov (2010) |
| apatite | REE, Y, P, Sr and Pb | Hermann (2002), Miller et al. (2007), El Korh et al. (2009) and Belousova et al. (2002) |
| clinopyroxene | LREE, Li, Sc and V | Miller et al. (2007), Zack et al. (2002) and Woodland et al. (2002) |
| epidote | REE, U, Th, Sr and Pb | Spandler et al. (2003), Miller et al. (2007) and El Korh et al. (2009) |
| garnet | Y and HREE | Spandler et al. (2003), Miller et al. (2007) and El Korh et al. (2009) |
| lawsonite | REE, Pb and Sr | Spandler et al. (2003) |
| phengite | LILE | Hermann (2002), Spandler et al. (2003) and Miller et al. (2007) |
| rutile | Ti, Nb and Ta | Miller et al. (2007), Spandler et al. (2003) and El Korh et al. (2009) |
| zircon | Zr, U and Hf | Miller et al. (2007) and Spandler et al. (2003) |

**Table 1: A summary of the main crustal minerals in a subducting slab. The second column describes the trace elements hosted by each mineral and in the third column contains the studies from which this information was taken.**

Hydrous fluids from subducted oceanic crust are responsible for generating the typical fluid-mobile element enrichment of arc lavas, while supercritical fluids or hydrous melts from sediments and oceanic crust are responsible for fluid-immobile element enrichment (LREE and Pb, Th and U) ( Xiao et al. 2012; Cao et al. 2016). The supercritical condition is a physical state where silicate melts and aqueous fluids become indistinguishable from each other. This condition occurs above the second critical end point, where a melt or fluid is called a supercritical fluid (Wyllie & Tuttle 1960; Mibe et al. 2004; Hermann et al. 2006). The intersection between the critical curve (crest of immiscibility between fluid and melt) and the $H_2O$-saturated solidus is the location of the second critical end point (Schmidt & Poli 2013). In felsic rocks, the second critical end point is located at 2.5 - 3.5 GPa and ~700˚C, and in a peridotite-$H_2O$ system at 3.8 GPa and ~1000˚C (Mibe et al. 2007). Schmidt et al. (2004) determined for MORB rocks, that around 850˚C and above 3.5 GPa the first fluid-saturated melts start to be generated. The fluid content in the melts decreases with temperature and never exceeds 15 wt% of $H_2O$ (Hermann & Green 2001). Breakdown of phengite in K-enriched MORB beyond the second critical end point (~1050˚C and 5-6 GPa) will create supercritical fluids (Schmidt et al. 2004; Xiao et al. 2012), which will be enriched in Ba, K, Cs and Rb (Xiao et al. 2012). In this dissertation, the PT conditions used to calculate mineral–fluid partition

coefficients are below the formation of hydrous melts or supercritical fluids, i.e. temperature and pressure are below 940˚C and 4 GPa, respectively.

### 1.4 Thesis aim and outline

Subduction zones control most of the trace element and $H_2O$ recycling into the mantle and arc magmas. Quantifying the trace elements that are transported into the mantle wedge by the slab fluids and those retained by the oceanic slab until a transition zone will help to understand this recycling process better. This dissertation aims to parameterise the trace element partition coefficient behaviour for key minerals involved in the slab crustal devolatilization, for which enough data exists to form temperature-dependent regressions. These minerals are amphibole, clinopyroxene, garnet (Gt), lawsonite (Law), rutile and epidote (Ep). Such parameterisation can be used in subduction zone geochemical models to calculate the composition of fluids resulting from the dehydration K-free basaltic oceanic crust. The purpose of this work is, therefore, to provide quantitative models for the calculation of the trace element partition coefficients between a rock and aqueous fluids (without melt present in the system) and to calculate the composition of the fluids that metasomatizes the mantle wedge above the subducting oceanic plate.

Chapter 2 contains a detailed explanation of the methodology used for the calculation of the partition coefficients, including a table with a list of incorporated literature that contains measured mineral-fluid partition coefficient data.

In Chapter 3, different temperature-dependent regressions are generated to calculate the trace element partition coefficients between six minerals and fluid. In addition, tables with the coefficients used in the regression for each mineral and trace elements, and their respective coefficients of determination ($R^2$) can be found in this chapter.

In Chapter 4, these temperature-dependent partition coefficients are used in the Rayleigh distillation equation (Ayers 1998) for the calculation of possible fluid compositions. The parameterisations for the calculation of *Di* are applied to the conditions of a real subduction zone, and results for two different environments are compared: a cold subduction zone (Marianas) and a hot subduction zone (Vanuatu). This approach is used to study the evolution of the fluid compositions during the subduction process.

In this dissertation, the term fluid will be used to refer to aqueous fluids and the term liquid for magma.

## 2. Parameterising the Partition Coefficient

### 2.1 Introduction

During the last decades, estimation of mineral-fluid partition coefficients values have improved significantly, due to the development of new analytical and experimental tools. The existence of measured *Di* values is improving our understanding of fluid-rock interaction in metamorphic processes. Due to the lack of data on this subject in the past, the mineral–fluid partition coefficient was often considered to be equal to solid–melt or even to solid–solid partitioning. There is still disagreement over which factors have a predominant control on solid-fluid partition coefficients: the crystalline phase of the minerals or the temperature and pressure conditions (Stalder et al. 1998; Martin et al. 2011). Here, the various proposed methods for quantifying the chemical interaction between fluid and rocks are discussed.

Hollister (1966) published one of the first studies where the distribution of trace elements in minerals, $Di_{bulk}$, was measured and modelled through the Rayleigh fractionation process:

$$X_{Min}^{A} = Di_{bulk}^{A} * X_{rock}^{A} * \left(1 - \frac{W^{G}}{W^{O}}\right)^{\left(Di_{bulk}^{A}-1\right)} \quad (2.1)$$

where $X_{Min}^{A}$ is the concentration of element *A* in a mineral; $X_{rock}^{A}$ is the bulk concentration of the same element in the rock; $W^{G}$ is the total weight proportion of the mineral, and $W^{O}$ is the initial weight of the system. Rayleigh (1896) demonstrated that, if two gases are mixed under vacuum conditions, the diffusion will create conditions of equilibrium, initially at the border between the porous walls of the gases and afterward throughout the entire system. Nowadays, Rayleigh equations are applied to progressive dehydration, rock-fluid interactions, partial melting, and fractional crystallisation processes. Equation 2.1 can be applied to metamorphic environments and indirectly specifies the trace element alteration in the minerals by the metamorphic fluids. In this case, the results of fluid-rock interaction can be observed in the minerals, but does not give direct information about the fluid composition.

Tatsumi et al. (1986) used the element mobility as an alternative method to calculate the fluid composition. They performed laboratory experiments, at 850°C and 1.2 GPa, on the element mobility to understand their compatibility with the fluid phase:

$$M = \frac{R_{x}^{STM} - R_{x}^{RP}}{R_{x}^{STM}} * 100\ (\%) \quad (2.2)$$

where $R_x^{STM}$ is the ratio of element $X$ over Nb originally present in the system and $R_x^{RP}$ is the same ratio lost during the dehydration. Equation 2.2 does not directly describe the quantity of trace elements that move into the fluid and how much of it remains in the rock.

During recent years, some key papers with clinopyroxene/garnet–fluid partitioning data were published, thereby considerably increasing the database on this subject. The experimental work of Brenan et al. (1994), Brenan et al. (1995), Adam et al. (1997), Ayers et al. (1997) and Stalder et al. (1998) were pioneering in the determination of *Di* at high PT conditions. However, these studies quantify the amounts of trace elements in the fluid at more elevated temperature conditions (temperature above 900˚C) than dehydration temperatures in the subducted oceanic crust (Martin et al. 2011). The partition coefficient can vary significantly with temperature, so the *Di* between a certain mineral and a fluid determined at 900°C is not necessarily applicable to partitioning at lower temperatures. This variation of the *Di* could be due to the changes of solubility or major composition of the $H_2O$ or changes in the mineral structure. To circumvent such problems, it is necessary to express the *Di* as a function of temperature. For example, Caciagli et al. (2011) present experimental data on lithium fractionation between clinopyroxene-fluid and olivine-fluid for 800-1100˚C at 1 GPa, and quantitatively predict lithium partition coefficients for these two minerals:

$$log_{10}(Di_{Li}^{cpx/fluid}) = -7.3\ (\pm 0.5) + 7.0\ (\pm 0.7) * 1000\ /\ T \quad (2.3)$$

$$log_{10}(Di_{Li}^{ol/fluid}) = -6\ (\pm 2) + 6\ (\pm 2) * 1000\ /\ T \quad (2.4)$$

where $T$ is temperature in Kelvin.

Often, *Di* values are only available for a set of minerals, and one way to calculate a missing mineral–fluid partitioning is by establishing a multiplication relationship using a mineral-mineral partition coefficient and a known mineral–fluid partition coefficient (Equation 2.5), such as for clinopyroxene (Zack et al. 1997; Marschall et al. 2007):

$$Di_{\ mineral/fluid} = Di_{clinopyroxene/fluid} * Di_{mineral/clinopyroxene} \quad (2.5)$$

In the Equation 2.5, the value of the partition coefficient between one specific mineral and the fluid can be calculated from others partition coefficients, more specifically on the *Di* between a clinopyroxene and fluid and the *Di* between this mineral and a clinopyroxene. Moreover, each of these partition coefficients will be dependent on several other factors such as the PT conditions, the mineral assemblage of the rock and the initial trace element composition of the bulk rock. These

factors are difficult to be constrain or can vary significantly in most of the cases, i.e. the determination of the exact value of pressure or temperature at which the mineral-clinopyroxene partition coefficient occurs it is extremely difficult. In conclusion, when Equation 2.5 is used to calculate the partition coefficient between a mineral and the fluid, the final *Di* will be influenced by the other partition coefficients and the inaccuracies related to the determination of these partition coefficients.

One of the methods proposed for the calculation of the mineral–fluid partitioning is lattice strain theory (LST). LST is a quantitative model that predicts *Di* by using the experimentally determined partition coefficient ($D_0$) of an element with ionic radius $r_0$ that would fit perfectly in the crystal structure. Blundy & Wood (1994) adapted Brice's (1975) work to calculate the pressure, temperature, and composition dependence of trace element partition coefficients between magmas and minerals. The lattice strain is a measurement of the lattice displacement in the crystal structure. A pseudo-parabolic variation of the mineral–melt partition coefficient is observed when plotted against the ionic radius (Figure 2-a), due to the strong influence of the lattice strain over the mineral–melt partitioning (Nagasawa 1966; Brice 1975; Blundy & Wood 1994; Green et al. 2000). This pseudo-parabolic behaviour is not observed when the clinopyroxene–fluid partition coefficient is plotted against the ionic radius of REE and trace elements with $2^+$ charge (Figure 2-b), which argues against the usage of LST for the calculation of mineral-fluid *Di* values. Figure 2-c show that although the divalent cations have a pseudo-parabolic behaviour when plotted against the ionic radius, this behaviour is not observed with cations with $1^+$ and $3^+$ charges. Moreover, Martin et al. (2011) argued that LST could be used only to predict the *Di* between lawsonite and fluid for divalent cations (except Ba), but that it does not work well for REE due to the weak fractionation between REEs. For lawsonite-fluid partition coefficients, only the divalent cations of zoisite-fluid *Di* show a pseudo-parabolic behaviour when plotted against the ionic radius (Figure 2-d). Furthermore, Feineman et al. (2007) notice the weak fractionation of rare earth elements in zoisite and argue that LST cannot be reliably used for predicting the *Di* between this mineral and a fluid. Unlike predicted by the LST, the effect of variation of the ionic radius on the mineral-fluid partitioning is less important than the effect of variation of temperature or pressure over realistic ranges. Therefore, LST is not used for the calculation of the mineral–fluid partition coefficients in this dissertation. However, despite the weak affinity between the ionic radius and the *Di*, this relationship was used to calculate the *Di* values for REE*s* for which experimentally determined *Di* values are absent.

In the remaining part of this chapter, the used methodologies for the formulation of temperature-dependent linear regression are explained. The approach taken by Caciagli et al. (2011) for Li is extended for the calculation of *Di* values for other trace elements.

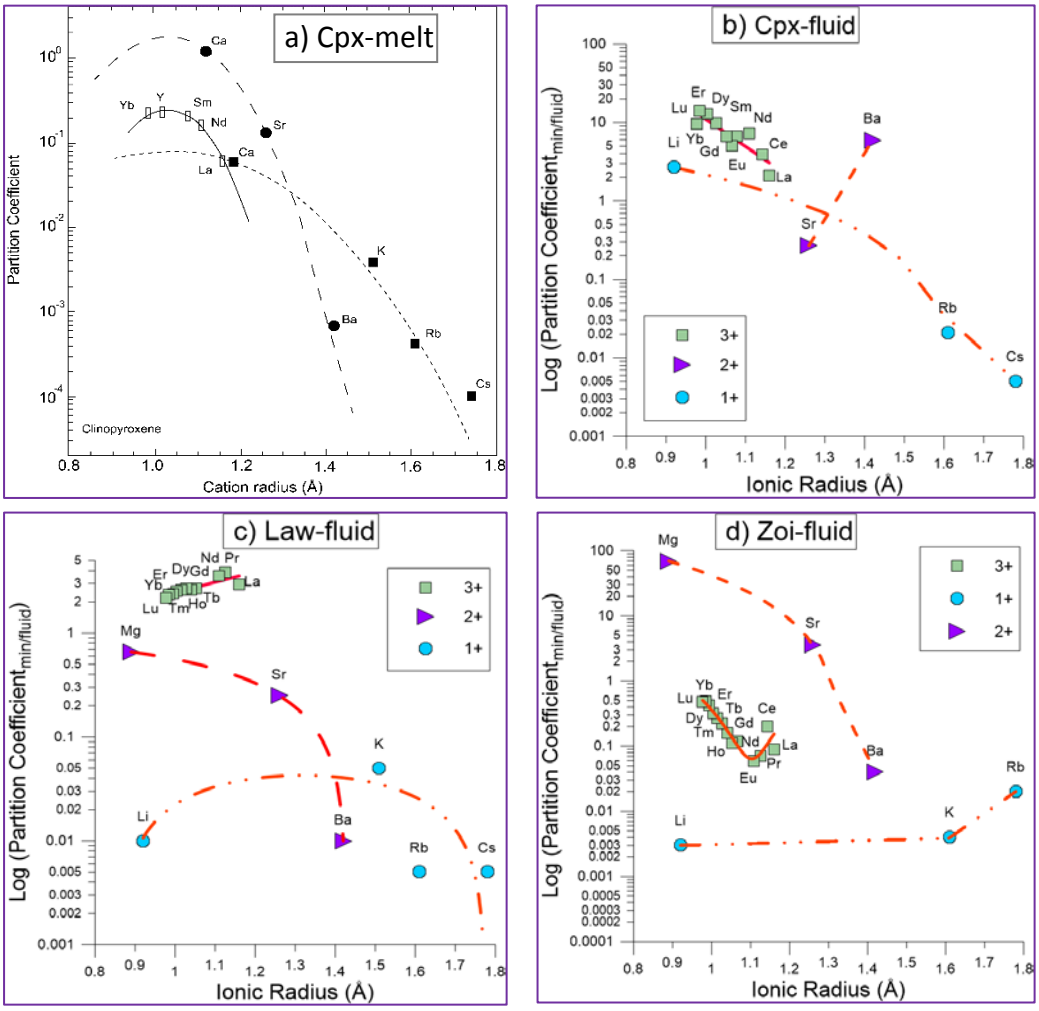


**Figure 2: Onuma diagrams contrasting two different REE partition coefficient behaviours versus the radius, for 3+ valency elements: (a) diagram for clinopyroxene-melt from (Wood & Blundy 1997); b) diagram for clinopyroxene–fluid partition coefficient; (c) diagram for lawsonite–fluid partition coefficient; and (d) diagram shows schematically the trace element behaviour of zoisite–fluid partition coefficient.**

## 2.2 Methodology

The lack of information on mineral–fluid partitioning of important hydrous minerals such as mica and chlorite makes it difficult to quantify their contribution to the trace element composition of fluids. While chlorite is a minor hydrous phase in the altered oceanic crust, micas are one of the most common hydrous minerals in the subducting basaltic crust and the overlying sediments. Although sediments can retain water up to 11 GPa (Schmidt & Poli 2013), thus greatly influencing the composition of the fluid in equilibrium with these minerals (Schmidt & Poli 2013), there is not enough available data for creating a consistent regression for the calculation of partition coefficients between sediment minerals and aqueous fluids. Because *Di* data for K-bearing phases is absent, a K-free basaltic crust was used in this dissertation to model subduction zone fluids.

Figure 3 shows a PT diagram of the mineral stability in subducting oceanic crust and the maximum water content for some of the phases. Overall, usable trace element partitioning information exists for six minerals: amphibole, clinopyroxene, garnet, lawsonite, rutile and zoisite,

and these are the minerals for which partition coefficients are parameterised in this dissertation. These minerals cover most of the important phases present within the subducting crust. Three main steps are performed to construct the *Di* parameterisation using a regression technique. The first step involves selecting the relevant *Di* data from the bibliography. The next step is to understand if some linear relationship between the ionic radius and the REE exists. If such a relationship exists, it is used to extrapolate *Di* values for some of the REE. The third and last step is the actual calculation of a temperature dependent regression and the parameterisation of the trace element *Di* behaviour as a function of temperature. A detailed explanation of each step is given below

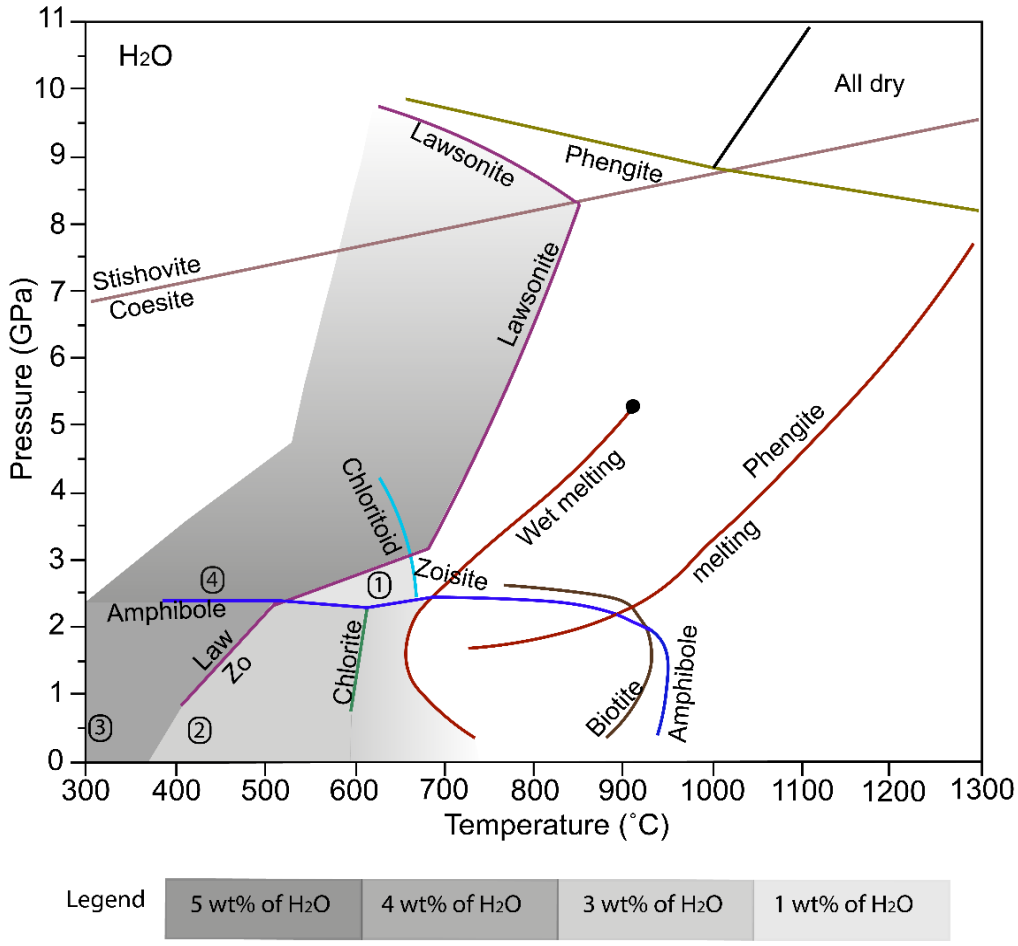


**Figure 3: PT diagram of the stability field of hydrous minerals in the oceanic crust (adapted from Schmidt & Poli, 2013). The shaded areas represents the maximum amount of water (adapted from Hacker, 2008). The area marked with (1) contains around 1 wt% of $H_2O$, the zone marked with (2) represents 3 wt% of $H_2O$, and areas with (3) and (4) contain 5 and 4 wt% of $H_2O$, respectively.**

**Step 1**: Data Selection

Table 2 contains relevant data for the determination of mineral-fluid partition coefficients of these minerals. Most of the studies report laboratory experiments with a specific mineral assemblage and at specific PT conditions. In general, these studies focus on the trace element interaction between the minerals and a fluid at a range of temperatures. Few of the papers consider the influence of solutes (HCl, NaCl and F) in the fluid or the influence of pressure on the *Di*. The used mineral assemblage in these studies is also considered. Studies, where the *Di* was measured in a simple mineral assemblage (composed of one or two minerals) are preferred over those with more complex systems, due to the existence of fewer variables in the system and the better control of the all factors that can influence the *Di*. The initial composition of the fluid is also an important criterion because the *Di* can vary with its acidic composition (McIntire 1963), so only experiments with pure water as fluid are used for all minerals, except for orthopyroxene and olivine (Appendix II and I, respectively). For these two minerals, 90% of the experiments were performed with some solute in the fluid, but in this study, the solutes were not taken into account.

Only data for experiments up to 900˚C and 4 GPa are used for the *Di* prediction, and mineral–fluid partitioning data above these conditions were discarded because such conditions are most likely above the second critical end point, and therefore probably dealt with supercritical fluids. From the 16 papers with mineral-fluid partition coefficient used in this dissertation, only 5 papers contain the pressure effect on the *Di* at pressures different than the 2 GPa (Table 2, column 5), i.e. Ayers et al. (1997) measured the partition coefficient at 2 and 3 GPa; Stalder at al. (1998) performed the experience at 3, 4, 4.5, 5 and 5.7 GPa; Green & Adam (2003) determined the *Di* at 3GPa; Caciagly et a. (2001) measured the partition coefficient at 1 GPa; and finally Kessel et al. (2005) measured the *Di* at 4 and 6 GPa. The experiments contain different starting compositions (Table 2, column 3), but the range of compositions is not sufficiently wide to use them in the parameterisation of the partition coefficients. Another factor that can influence the partition coefficient is the composition of the initial fluids. Most of the studied use pure water as the initial composition of fluids. Only 5 of the papers studied the influence of solutes, such as HCl, NaCl and F over the partition coefficient. Due to the limited number of experiments which involve solutes in the fluid, this factor was not parameterised. The only factor that can be parameterised reliably for all minerals is the temperature.

| Mineral | Paper | Starting Material | T | P | Nº exp. with Pure water | Nº exp. with Mixture |
|---|---|---|---|---|---|---|
| Amph | Brenan et al. (1995) | Garnet + Diopside | 900°C | 2 GPa | 10 | 5 |
| | Adam et al. (1997) | Basanite | 900, 1000 and 1100°C | 2 GPa | 6 | 2 |
| | Zack et al. (2002) ▪ | Metabasalts | 650°C | 2 GPa | - | - |
| | Fabbrizio et al. (2013) | Peridotite | 900, 1000, 1100 and 1300°C | 2 GPa | - | 18 |
| Cpx | Brenan et al. (1995) ▪ | Garnet + Diopside | 900°C | 2 GPa | 10 | 5 |
| | Ayers et al. (1997) | Peridotite | 900, 1050, 1000 and 1100°C | 2 and 3 GPa | 17 | - |
| | Adam et al. (1997) | Basanite | 900, 1000 and 1100°C | 2 GPa | 6 | 2 |
| | Brenan et al. (1998) ▪ | Basalts | 900°C | 2 GPa | 4 | 1 |
| | Stalder et al. (1998) | SMAS | 900, 1000, 1100 and 1200°C | 3, 4, 4.5, 5 and 5.7 GPa | 19 | 2 |
| | Green & Adam (2003) | Oceanic tholeiite | 650 and 700°C | 3 GPa | 6 | - |
| | Kessel et al. (2005) ▪ | A K-free average MORB | 700, 800, 900, 1000 and 1200°C | 4 and 6 GPa | 8 | - |
| | Caciagli et al. (2011) | Clinopyroxen, olivine and plagioclase | 800, 900, 1000, 1100 and 1200 °C | 1 GPa | 32 | - |
| | Fabbrizio et al. (2013) | Peridotite | 900, 1000, 1100 and 1300°C | 2 GPa | - | 18 |
| Gt | Brenan et al. (1995) ▪ | Garnet + Diopside | 900°C | 2 GPa | 10 | 5 |
| | Ayers et al. (1997) | Peridotite | 900, 1050, 1000 and 1100°C | 2 and 3 GPa | 17 | - |
| | Adam et al. (1997) | Basanite | 900, 1000 and 1100°C | 2 GPa | 6 | 2 |
| | Brenan et al. (1998) ▪ | Basalts | 900°C | 2 GPa | 4 | 1 |
| | Stalder et al. (1998) | CMAS | 900, 1000, 1100 and 1200°C | 3, 4, 4.5, 5 and 5.7 GPa | 19 | 2 |
| | Green & Adam (2003) | Oceanic tholeiite | 650 and 700°C | 3 GPa | 6 | - |
| | Kessel et al. (2005) ▪ | A K-free average MORB | 700, 800, 900, 1000 and 1200°C | 4 and 6 GPa | 8 | - |
| | Fabbrizio et al. (2013) | Peridotite | 900, 1000, 1100 and 1300°C | 2 GPa | - | 18 |
| Law | Marschall et al. (2007) | Metamorphic rocks | 900°C | 2 GPa | - | - |
| | Brenan et al. (1998) | Basalts | 900°C | 2 GPa | 4 | 1 |
| | Green & Adam (2003) | Oceanic tholeiite | 650 and 700°C | 3 GPa | 6 | - |
| | Martin et al. (2011) ▪ | Dehydrated lawsonite | 650 and 700°C | 3 - 3.5 GPa | 2 | - |
| Ol | Brenan et al. (1995) ▪ | Garnet + Diopside | 900°C | 2 GPa | 10 | 5 |
| | Ayers et al. (1997) | Peridotite | 900, 1050, 1000 and 1100°C | 2 and 3 GPa | 17 | - |

| | | | | | | |
|---|---|---|---|---|---|---|
| | Caciagli et al. (2011) ▪ | Clinopyroxen, olivine and plagioclase | 800, 900, 1000, 1100 and 1200 °C | 1 GPa | 32 | - |
| | Fabbrizio et al. (2013) ▪ | Peridotite | 900, 1000, 1100 and 1300°C | 2 GPa | - | 18 |
| Opx | Ayers et al. (1997) | Peridotite | 900, 1050, 1000 and 1100°C | 2 and 3 GPa | 17 | - |
| | Garrido et al. (2000) ▪ | Basanite | 1080, 1100, 1160, 1200 and 1220°C | 2, 3, 4, 6 and 7.5 GPa | - | - |
| | Fabbrizio et al. (2013) ▪ | Peridotite | 900, 1000, 1100 and 1300°C | 2 GPa | - | 18 |
| Rt | Brenan et al. (1994) ▪ | Rutile | 900, 1000 and 1100°C | 1 and 2 GPa | 12 | 3 |
| Zoi | Brunsmann et al. (2001) ▪ | Metabasites | 500 and 550°C | 0.6 GPa | 6 | - |
| | Feineman et al. (2007) ▪ | Zoisite | 750, 800 and 900°C | 2 GPa | 4 | - |
| | Martin et al. (2011) ▪ | Dehydrated lawsonite | 650 850°C and | 3 GPa | - | - |

**Table 2: A compilation of studies that report partition coefficients for given rock composition, P and T conditions of the experimental procedures, and the fluid composition. The last two columns contain the number of experiments in which pure water or mixture of pure water and some acid were used. The models for the prediction of partitioning behaviour in this dissertation are using the data from the papers marked with purple squares. T=temperature, P=pressure, Amph=amphibole, Cpx=clinopyroxene, Gt=garnet, Law=lawsonite, Ol=olivine, Opx=orthopyroxene, Rt=rutile, Zoi=zoisite and the CMAS system = (MgO, $SiO_2$, $Al_2O_3$, $CaCO_3$).**

To sum up, the criteria used to select the mineral partition coefficient data are:

- temperatures and pressure below 900˚C and 4 GPa, conditions that should characterise the dehydration window in the subducted oceanic crust;
- *Di* data from experiments performed only with pure water, due to the scarcity of data on the influence of solvents over the partition coefficient;
- Experiments with a simple mineral assemblage (composed of one or two minerals) are preferred over more complex mineral assemblage.
- For each of the minerals the same data processing approach is used. Moreover, Chapter 3 contains a more detailed explanation of the rationale and the applied available literature data for the creation of temperature dependent partition coefficients regression for each mineral.

**Step 2:** *Di* extrapolation for REEs

For some REE, such as Pr, partition coefficient data is absent. In such cases, it is necessary to extrapolate from other *Di* values by plotting the radius of REE versus the *Di* value and fit the data to a regression line.

Regressions allow finding a relationship between one dependent variable (in this case the partition coefficient) and series of other independent variables (in this case the ionic radius or the temperature). Comparison between several regressions (power-law, exponential, polynomial, and linear) are performed to determine which one has the best correlation with the data. As an example, Figure 4 contains the available REE data for clinopyroxene at 700˚C and several possible regressions associated with the data. It can be observed that as the ionic radius of the elements gradually decreases, the atomic radius of the elements increases. In this case, it was necessary to extrapolate the *Di* for praseodymium, terbium, holmium and thulium. For example, praseodymium has an ionic radius of 1.126 Å, which sits between cerium (ionic radius = 1.143 Å) and neodymium (ionic radius = 1.109 Å). Table 3 contains the calculated *Di* results based on the four types of regressions for Pr. For this element, the variation between the different *Di´*s values, given by the regressions can be seen in column 3 of Table 3. The best fit, for this specific element, is a 4-degree polynomial regression (see Equation 2.7).

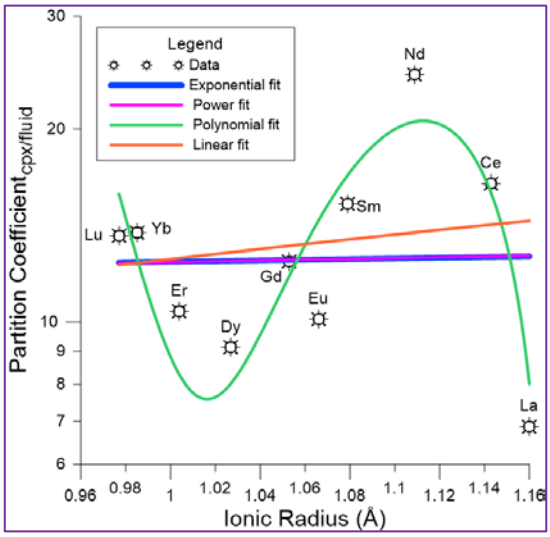


**Figure 4: $Di_{cpx/fluid}$ data for clinopyroxene at 700˚C, from Kessel et al. (2005) and possible fits associated. The plotted elements have 3+ valency.**

| Regression type | $R^2$ | $Di_{Pr}$ value |
|---|---|---|
| Exponential | 0.0005 | 12.60908 |
| Linear | 0.0228 | 13.992 |
| Polynomial | 0.8008 | 22.67921 |
| Power-law | 0.0007 | 12.63093 |

**Table 3: Praseodymium´s *Di* values calculated with several types of regressions and their respective $R^2$.**

The exponential regression is one of the simplest regression methods, where the dependent value (*Di*) results from the elevation of the independent variable (temperature) over a coefficient:

$$\ln(Di) = ar_i + b \Leftrightarrow Di = exp(ar_i + b) = exp(ar_i)\, exp(b) \qquad (2.6)$$

where $a$ and $b$ are coefficients and $r_i$ is the REE's ionic radius from Shannon (1976).

A polynomial regression consists of several algebraic terms each of which includes a coefficient multiplied by the independent variable (ionic radius or temperature) and raised to a non-negative integral power:

$$ln(Di) = ar_i^3 + br_i^2 + cr_i + d \Leftrightarrow D = \exp(ar_i^3)\exp(br_i^2)\exp(cr_i)\exp(d) \quad (2.7)$$

where $a$, $b$, $c$ and $d$ are coefficients and $r_i$ is the ionic radius of the REE (Shannon, 1976).

Exponential equations are used for all minerals to predict the missing REE. However, for clinopyroxene and zoisite predictions, polynomial equations are used.

**Step 3:** Temperature-dependent regression calculations

A comparison between the different regressions shows that the exponential regression has the best correlation with the mineral-fluid partition coefficient data, so these are used to calculate the temperature-dependent mineral–fluid partition coefficients for all elements. For better accuracy of the regressions, more experimental data are necessary, which are not available in the literature. The acquisition of experimental data is beyond the scope of this dissertation.

## 2.3 Statistics and uncertainties of the data

Standard deviation (1σ and 2σ) and standard error (SE) are used in the utilized studies to demonstrate the accuracy of the analyses performed in each experiment. The standard deviation (Equation 2.8) of the sample measures how much the individual values differ from the sample mean, i.e. it calculates the dispersion of the individual values from the mean of the data. The standard error (Equation 2.9) of the sample mean is a statistical method used to estimate the degree of difference between the sample mean and the population mean, i.e. how accurate the estimate is of the mean value of the sample.

$$\sigma = \sqrt{\frac{\sum_{i=1}^{N}(x_i - \bar{x})^2}{N-1}} \quad (2.8)$$

where $\bar{x}$ is mean value of the sample, $x_i$ are the measured values with *i* between 1 and N, and *N* is the total number of measured values.

$$SE = \frac{\sigma}{\sqrt{N}} \quad (2.9)$$

where $\sigma$ is the standard deviation and *N* is the total number of measured values.

The analytical and the model error are two types of statistics measurements that can be used to determinate the accuracy of the prediction models of the trace elements partition coefficients created in this dissertation. The analytical error is given by the difference between the performed analyses and the concentration of the element in the sample (Miesch 1967). Standard deviations are used to determine the analytical error of the paper used in this dissertation to predict the trace

elements mineral-fluid partition coefficient. Appendix I contains all analytical errors, and the analytical percentage of this error is plotted in the figures 9, 13 and 20, where the partition coefficient is plotted against the ionic radius of the trace element. The model error gives the statistic measures that show in which degree the created model can reproduce the existent data. Due to the limited number of data points, the $R^2$ (Equation 2.10) are the only statistic method that is applied to measure the model errors.

$$R^2 = \frac{\sum(T - \bar{T})(Di - \overline{Di})}{\sqrt{\sum(T - \bar{T})^2 \sum(Di - \overline{Di})^2}} \tag{2.10}$$

where *T* and *Di* are the measured temperature and partition coefficient values, and $\bar{T}$ and $\overline{Di}$ are calculated using Equations 2.11and 2.12, respectively.

$$\bar{T} = \frac{1}{N}\sum_{i=1}^{N} Ti \tag{2.11}$$

and

$$\overline{Di} = \frac{1}{N}\sum_{i=1}^{N} Di_i \tag{2.12}$$

where *N* is the total number of measured values, is mean value of the sample $Ti$ and $Di_i$ are the mean values of the temperature and the partition coefficient respectively.

# 3. Results

This chapter describes the calculation of temperature-dependent partition coefficients for six of the discussed minerals. Each mineral has general information about its chemical and physical characteristics and detailed information about how the regressions were determined, as well as the variation of partition coefficients of each trace element with temperature.

## 3.1 Amphibole

### *3.1.1 General information*

Amphibole is the general name of minerals with structure formula $AX_2Z_5((Si,Al,Ti)_8O_{22})(OH,F,Cl,O)_2$, where the position A can be occupied with Na, K, Ca, or $Pb^{2+}$, X can be occupied with Li, Na, Mg, $Fe^{2+}$, $Mn^{2+}$ or Ca, and Z by $Li^{1+}$, $Na^{1+}$, Mg, $Fe^{2+}$, $Mn^{2+}$, Zn, Co, Ni, $Al^{3+}$, $Fe^{3+}$, $Cr^{3+}$, $Mn^{3+}$, $V^{3+}$, Ti or Zr. It is an extensive and complex group, where minerals share a similar crystal structure but have different proportions of Na, Ca and Mg. It has a wide-ranging stability field under hydrous conditions, and this allows its presence in a large variety of lithologies. The breakdown of this mineral in the basaltic systems occurs between 2.3 and 2.5 GPa (corresponding to around 65-70 km) and releases 0.4 wt.% of $H_2O$ of total water in the altered oceanic crust (Schmidt & Poli 2013), which, in the presence of chlorite, can produce chloritoid. Ellis & Thompson (1986) demonstrate that the amphibole can be stable above the solidus in fluid saturated systems. At certain conditions, amphibole can be stable between 600°C and 1120°C (Ridolfi et al. 2010) and coexist with zoisite, garnet, clinopyroxene and paragonite (Poli & Schmidt 1995). In peridotite, amphibole can be the major hydrous phase to a depth of 450 km (Inoue et al. 1998).

zoisite + amphibole + quartz ⇄ anorthite + clinopyroxene + $H_2O$ (3.1)

hornblende ⇄ 8 diopside + 3 pyrope + 4 quartz + 4 $H_2O$ (3.2)

amphibole + epidote ⇄ chloritoid + clinopyroxene + quartz + $H_2O$ (3.3)

Reaction 3.1 describes a possible breakdown reaction for amphibole + zoisite under 1.5 GPa (Ellis & Thompson, 1986). Reaction 3.2 shows a possible mineral assemblage that would result from the disappearance of hornblende down to 1.9 GPa, and reaction 3.3 shows the breakdown of amphibole at high pressures (2.4-2.6 GPa) (Poli 1993).

The amphibole group consists of 76 recognized mineral species, amongst which a complex substitution between sodium and calcium, and between magnesium, iron and manganese exists. Due to this crystal structural complexity, it is difficult to conduct laboratory experiments to study the role of crystal structure and composition on amphibole-liquid or fluid partitioning (Tiepolo et al. 2007), which explains the relatively limited database available. The ability of amphibole to retain REE in its structure exceeds the ability of pyroxenes, plagioclases and olivine. In basalts, the LREE are more

compatible with the amphibole than the HREE, moreover, the MREE are more compatible than the LREE resulting in the typical steep REE pattern ( Davidson et al. 2007; Lesnov 2010). Amphibole is rich in Ta, Nb, Sr, Zr and LILE, but retains a low concentration of Rb in its structure (Ionov & Hofmann 1995; Adam & Green 2006).

The data from Adam et al. (1997) is not used for the prediction of *Di* because the mineral-fluid partitioning is measured in water-saturated melts and does not represent pure water conditions. Brenan et al. (1995) demonstrated that the HCl presence in the solute decreases the amphibole-fluid partitioning. The mixture of water and HCl used in the Brenan et al. (1995) makes their measured *Di* inapplicable for this study, while the data from Fabbrizio et al. (2013) is not used for its peridotitic starting composition. For the calculation of the fluid-associated *Di* values (instead of melt-associated), the *Di* between amphibole and clinopyroxene is calculated (Equation 2.5). These two minerals are widespread in basalt rocks, and the amphibole–clinopyroxene partition coefficient is well constrained (Varne & Graham 1971; Witt-eickschen et al. 1998; Tribuzio et al. 1999), which helps to better constrain amphibole–fluid *Di* values. The amphibole-fluid partition coefficient in this dissertation is dependent on clinopyroxene-fluid *Di* and on amphibole-clinopyroxene *Di*. As result, the trend of amphibole-fluid *Di* values for each element could be similar to the trend clinopyroxene-fluid *Di*. The amphibole–clinopyroxene partitioning values are taken from Zack et al. (2002), and clinopyroxene–fluid partitioning is taken from Kessel et al. (2005).

### *3.1.2 Calculation of the missing REE data*

Figure 5 shows the behaviour of $Di_{(REE)}$ plotted versus the ionic radius for two different temperatures. The partition coefficient decreases with increasing ionic radius for both temperatures. Exponential equations were used to calculate the partition coefficient of the missing elements. Table 4 contains the results from Equation 2.6 with their coefficient of determination for the data for two temperatures.

| T | Coefficients | $R^2$ |
|---|---|---|
| 650 | a = -18.2218 | 0.9425 |
| | b = 22.73804 | |
| 920 | a = -17.27804 | 0.9606 |
| | b = 19.0548 | |

**Table 4: Results from the predicted models for the calculation of the missing REE Di values, using $Di=exp(ar_i+b)$. The second column has the coefficients used in the exponential equation, and the last column has $R^2$ for each temperature.**

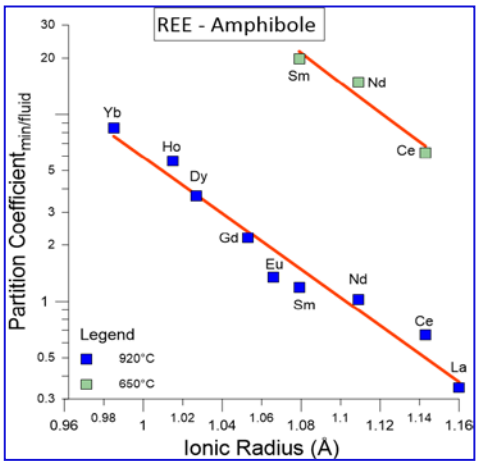


**Figure 5: Amphibole-fluid partition coefficient, when plotted versus the ionic radius $r_i$ at 650 and 920˚C. The data for 650˚C is calculated from Zack et al. (2002) and Kessel et al (2005). The data for 920˚C is calculated between Zack et al. (1997) and Kessel et al. (2005). The symbols represent the calculated data and the red lines are the best exponential fits to these data for each temperature. The plotted elements have 3+ valency.**

### *3.1.3 Di coefficients and results*

| Element | Coefficients | $R^2$ | Element | Coefficients | $R^2$ |
|---|---|---|---|---|---|
| La | a = -0.01043 | 1 | Tm | a = -0.01017 | 1 |
| | b = 8.38003 | | | b = 11.2362 | |
| Ce | a = -0.01036 | 1 | Yb | a = -0.00982 | 1 |
| | b = 8.64581 | | | b = 11.17432 | |
| Pr | a = -0.00971 | 1 | Lu | a = -0.01023 | 1 |
| | b = 8.53123 | | | b = 11.58456 | |
| Nd | a = -0.00989 | 1 | Th | a = -0.01029 | 1 |
| | b = 9.13082 | | | b = 8.50488 | |
| Sm | a = -0.01041 | 1 | U | a = -0.00927 | 1 |
| | b = 9.75736 | | | b = 6.97721 | |
| Eu | a = -0.01117 | 1 | Zr | a = -0.018063 | 1 |
| | b = 10.57698 | | | b = 16.26765 | |
| Gd | a = -0.01025 | 1 | Nb | a = -0.00277 | 1 |
| | b = 10.21449 | | | b = 3.74715 | |
| Tb | a = -0.01001 | 1 | Li | a = -0.00076 | 1 |
| | b = 10.29356 | | | b = - 0.5411 | |
| Dy | a = -0.01009 | 1 | Ba | a = -0.00563 | 1 |
| | b = 10.5847 | | | b = 8.82855 | |
| Y | a = -0.00482 | 1 | Sr | a = -0.00731 | 1 |
| | b = 8.02499 | | | b = 6.49581 | |
| Ho | a = -0.0093 | 1 | B | a = 0.00197 | 1 |
| | b = 10.28928 | | | b = -2.43688 | |
| Er | a = -0.01014 | 1 | | | |
| | b = 11.03127 | | | | |

**Table 5: Results from the temperature-dependent regressions for the trace elements, with Di=exp(aT+b). The prediction models use data from Zack et al. (2002) and Kessel et al. (2005).**

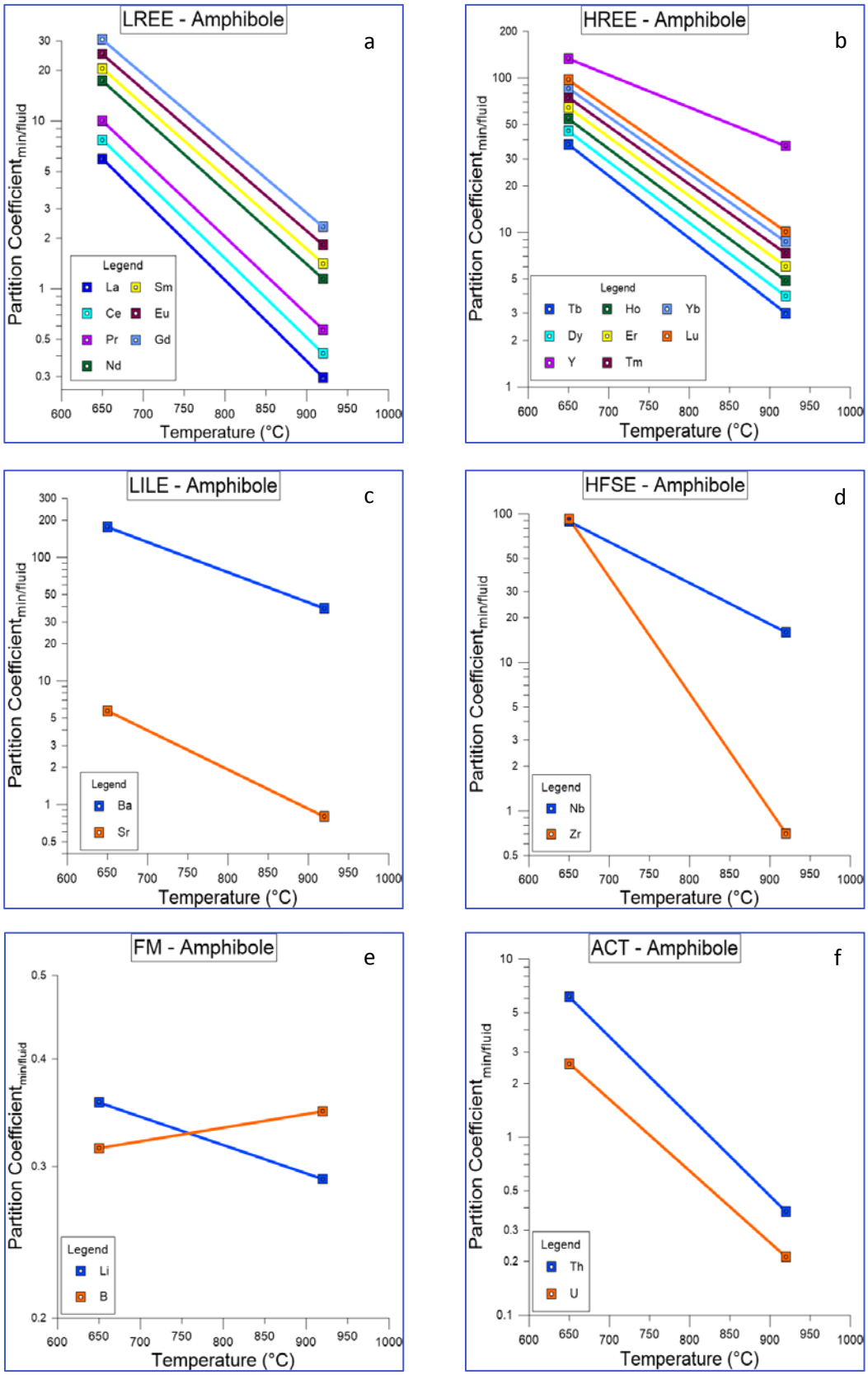


**Figure 6: Diagrams with partition coefficients plotted against the temperature of: a) Light Rare Earth elements; b) Heavy Rare Earth elements; c) Large-ion Lithophile elements; d) High field-strength elements; e) Fluid Mobile elements; and f) Actinide element. The squares represent the available data from Zack et al. (2002) and Kessel et al. (2005) and the lines represent the respective fit lines.**

Due to the limited *Di* database for amphibole, the prediction of the temperature-dependent trace element partition coefficient behaviour is calculated with only two data points. Table 5 contains the respective coefficients for the exponential regressions used in these predictions. When the exponential regressions are calculated only with two data points, the $R^2 = 1$ is not meaningful.

For the available data of amphibole, the partition coefficients of trace elements, in the same group, have similar behaviour (Figure 6). Most of the trace element *Di* values decrease by about one order of magnitude between 650˚C and 920˚C, which makes the temperature dependence of partitioning between amphibole and trace elements a robust feature, despite the limited availability of the data. The only exception is zirconium, for which *Di* decreases by two orders of magnitude over the same temperature interval and B and Li, for which the *Di* value stays rather stable at about 0.3.

## 3.2 Clinopyroxene

### *3.2.1 General information*

Clinopyroxene is a monoclinic pyroxene with the general formula $(Na, Al, Ca, Mg, Fe)_2SiO_6$ and can be either sodic or calcic. This type of pyroxene is widespread in basic and ultrabasic igneous rocks such as basalts and peridotites and high pressure and temperature metamorphic rocks such as eclogites. Pyroxene can be stable to 20 GPa and 1450°C (Ringwood & Major 1968; Akaogi & Akimoto 1977), corresponding to 600 km of depth.

If there is no olivine in the system, clinopyroxene controls all the lithium and beryllium and keeps them in its structure until exposed to extreme temperatures (Zack et al. 2002; Woodland et al. 2002). In systems where zoisite is absent, lead is compatible with clinopyroxene. rubidium, barium, caesium and strontium are strongly incompatible with this mineral. Furthermore, clinopyroxene favours HREE and tantalum over niobium, and hafnium over zirconium (Green & Adam 2003). The vast stability field and the significant capacity to retain important trace element makes clinopyroxene important for understanding the composition of the fluid that is released from subducted ocean crust.

Stalder et al. (1998) and Green et al. (2000) agree that the partition coefficient between clinopyroxene and fluid is pressure-dependent and that *Di* values decrease with increasing pressure. However, there is not enough data to calculate pressure-dependent regression, so the pressure influence is ignored in this dissertation.

Figure 7 shows all available niobium *Di* data for clinopyroxene. The database available for clinopyroxene–fluid partition coefficients is larger than for amphibole. To uniform the data for this mineral first was calculated of average values for some of Brenan et al. (1995) and Brenan et al. (1998) data. This is necessary due to the almost identical *Di* values for the same temperature. Green

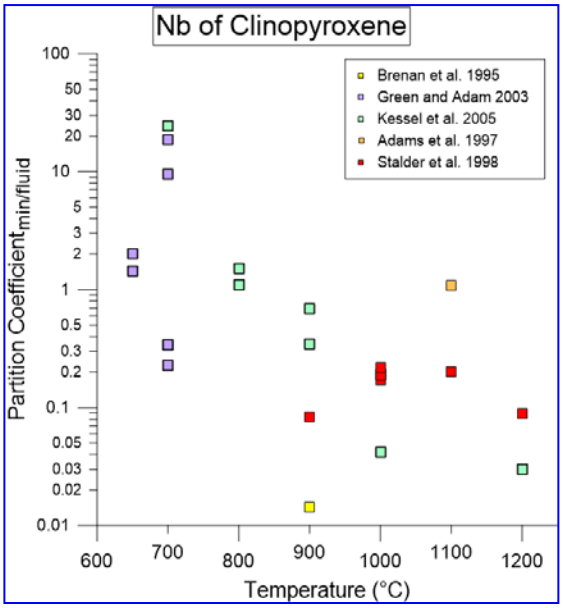


**Figure 7: The available data for clinopyroxene-fluid partitioning for Niobium.**

& Adam (2003) measured clinopyroxene-fluid *Di* values in a mineral assemblage of phengite, allanite, zircon and rutile, and these minerals can buffer the partition coefficients for LILE, HFSE and LREE (Hermann et al. 2006). For this reason, the data from this study are excluded in the calculation of partition coefficients. The *Di* from Stalder et al. (1998) and Adam et al. (1997) are not used due to the high ambient pressures and temperatures of their data, which implies the possible existence of melt in the system or potential supercritical conditions. For this mineral, the data used for the *Di* parameterisation is from Kessel et al. (2005), Brenan et al. (1995) and Brenan et al. (1998). Caciagli et al. (2011) present alternative fits (Eqn. 2.3 and 2.4) for lithium. Figure 8 shows the *Di* from Kessel et al. (2005) and some data from Caciagli et al. (2011). The *Di* values from Kessel et al. (2005) (slightly) decrease with the temperature, while the data from Caciagli et al. (2011) increase. In the first study, the pressure is 4 GPa, and in the second the pressure is 1 GPa. The large pressure difference between these studies can be a possible explanation for this different behaviour. Although both studies performed the *Di* measurements at the same temperature, the big difference of the pressures could be a possible problem when the *Di* from both studies is used for the formulation of a single temperature-dependent regression. Therefore, it was necessary to use data from only one of the papers. Caciagli et al. (2011) determined the partition coefficient only of lithium between clinopyroxene and fluid, while in the study of Kessel et al. (2005), a total of 26 trace elements partition coefficient between clinopyroxene and fluid were determined. To ensure that most of the data were determined at similar conditions, the lithium data was taken from Kessel et al. (2005).

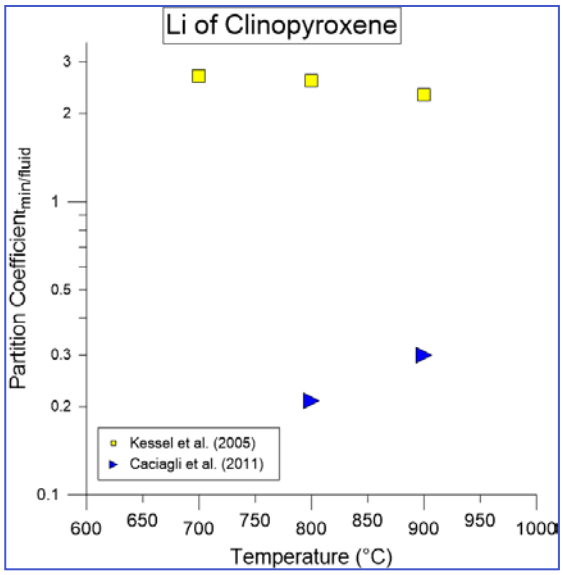


**Figure 8: Clinopyroxene-fluid partition coefficient of lithium plotted versus the temperature. The data from Kessel et al. (2005) is measured at 4 GPa and the data from Caciagli et al. (2011) is measured at 1 GPa.**

Here, I use an alternative to Caciagli et al. (2011) (Equation 2.3), with a data adopted from Kessel et al. (2005).

Due to the lack of data for Cpx concentration in the study of Kessel et al. (2005), it was necessary to use the garnet concentration to calculate the partition coefficient between clinopyroxene and fluid:

$$Di = \frac{(Di_{bulk} - X_{fluid}) - (m_{Gt} * X_{Gt})}{(X_{fluid} * m_{Cpx})} \quad (3.4)$$

where $Di_{bulk}$ is the whole rock-fluid partition coefficient of a certain element, $X_{fluid}$ is the concentration of the same element in the fluid, $X_{Gt}$ is the concentration of the same element in the garnet, and $m_{Gt}$ and $m_{Cpx}$ are the garnet and clinopyroxene abundance in the rock, respectively.

### *3.2.2 Calculation of the missing REE data*

For the prediction of the missing REEs (praseodymium, terbium, holmium and thulium), two different types of regression were used: a third-order polynomial equation is the best fit for the data at 700˚C (Figure 9a) due to the parabolic behaviour of the *Di* when plotted versus the ionic radius; for 800˚C the best fit for the data is a second-order polynomial equation (Figure 9b), while, for 900˚C, an exponential regression was used (Figure 9c). Mineral–fluid partitioning behaviour is more chaotic and does not have such a direct relationship as mineral-melt partitioning with the ionic radius. A possible explanation for this can be the changes of the solubility of the $H_2O$ or changes of the structure and major element compositions of this mineral with the increasing temperature. The partition coefficient decreases by one order of magnitude between Lanthanum and Lutetium for all temperatures. The Er, Dy and Yb partitioning values are almost the same for 700˚C and 800˚C, but at 900˚C the *Di* value of these elements increases, showing evidence that the partition coefficient starts to be more affected by high temperatures. Table 6 contains all the coefficients and the $R^2$ from these predictions.

| T | Coefficients | $R^2$ |
|---|---|---|
| 700 | a = -2167.33 | 0.8008 |
| | b = 6918.59 | |
| | c = -7347.52 | |
| | d = 2598.51 | |
| 800 | a = -29.253 | 0.8293 |
| | b = 54.389 | |
| | c = - 22.757 | |
| 900 | a = -16.625 | 0.9731 |
| | b = 18.251 | |

**Table 6: The clinopyroxene coefficients resulting from the prediction of the missing REE. For 700˚C the equation used is $Di=\exp(ar_i^3+br_i^2+cr_i+d)$. For 800˚C and 900˚C the equations used are $Di=\exp(ar_i^2+br_i+c)$ and $Di=\exp(ar_i+b)$, respectively.**

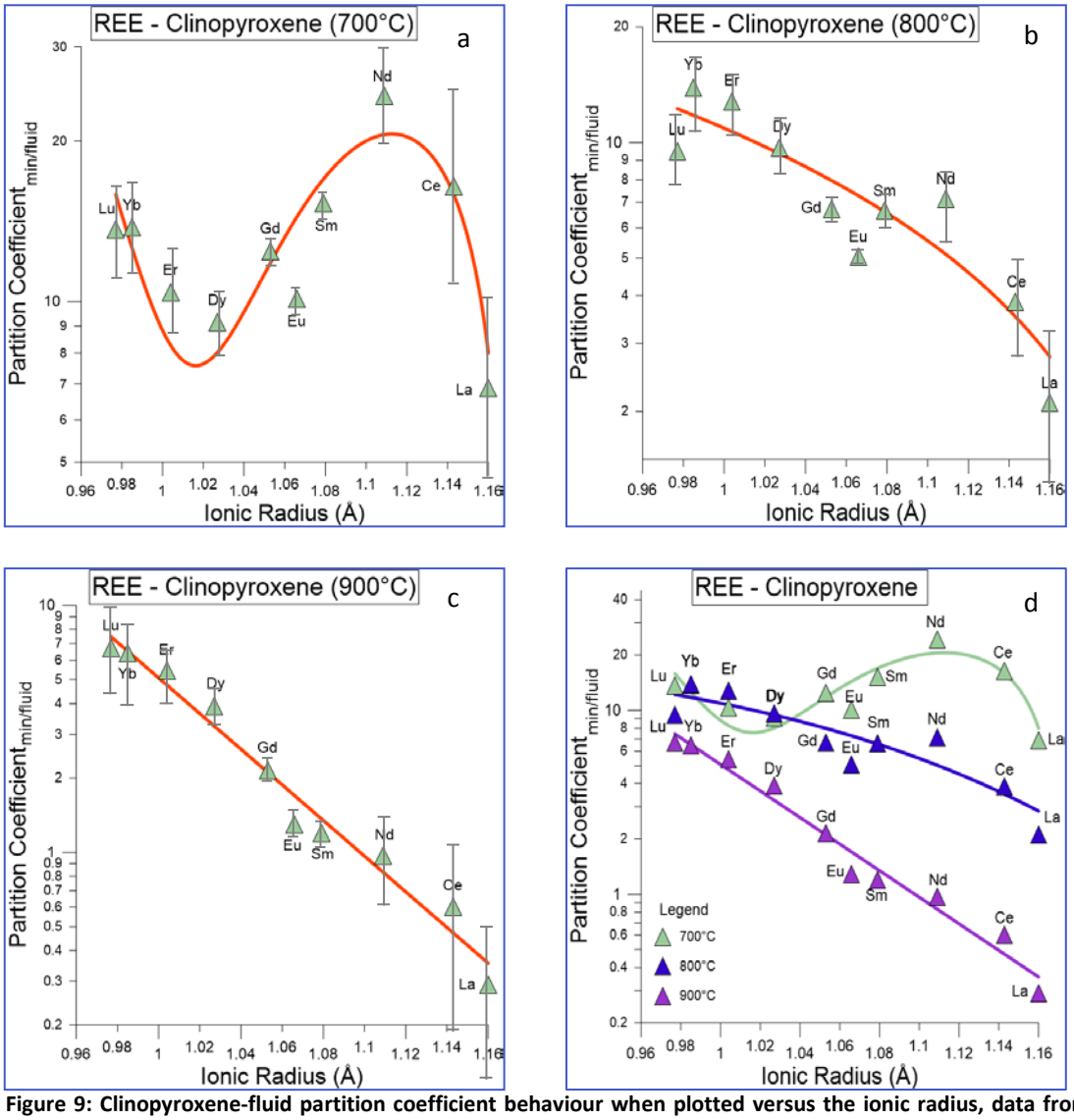


**Figure 9: Clinopyroxene-fluid partition coefficient behaviour when plotted versus the ionic radius, data from Kessel et al. (2005): a) 700˚C with third-degree polynomial equation; b) 800˚C with second-degree polynomial equation; and c) 900˚C with exponential regression. The symbols represent the available data for each temperature and the red line is the best-fit associate to these data. d) contains all REEs partition coefficients plotted together. The set of whiskers represents the analytical error from Kessel et al. (2005). The plotted elements have 3+ valency.**

### *3.2.3 Di coefficients and results*

Exponential equations are used to calculate the partition coefficient behaviours (Table 7). In general, the prediction models are quite precise, with only 8 (of a total of 30 elements) with an $R^2$ under 0.8. Figure 10 shows some examples of the worst and the best fit produced for the *Di* parameterisation.

From the available data for clinopyroxene, the behaviour of the partition coefficients of the trace elements within the same group exhibit similar behaviour (Figure 11). However, the gradual decrease of *Di* values with temperature is not observed for all REEs (Figure 11a,b) due to the apparently irregular behaviour of the REE at 700˚C when plotted against ionic radius (Figure 9d).

Yttrium has larger values than rest of the geochemically similar HREE for this mineral. Scandium, rubidium, caesium and boron are trace elements for which the partition coefficient has a positive correlation with temperature.

| Element | Coefficients | $R^2$ | Element | Coefficients | $R^2$ |
|---|---|---|---|---|---|
| La | a = -0.0158 | 0.9795 | Hf | a = -0.0173 | 0.9969 |
| | b = 13.1263 | | | b = 16.4817 | |
| Ce | a = -0.0165 | 0.9950 | Li | a = -0.0007 | 0.9121 |
| | b = 14.4376 | | | b = 1.5103 | |
| Pr | a = -0.0172 | 0.9975 | Zr | a = -0.0172 | 0.9856 |
| | b = 15.0252 | | | b = 15.8093 | |
| Nd | a = -0.0161 | 0.9810 | U | a = -0.0145 | 0.9671 |
| | b = 14.4089 | | | b = 11.5385 | |
| Sm | a = -0.0128 | 0.9624 | Th | a = -0.0175 | 0.9493 |
| | b = 11.7942 | | | b = 15.2479 | |
| Eu | a = -0.0103 | 0.9665 | Sr | a = -0.0123 | 0.6762 |
| | b = 9.7419 | | | b = 10.3345 | |
| Gd | a = -0.00878 | 0.9713 | Rb | a = 0.0035 | 0.6883 |
| | b = 8.7550 | | | b = -6.1649 | |
| Tb | a = -0.0066 | 0.8112 | Nb | a = -0.0275 | 0.7343 |
| | b = 7.0572 | | | b = 22.4073 | |
| Dy | a = -0.0042 | 0.7266 | Pb | a = -0.0096 | 0.8519 |
| | b = 5.3358 | | | b = 5.9485 | |
| Y | a = -0.0035 | 0.4233 | Ba | a = -0.0213 | 0.4703 |
| | b = 6.9669 | | | b = 14.0633 | |
| Ho | a = -0.0034 | 0.5742 | B | a = 0.0036 | 0.9560 |
| | b = 4.7035 | | | b = -4.2763 | |
| Er | a = -0.0032 | 0.7198 | Be | a = -0.005 | 0.9309 |
| | b = 4.7294 | | | b = 3.8407 | |
| Tm | a = -0.0030 | 0.6625 | Cs | a = 0.0022 | 0.9215 |
| | b = 4.5728 | | | b = -6.2678 | |
| Yb | a = -0.0038 | 0.8956 | Sc | a = 0.004 | 0.7851 |
| | b = 5.3643 | | | b = -0.4287 | |
| Lu | a = -0.0036 | 0.9990 | Ta | b = -0.0158 | 0.9995 |
| | b = 5.0961 | | | a = 14.4347 | |

**Table 7: Results from the exponential regressions for the trace elements of clinopyroxene, with Di=exp(aT+b).**

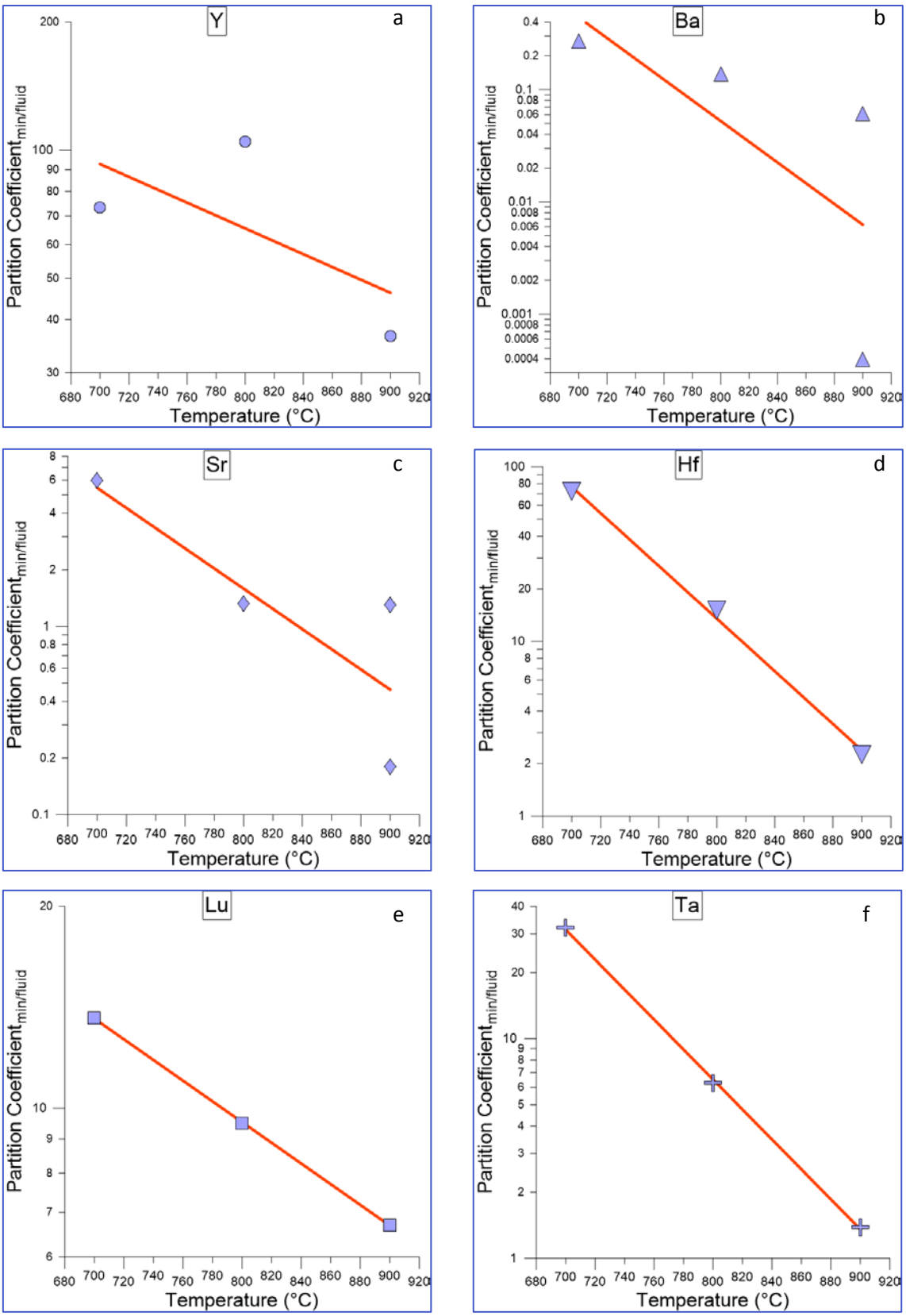


**Figure 10: Examples of 6 predictive models (3 examples of the best and 3 for the worst fits), when *Di* is plotted against the temperature. a) Y ($R^2$ = 0.4233) with data from Kessel et al. (2005); b) Ba ($R^2$ =0.4703) with data from Kessel et al. (2005); c) Sr ($R^2$ = 0.6762) with data from Kessel et al. (2005) and Brenan et al. (1995); d) Hf ($R^2$ = 0.9969) with data from Kessel et al. (2005); e) Lu ($R^2$ =0.9990) with data from Kessel et al. (2005); and f) Ta ($R^2$ =0.9995) with data from Kessel et al. (2005). The symbols represent the available data for each element and the red line is the best-fit associated with these data.**

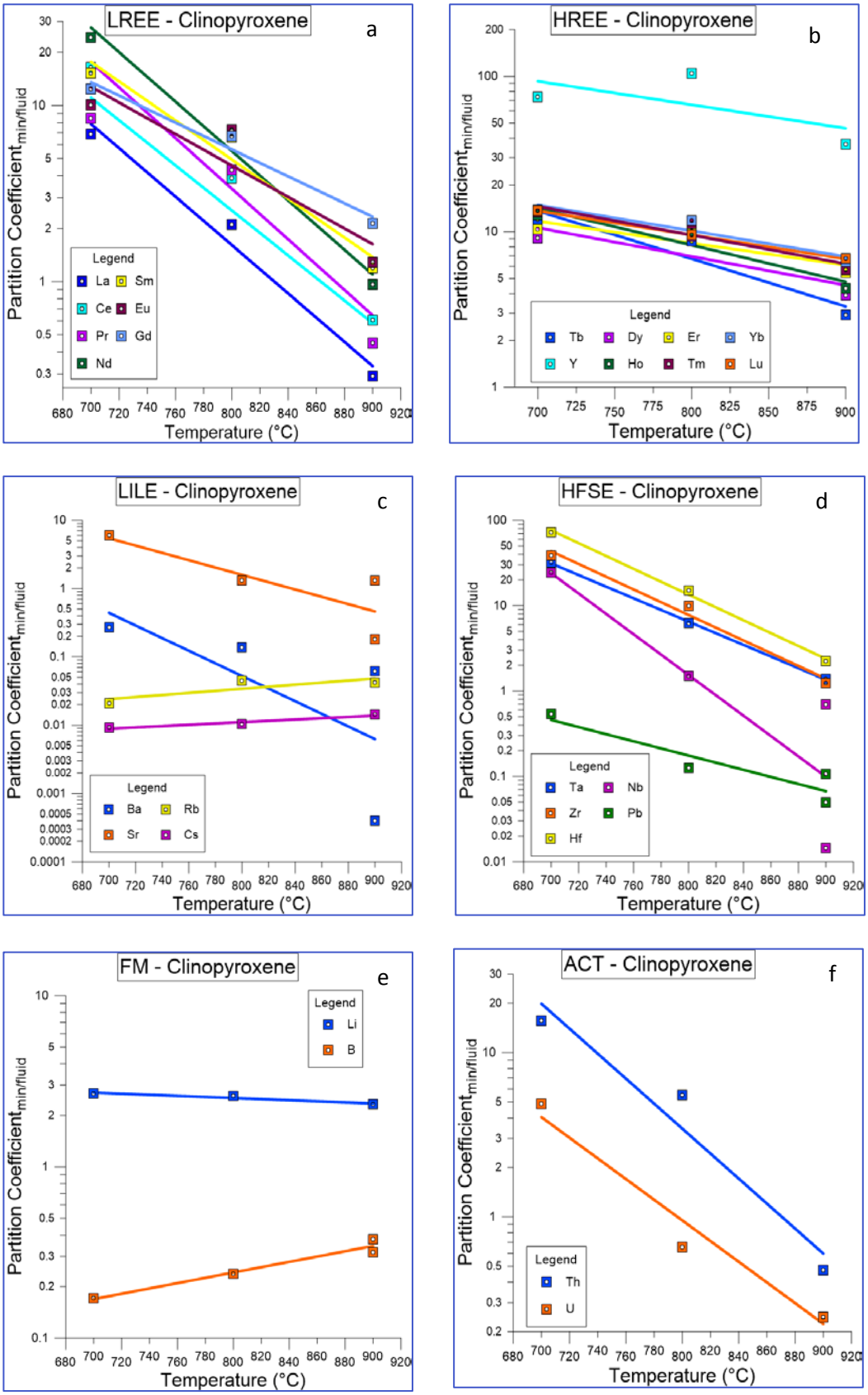


**Figure 11: Diagrams with partition coefficients plotted against temperature for: a) Light Rare Earth elements; b) Heavy Rare Earth elements; c) Large-Ion Lithophile elements; d) High Field-Strength elements; e) Fluid Mobile elements; and f) Actinide elements. The squares represent the available data from Kessel et al. (2005), Brenan et al. (1995) and Brenan et al. (1998), and lines represent their respective best-fitting parameterisation.**

## 3.3 Garnet

### *3.3.1 General information*

Garnet is a general name for a group of minerals with structural formula $X_3Y_2(SiO_4)_3$, where X can be Mg, Ca, $Mn^{2+}$ and $Fe^{2+}$ and Y can be $Cr^{3+}$, $Fe^{3+}$, $Al^{3+}$, $Mn^{3+}$ and $V^{3+}$. A wide range of rocks contain this mineral. Garnet is, for example, common in ultrabasic rocks such as peridotites and kimberlites and even in some alkaline igneous rocks. Garnet is present in metamorphic rocks such as mica schists, gneisses and skarns.

In a MORB-pyrolite assemblage, garnet can be stable at high temperature and pressure at 1483°C and over 2.0 GPa, respectively (Robinson & Wood 1998).

garnet + clinopyroxene ⇄ orthopyroxene + spinel + plagioclase (3.5)

pyroxene + spinel ⇄garnet + olivine (3.6)

At low pressure and relatively high temperature, under 850°C and 0.8 GPa, garnet breaks down (Carswell & Cuthbert 1986; Mukhopadhyay 1991) (reaction 3.5). In serpentine, garnet results from the breakdown of pyroxene and spinel (Macgregor 1970) (reaction 3.6).

During metamorphic processes, the fractionation of trace elements between garnet and fluid is more pronounced than between clinopyroxene and fluid (Stalder et al. 1998). Moreover, for this mineral Stalder et al. (1998) experimentally determined that the fractionation of all elements is more pronounced at 3 GPa than at 5.7 GPa. While pure pyrope is not relevant for basaltic systems, there is an influence of chemical composition of garnet on the *Di* (e.g. the Di value of LREE and HFSE is bigger in pure pyrope garnet than in minerals composed of 90% pure pyrope and 10% of another type of garnet) (Stalder et al. 1998)). Finally, for garnet, the partition coefficient does not vary significantly between pure water and a mixture of water and hydrochloric acid (Stalder et al. 1998).

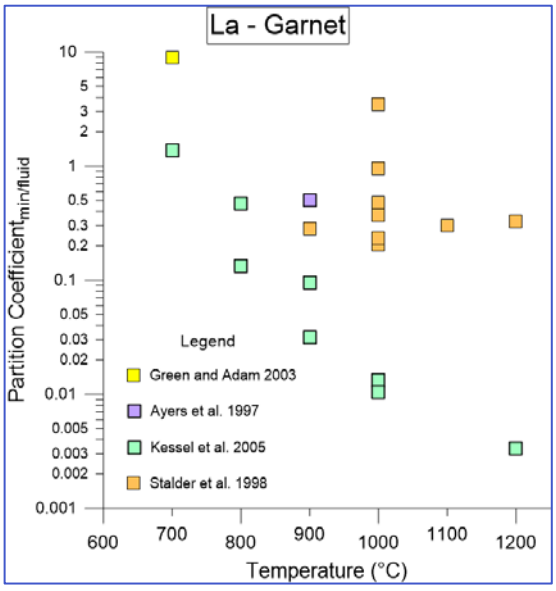


**Figure 12: Lanthanum available data for garnet fluid partitioning.**

Garnet has an extremely low affinity for elements such as Cs, Rb, Ba and Sr and a low affinity for Nb and Ta (Green et al. (2000); Green & Adam 2003). On the other hand, HREE and Y have a high affinity with this mineral and garnet retains HREE better than LREE (Otamendi et al. 2002; Spandler et al. 2003; El Korh et al. 2009; Miller et al. 2007).

Figure 12 contains an example of all available Lanthanum *Di* data for garnet. The *Di* data selection for garnet uses the same procedure and data sets as for clinopyroxene. First, the average values for some of Brenan et al. (1995) and Brenan et al. (1998) data were calculated. The data used from Brenan et al. (1995) is only from measurements of partition coefficients between minerals and pure water. Green & Adam (2003) was excluded due to the complex mineral assemblage used in their experiments. Finally, as mentioned in section 3.2.1 of this chapter, the *Di* from Stalder et al. (1998) and Adam et al. (1997) are calculated at high PT conditions, so these studies are not used. For this mineral, the data used is data from Brenan et al. (1995), Brenan et al. (1998) and Kessel et al. (2005).

### *3.3.2 Calculation of the missing REE data*

For garnet, the adopted procedure for estimating *Di* values for REE elements for which no data is available is different from the one used for other minerals. LREE and HREE *Di*'s values were plotted versus the ionic radius separately (Figure 13, a and b), due to small inflection around Gd. The predicted values for the LREE are two to three times closer to the measured values from Kessel et al. (2005) than when the prediction is made with all REEs together. An example of this kind of behaviour is for the 900°C data. When the prediction model is using all REE, the predicted value for $Di_{Lu}$=465, two times larger than the measured *Di*=215 from Kessel et al. (2005). When the regression is done for LREEs only, the $Di_{La}$=248, much closer to the measured value. This method, therefore, gives a more accurate prediction of the values for the missing LREE (praseodymium, terbium, holmium and thulium). Table 8 contains all the coefficients and the $R^2$ from these predictions.

| T/Element | Coefficients | $R^2$ |
|---|---|---|
| **700/LREE** | a = -49.66 | 0.9887 |
| | b = 57.84 | |
| **700/HREE** | a = -14.95 | 0.9979 |
| | b = 21.03 | |
| **800/LREE** | a = -50.32 | 0.9835 |
| | b = 57.70 | |
| **800/HREE** | a = -25.26 | 0.8652 |
| | b = 31.19 | |
| **900/LREE** | a = -61.47 | 0.9982 |
| | b = 67.87 | |
| **900/HREE** | a = -30.03 | 0.9530 |
| | b = 34.86 | |

**Table 8: The coefficients and the $R^2$ resulting from the exponential regression used for the prediction of the missing REE. The equation used is $Di=\exp(ar_i+b)$.**

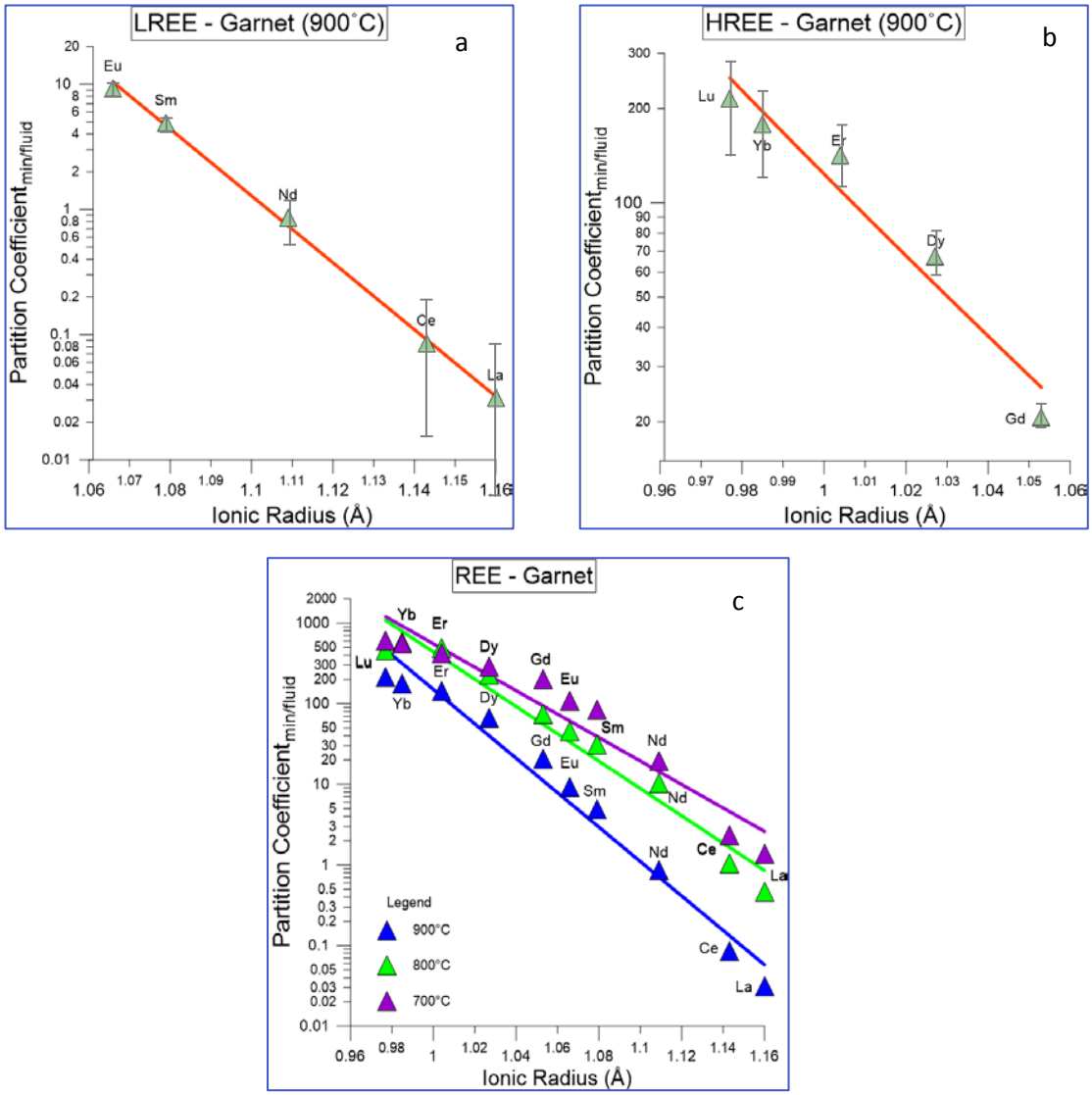


**Figure 13: REE's partition coefficient behaviour, when plotted versus the ionic radius, data from Kessel et al. (2005): a) LREE data at 900˚C with exponential fit; b) HREE data at 900˚C with exponential fit. The symbols represent the available data for each temperature and the red line is the best exponential fit associate to these data. c) all REE data plotted together. The set of whiskers represents the analytical error from Kessel et al. (2005). The plotted elements have 3+ valency.**

### *3.3.3 Di coefficients and results*

For the calculation of the temperature dependence of the partition coefficients, an exponential regression was used. Only ten elements (out of 30) have an $R^2$ value under 0.8. Figure 14 contains three examples of the worst and the best fit produced for the *Di* predictions, and Table 9 contains all the associated coefficients and $R^2$ values. The *Di* of yttrium, rubidium, boron, beryllium, barium and lithium have the worst fit, with $R^2$ under 0.5 (Figure 14, Table 9). With increasing temperature, the fit to the data for these elements does not vary significantly, although data values for yttrium show a scatter of almost a factor 10. Increasing temperature has a similar effect on the garnet–fluid trace element *Di* behaviour as for clinopyroxene. For rubidium, yttrium, scandium and caesium, the partition coefficient (slightly) increases with the temperature, while for the rest of the trace elements, *Di* decreases (by a significantly larger amount).

For the available data of garnet, the partition coefficients of most of the trace elements within the same group exhibit similar behaviour (Figure 15), except for the HREE and the LILE, for which several outliers can be observed.

| Element | Coefficients | $R^2$ | Element | Coefficients | $R^2$ |
|---|---|---|---|---|---|
| **La** | a = -0.0189 | 0.9418 | **B** | a = -0.0145 | 0.3113 |
| | b = 13.7285 | | | b = 8.2815 | |
| **Ce** | a = -0.0165 | 0.9169 | **Ba** | a = -0.0116 | 0.4786 |
| | b = 12.6669 | | | b = 7.4589 | |
| **Pr** | a = -0.0164 | 0.9338 | **Sr** | a = -0.0279 | 0.9443 |
| | b = 13.6353 | | | b = 19.5209 | |
| **Nd** | a = -0.0156 | 0.8956 | **Th** | a = -0.01918 | 0.9943 |
| | b = 13.9975 | | | b = 14.7845 | |
| **Sm** | a = -0.0142 | 0.9704 | **U** | a = -0.0166 | 0.8792 |
| | b = 14.5192 | | | b = 14.0209 | |
| **Eu** | a = -0.0123 | 0.9715 | **Li** | a = -0.0103 | 0.2481 |
| | b = 13.4436 | | | b = 6.6332 | |
| **Gd** | a = -0.0113 | 0.8743 | **Rb** | a = 0.00069 | 0.0585 |
| | b = 13.4819 | | | b = -5.7867 | |
| **Tb** | a = -0.0093 | 0.9538 | **Zr** | a = -0.0132 | 0.8518 |
| | b = 12.1114 | | | b = 13.7247 | |
| **Dy** | a = -0.0072 | 0.8606 | **Nb** | a = -0.0304 | 0.9406 |
| | b = 10.8744 | | | b = 10.9528 | |
| **Y** | a = 0.00087 | 0.0111 | **Hf** | a = -0.01299 | 0.8662 |
| | b = 3.5069 | | | b = 13.0217 | |
| **Ho** | a = -0.0074 | 0.9019 | **Pb** | a = -0.0176 | 0.8612 |
| | b = 11.1889 | | | b = 10.4047 | |
| **Er** | a = -0.0048 | 0.5477 | **Ta** | a = -0.0276 | 0.9664 |
| | b = 9.5051 | | | b = 24.321 | |
| **Tm** | a = -0.0058 | 0.9511 | **Sc** | a = 0.0037 | 0.7059 |
| | b = 10.3298 | | | b = 1.7369 | |
| **Yb** | a = -0.0056 | 0.7127 | **Cs** | a = 0.0033 | 0.6812 |
| | b = 10.4751 | | | b = -8.2525 | |
| **Lu** | a = -0.0052 | 0.9329 | **Be** | a = -0.0157 | 0.4811 |
| | b = 10.1226 | | | b = 10.0901 | |

**Table 9: Results from the exponential regressions for the trace elements of garnet, with Di=exp(aT+b).**

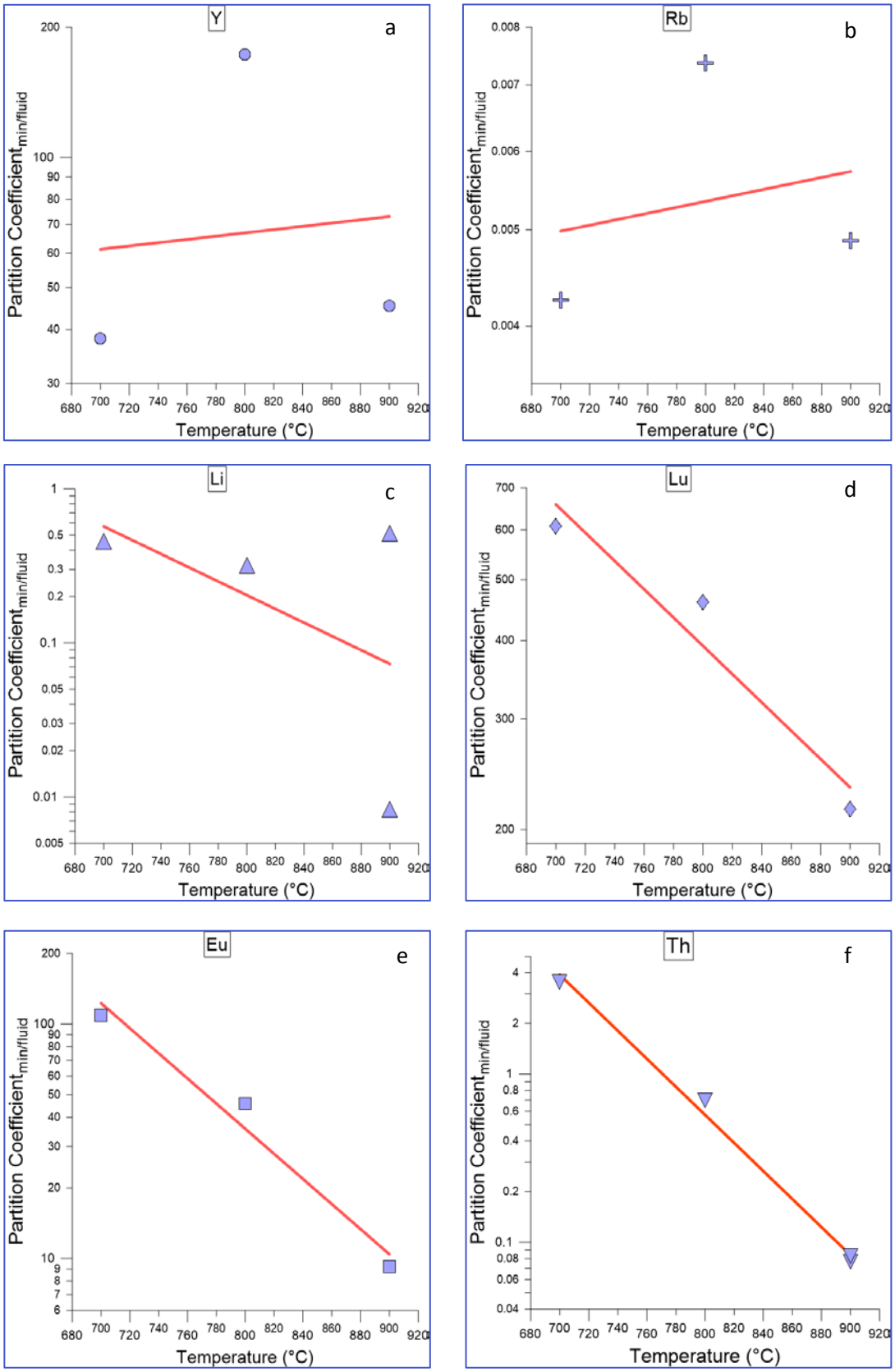


**Figure 14: Examples of the three best and worst prediction models of trace elements, when Di is plotted against the temperature. a) Y ($R^2$ = 0.0111) with data from Kessel et al. (2005); b) Rb ($R^2$ =0.0585) with data from Kessel et al. (2005); c) Li ($R^2$ =0.2481) with data from Kessel et al. (2005) and Brenan et al. ( 1998); d) Lu ($R^2$ =0.9328) with data from Kessel et al. (2005); e) Eu ($R^2$ = 0.9715) with data from Kessel et al. (2005); and f) Th ($R^2$ =0.9943) with data from Kessel et al. (2005). The symbols represent the available data for each element and the red line is the best fit associated to these data.**

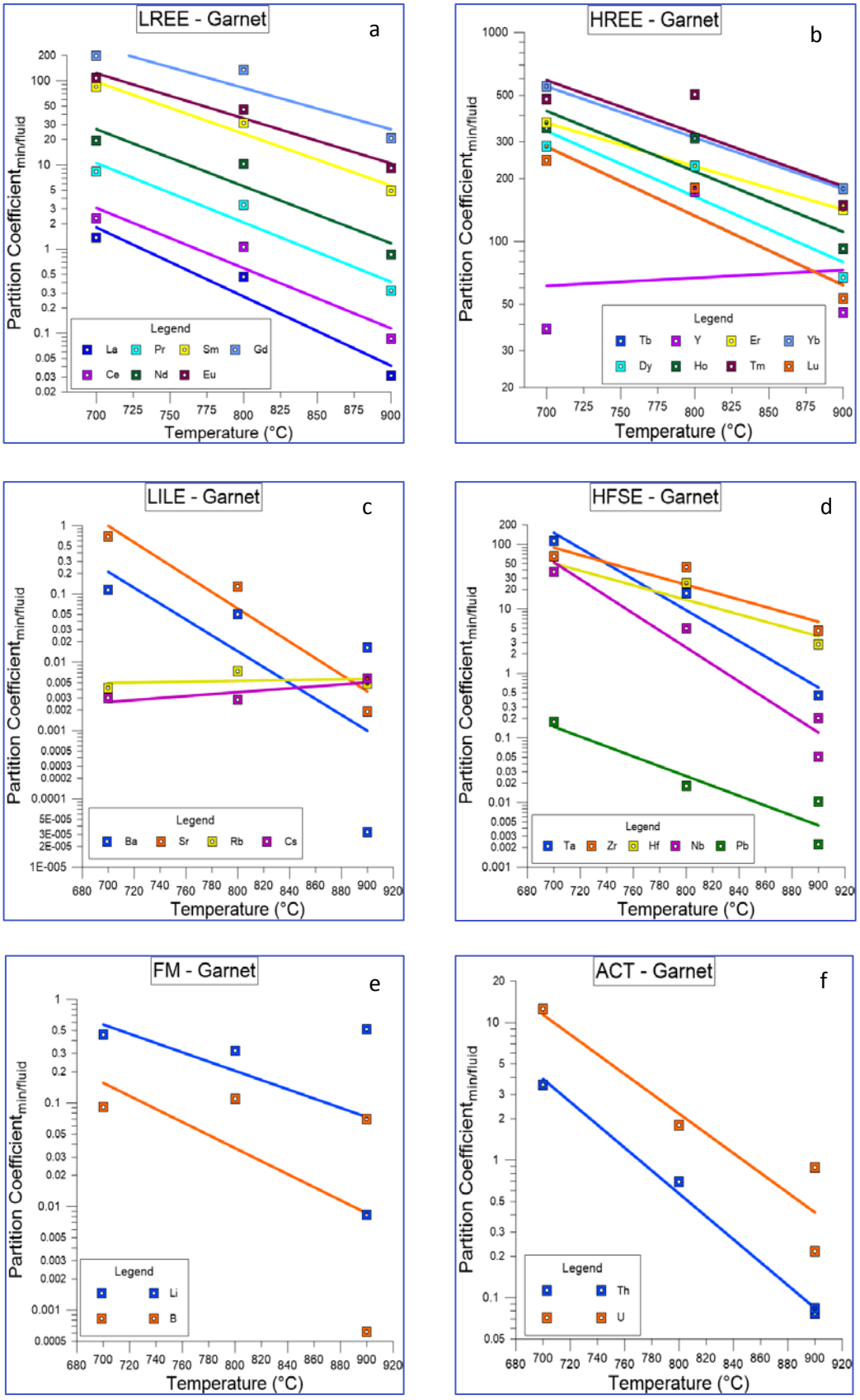


**Figure 15: Diagrams with partition coefficients plotted against the temperature for: a) Light Rare Earth elements; b) Heavy Rare Earth elements; c) Large-ion Lithophile elements; d) High Field-strength elements; e) Fluid Mobile elements; and f) Actinide elements. The data is from Kessel et al. (2005), Brenan et al. (1995) and Brenan et al. (1998) and the squares and lines represents the available data and the respective fit lines.**

## 3.4 Lawsonite

### *3.4.1 General information*

Lawsonite is a hydrous metamorphic mineral with structural formula $CaAl_2(Si_2O_7)(OH)_2.H_2O$, that is stable at high pressures (2-9.2GPa) and low temperatures (550-1040°C). The importance of lawsonite for this study is due to its large capacity for storing water, up to 11.5 wt.% (Schmidt & Poli 1994; Poli & Schmidt 1995; Martin et al. 2011). The occurrence of this mineral is widespread in subducting slabs. During subduction, at low temperature, lawsonite brings crustal bound water to large depth, as its pressure stability field is the highest amongst the hydrous phases present in the crust.

During the fluid-mineral interaction, LREE and Sr are compatible with lawsonite, but elements such as LILE and HFSE are incompatible (Usui et al. 2007; Martin et al. 2011). The breakdown of allanite, in the shallow levels of the subduction zone, will release REE and Sr, and lawsonite will incorporate them (Usui et al. 2007), transporting these elements to greater depths, up to the coesite stability field (Usui et al. 2007). Martin *et al.* (2001) observed that with increasing pressure and temperature, elements like Sr, Be, Th and HREE start to become more incompatible with lawsonite.

$$\text{lawsonite} \rightleftarrows \text{zoisite} + \text{quartz} + \text{kyanite} + H_2O \quad (3.7)$$

$$\text{lawsonite} \rightleftarrows \text{zoisite} + \text{coesite} + \text{kyanite} + H_2O \quad (3.8)$$

$$\text{lawsonite} + \text{clinopyroxene} + \text{garnet}_1 \rightleftarrows \text{garnet}_2 + \text{quartz/coesite} + H_2O \quad (3.9)$$

The breakdown of lawsonite is strongly temperature dependent and may create another hydrous phase, e.*g.* zoisite (Schmidt & Poli 1994; Poli & Schmidt 1995) at pressures between 1.7 and 6.5 GPa, see reactions 3.7 and 3.8. Reaction 3.9 shows the breakdown of lawsonite at a temperature above 650°C and 3 GPa. At cold geothermal gradients conditions, lawsonite could be the last hydrous phase present in the slab crust, and its breakdown will leave a dry eclogitic residue.

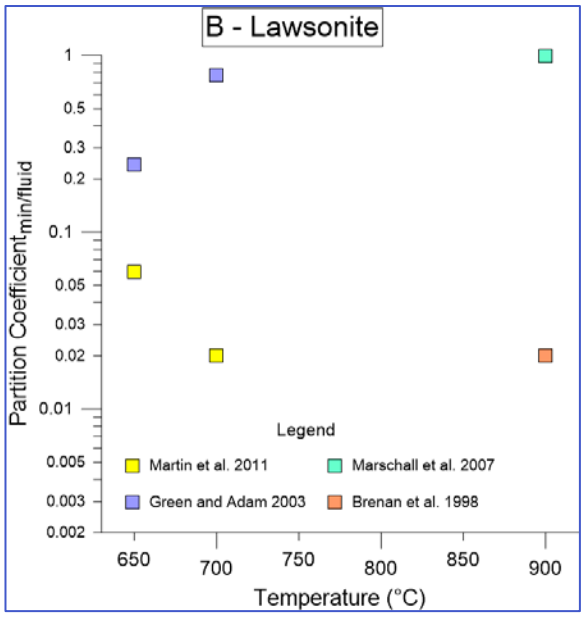


**Figure 16: Boron partitioning available data for lawsonite - fluid partitioning.**

Figure 16 is an example of available *Di* data for Boron with lawsonite. For this mineral, the data from Brenan et al. (1998) and Marshall et al. (2007) were discarded. In the study of Brenan et al. (1998), the calculation of the lawsonite–

fluid partitioning is very indirect, as it is calculated from amphibole-fluid partitioning that is, in itself, estimated from clinopyroxene–fluid partitioning. So the lawsonite *Di* will be dependent not only on amphibole–lawsonite partitioning but also on clinopyroxene–amphibole partitioning. Marschall et al. (2007) calculate the lawsonite–fluid partitioning by using the data from Marschall et al. (2006) and Brenan et al. (1998). In the first study, the metamorphic rocks were exposed to a maximum temperature of 500˚C, and in the second study, the clinopyroxene-fluid partitioning was determined at 900˚C. Consequently, the significant difference between the temperatures of these two studies makes the data not suitable for temperature dependent models.

The lawsonite–fluid partition coefficient was directly analysed only in two studies, by Green & Adam (2003) and Martin et al. (2011). The temperature conditions of these two studies are the same and although the partition coefficients from both papers have similar behaviour, in Green & Adam (2003), the composition of the run products is a mixture of several minerals, while in Martin et al. (2011) the run product is only lawsonite. In consequence, Martin et al. (2011) partition coefficient data are preferred, as they represent only the interaction between the lawsonite and fluid, and the *Di* values are not buffered by other minerals. However, for the prediction of HFSE, Y and U partition coefficients from both Martin et al. (2011) and Green & Adam (2003) are used, since Martin et al. (2011) have just one *Di* value determined. For the other trace elements, I only used the data of Martin et al. (2011).

### *3.4.2 Di coefficients and results*

The temperature dependence of the trace element partition coefficients is calculated only with two data points, due to the limited database for this mineral, so the coefficients of determination for these data (for which $R^2 = 1$ always) are not representative. Table 10 contains all the coefficients for the exponential regressions used in these predictions.

From the available data for lawsonite, the partition coefficients of trace elements in the same group exhibit similar behaviour (Figure 17). For most of the trace elements, the partition coefficients have an inverse correlation with temperature. tin, uranium, vanadium and chromium are the exceptions (Figure 17, f and g). It is important to mention that within 50˚C, the variation of the *Di* values for the transition metals is significant, increasing from 101 to 710 and from 116 to 979 for vanadium and chromium, respectively. lithium´s partition coefficient decreases by three orders of magnitude over only 50˚C. For the rest of the trace elements, there is less variation in the partition coefficient values.

| Element | Coefficients | $R^2$ | Element | Coefficients | $R^2$ |
|---|---|---|---|---|---|
| **La** | a = -0.0135 | 1 | **Li** | a = -0.1104 | 1 |
| | b = 9.8576 | | | b = 69.4764 | |
| **Ce** | a = -0.0204 | 1 | **Be** | a = -0.0459 | 1 |
| | b = 14.7422 | | | b = 31.6267 | |
| **Pr** | a = -0.0071 | 1 | **Ga** | a = -0.0152 | 1 |
| | b = 5.9229 | | | b = 12.4301 | |
| **Nd** | a = -0.0108 | 1 | **Ta** | a = -0.0280 | 1 |
| | b = 8.3185 | | | b = 22.1024 | |
| **Sm** | a = -0.0185 | 1 | **V** | a = 0.039 | 1 |
| | b = 13.1385 | | | b = -20.73676 | |
| **Eu** | a = -0.01318 | 1 | **Cr** | a = 0.0427 | 1 |
| | b = 10.0204 | | | b = -22.9746 | |
| **Gd** | a = -0.0179 | 1 | **Nb** | a = -0.0499 | 1 |
| | b = 12.6811 | | | b = 35.4893 | |
| **Tb** | a = -0.0181 | 1 | **Sn** | a = 0.0048 | 1 |
| | b = 12.74289 | | | b = 0.6833 | |
| **Dy** | a = -0.0198 | 1 | **U** | a = 0.00899 | 1 |
| | b = 13.8536 | | | b = -1.6601 | |
| **Ho** | a = -0.02085 | 1 | **Pb** | a = -0.0091 | 1 |
| | b = 14.5149 | | | b = 9.2518 | |
| **Er** | a = -0.0212 | 1 | **Rb** | a = -0.01833 | 1 |
| | b = 14.7121 | | | b = 6.6135 | |
| **Tm** | a = -0.0223 | 1 | **Sr** | a = -0.0116 | 1 |
| | b = 15.3694 | | | b = 6.1513 | |
| **Yb** | a = -0.0191 | 1 | **B** | a = -0.02197 | 1 |
| | b = 13.2718 | | | b = 11.4685 | |
| **Lu** | a = -0.0231 | 1 | **Ba** | a = -0.0563 | 1 |
| | b = 15.7985 | | | b = 34.2718 | |
| **Y** | a = -0.0203 | 1 | **Th** | a = -0.0185 | 1 |
| | b = 14.1562 | | | b = 12.0071 | |

**Table 10: Results from the exponential regressions for the trace elements of lawsonite, with Di=exp(aT+b).**

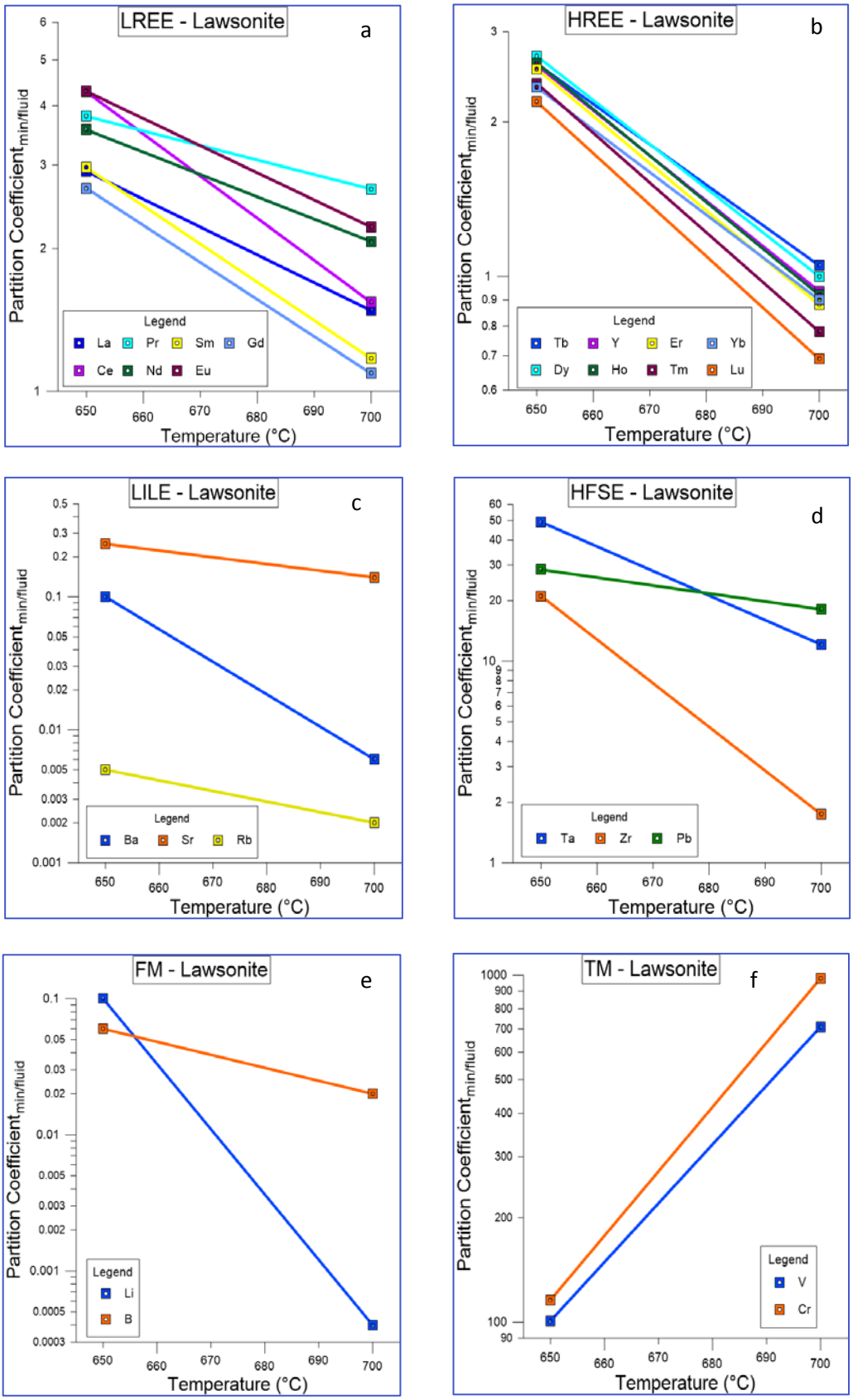


**Figure 17: Diagram with partition coefficients plotted against temperature for: a) Light Rare Earth elements; b) Heavy Rare Earth elements; c) Large-Ion Lithophile elements; d) High Field-strength elements; e) Fluid Mobile elements; f) Transition metals; and g) Post-transition metals. The data is from Green & Adam (2003) and Martin et al. (2011). The squares represent the available data and the lines are their respective fit.**

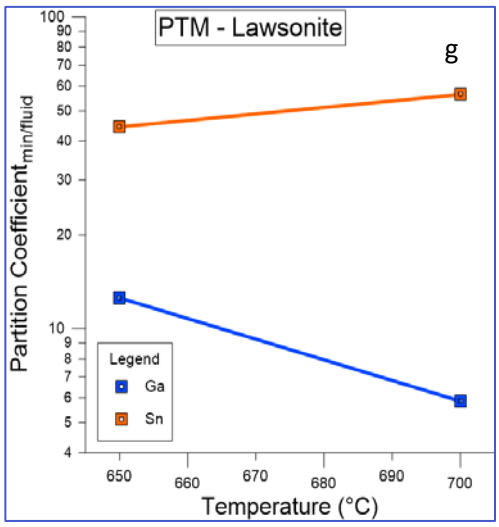


**Figure 17: Continuation.**

## 3.5 Rutile

### *3.5.1 General information*

Rutile is the most common titanium dioxide ($TiO_2$) polymorph (minerals with same chemical composition but different crystal structure). It is an accessory mineral that is common in igneous and some high-grade metamorphic rocks, such as amphibolite and eclogites. During metamorphic processes, rutile can be produced by heating anatase (another titanium dioxide polymorph) to above 730°C. Rutile has a large stability field, with a melting point above 1825°C (Deer et al. 1992), and controls fractionation of HFSE.

Even residual rutile in the system will host all $Ti^{4+}$, $Ta^{5+}$ and $Nb^{5+}$ (Jenner et al. 1993; Green & Hermann 2002; Adam 2003; El Korh et al. 2009; Schmidt & Poli 2013). Increasing the temperature will lower the partition coefficients for Nb and Ta (Brenan et al. 1994). The initial rutile composition also controls the partitioning between the fluid and this mineral. Brenan et al. (1994) performed several tests on the influence of anions on the partitioning between the fluid and the rutile. They concluded that the addition of Cl (in the form of HCl and NaCl) has no significant effect on the *Di* values of Nb and Ta, but decreases the *Di* values of U and Th; on the other hand, $Al^{3+}$ ($Al_2O_3$) present in the fluid will increase the partition coefficient of Nb and Ta.

### *3.5.2 Di coefficients and results*

| Element | *Di* (Min/Fluid) |
|---|---|
| Hf | 94 |
| Zr | 206 |
| U | 89 |
| Th | 0.1 |

**Table 11: Constant values of rutile-fluid partitioning.**

Rutile–fluid partitioning data was found only in Brenan et al. (1994) and only for HFSE. The partition coefficient of uranium, hafnium, zirconium and thorium has only one data point, so the *Di* for these elements will be taken as fixed, due to the lack of more data (Table 11). From HFSE, it was only possible for tantalum and niobium to formulate temperature-dependent regressions. The partition coefficient behaviour for these two trace elements has an inverse correlation with the temperature (Figure 18, Table 12).

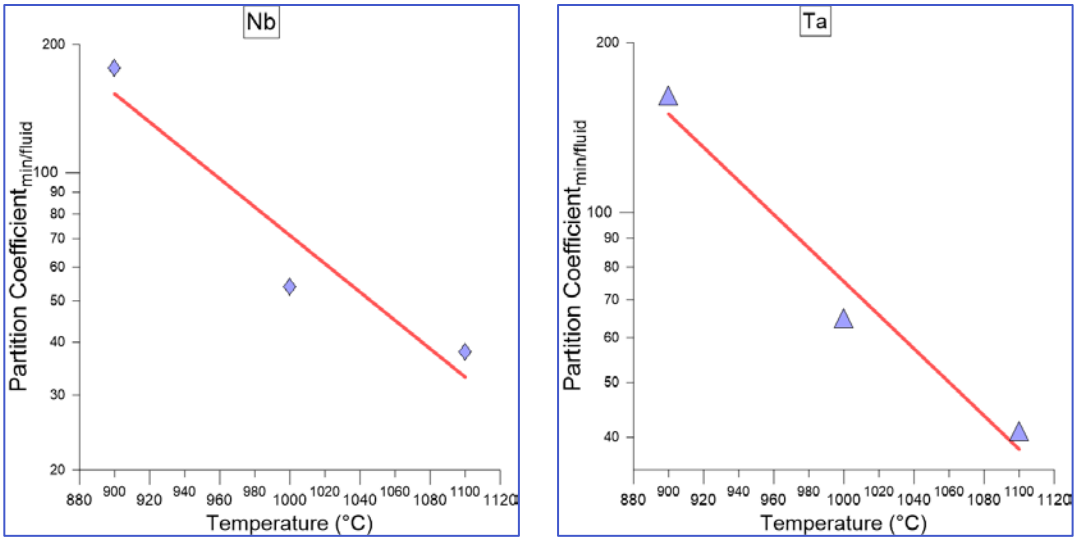


**Figure 18: Partition coefficients for Nb and Ta have an inverse behaviour with temperature. The data is from Brenan et al. (1994). The $R^2$ is 0.9109 and 0.9657 for Niobium and Tantalum, respectively.**

| Element | Coefficients | $R^2$ |
|---|---|---|
| **Nb** | a = -0.00766 | 0.9109 |
| | b = 11.9302 | |
| **Ta** | a = -0.0068 | 0.9657 |
| | b = 11.1623 | |

**Table 12: Results from the linear regressions for the trace elements of rutile, with Di=exp(aT+b). The prediction models use data from Brenan et al. (1994).**

## 3.6 Epidote

### *3.6.1 General information*

Zoisite is one of the most common epidote minerals, with structure formula $Ca_2Al_2O.AlOH(Si_2O_7)(SiO_4)$. Epidotes can be found in metabasalts, between blueschist and eclogite facies conditions (Peacock 1993). The pressure and temperature stability of zoisite can be located between the breakdown of lawsonite and the solidus (Schmidt & Poli 1994; Schmidt & Poli 2013); i.e. pressures until 3 GPa and temperatures between 400°C and 1200°C ( Boettcher 1970; Martin et al. 2011).

$$\text{zoisite + kyanite + quartz} \rightleftarrows \text{anorthite + } H_2O \quad (3.10)$$

$$\text{zoisite + tremolite} \rightleftarrows \text{hornblende + diopside + quartz + H2O} \quad (3.11)$$

At low pressure (below 1 GPa), the breakdown of zoisite releases water without producing other hydrous minerals (reaction 3.10; Jenkins et al. 1985). Above 700°C, the breakdown of zoisite can produce new hydrous minerals (reaction 3.11; Poli & Schmidt 2004).

This mineral may contain a large amount of trace elements like REEs, Th, U, Pb and Sr, and it is more enriched in LREE and MREE compared to HREE ( Brunsmann et al. 2001; Zack et al. 2002; Martin et al. 2011). Zack et al. (2002) observed that under eclogite conditions epidote could easily take non-negligible quantities of Sr into its structure. Martin et al. (2011) observed that REEs start to be strongly compatible with zoisite at temperatures above 700°C. The presence of residual epidote in the slab can control most of the budget of Th and LREE in the system (Manning 2004), so characterizing the zoisite-fluid interaction is important for a better understanding of fluid compositions.

Feineman et al. (2007) observed that, at low temperatures, the partition of trace elements is more extreme in individual zoisite dehydration reactions than in zoisite-bearing eclogite. The breakdown of zoisite will release a fluid that is enriched in Sr, Pb, and LREE.

The data used for the *Di* predictive models for all trace elements are from Brunsmann et al. (2001), Feineman et al. (2007) and Martin et al. (2011). Figure 19 shows all data for the partition coefficient of strontium for this mineral. It is evident that the two studies show different trends. Strontium is the only trace element showing such discrepancy. The data from Martin et al. (2011) is composed only of two data points while the study of Feineman et al. (2007) has five data points. For this reason, the data from Feineman et al. (2007) was used to determinate strontium behaviour in response to temperature increase.

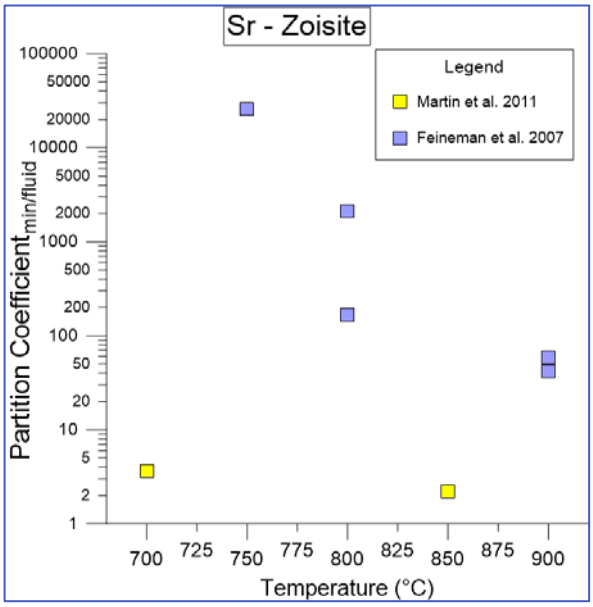


**Figure 19: Strontium's available data for clinopyroxene-fluid partitioning.**

### *3.6.2 Calculation of the missing REE data*

For the prediction of *Di* as a function of ionic radius for the missing REE, exponential and polynomial regressions are the two type that best describe the partition coefficient behaviour. An exponential regression fits the data best for the 550°C and 900°C data (Figure 20-a and d, respectively). A second-order degree polynomial equation is the best fit for the data at 750 and 800°C (Figure 20-b and c, respectively). Table 13 contains all the coefficients and the $R^2$ from these predictions.

Figure 20 shows that, at 550˚C, the *Di* have apparent exponential behaviour when plotted against the ionic radius, while after that a polynomial regression best explains the *Di* behaviour at 750˚C and 800˚C. Finally, at 900˚C, an exponential regression best explains the *Di* behaviour when plotted against the ionic radius. For 550˚C, the data used to predict the mineral-fluid partition coefficient behaviour, is only from LREE. The lack of HREE *Di* data at this temperature makes it difficult to speculate on the actual pattern of the all REE partition coefficient behaviour when plotted against the ionic radius. It is possible that the REE Di behaviour at 550˚C is polynomial, but due to the absence of HREE *Di* data, the regression type that best applies to the data is an exponential one.

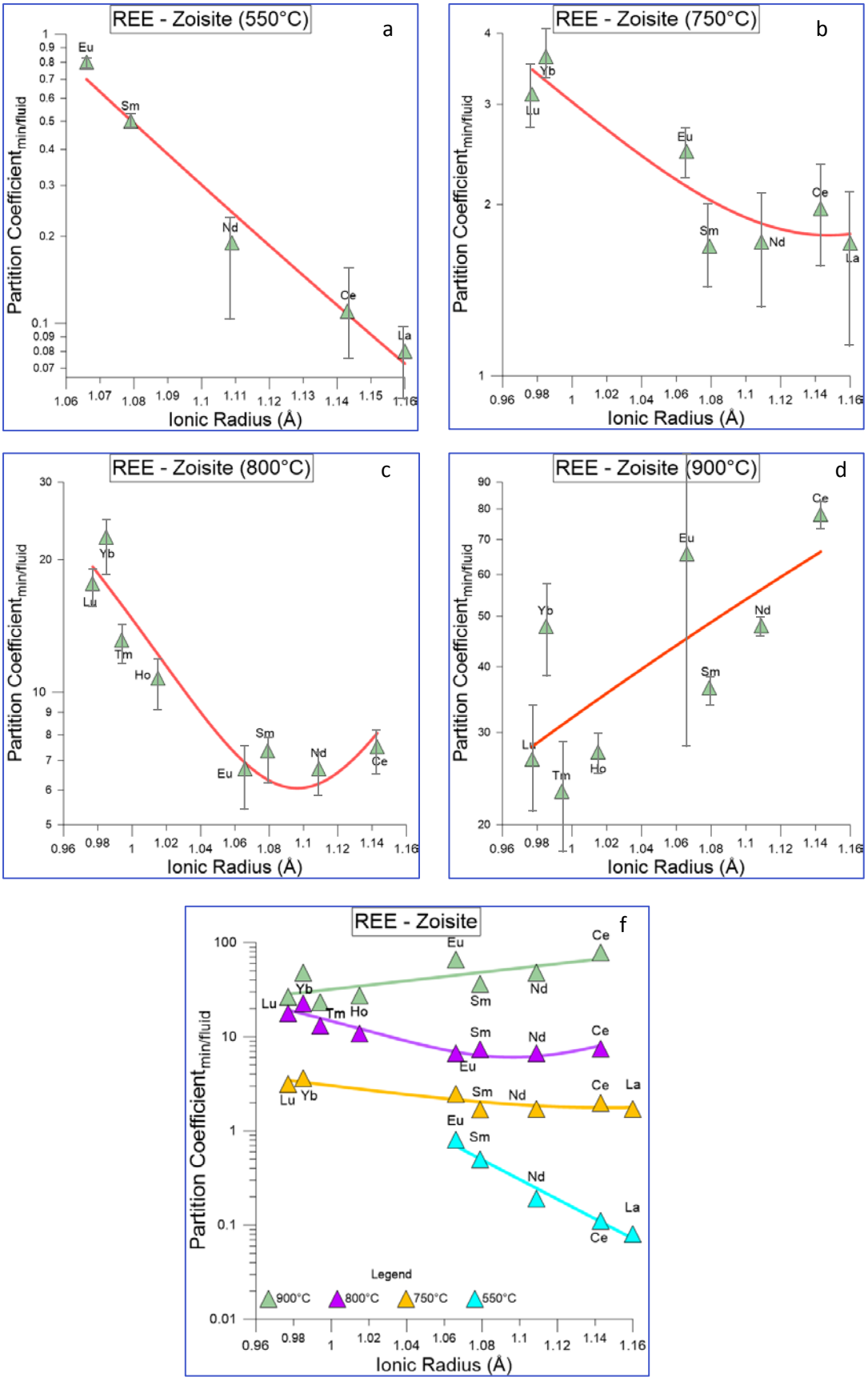


**Figure 20: REE's partition coefficient behaviour against ionic radius. a) at 500°C with exponential regression and data from Brunsmann et al. (2001); b) at 750°C with second-degree polynomial regression and data from Feineman et al. (2007); c) 800°C with second-degree polynomial regression and data from Feineman et al. (2007); d) 900°C with exponential regression and data from Feineman et al. (2007). The symbols represent the available data for each temperature and the red line is the best-fit curve associated with these data. g) contains the all REE´s partition coefficients plotted together. The set of whiskers represents the analytical error from respective paper. The plotted elements have 3+ valency.**

| T | Coefficients | $R^2$ |
|---|---|---|
| 550 | a = -24.073 | 0.9744 |
| | b = 25.293 | |
| 750 | a = 21.617 | 0.8379 |
| | b = - 49.871 | |
| | c = 29.336 | |
| 800 | a = 74.826 | 0.9275 |
| | b = -164.385 | |
| | c= 92.1696 | |
| | b = 6.785 | |
| 900 | a = 5.1997 | 0.5329 |
| | b = -1.7366 | |

**Table 13: The coefficients and the $R^2$ resulting from the polynomial and exponential regressions used for the prediction of the missing REE. For 750˚C and 800˚C, the equation used is $Di=\exp(ar_i^2+br_i+c)$. Finally, for 550˚C and 900˚C, the equation used is $Di=\exp(ar_i+b)$.**

### *3.6.3 Di coefficients and results*

Exponential equations are used to calculate the temperature-dependent partition coefficient behaviour. In general, the prediction models are not so good in comparison to the other discussed minerals. Three of the predictions have $R^2$ under 0.6, and only four have $R^2$ over 0.9. Figure 21 shows three examples of the worst and the best fit produced for the prediction of *Di*'s behaviour. Table 14 contains all the coefficients and the $R^2$ that results from these predictions. Where the exponential regressions are calculated only with two data points the $R^2 = 1$ is not meaningful.

The partitioning of trace elements in the same group exhibits similar behaviour (Figure 22). The *Di* behaviour, for most of the trace elements, has a direct correlation with temperature, with the exception of barium and strontium from the LILEs; lead, tantalum and niobium from the HFSEs (Figure 22, a and b); and beryllium and gadolinium from Earth metals and post-transition metals (PTM), respectively. The decrease of the partition coefficient of strontium and the increase of the partition coefficient of some LREE is significant, by three orders of magnitude within only 150˚C.

| Element | Coefficients | $R^2$ | Element | Coefficients | $R^2$ |
|---|---|---|---|---|---|
| La | a= 0.0186 | 0.7674 | Lu | a = 0.0172 | 0.7326 |
| | b= -13.6542 | | | b = -12.1101 | |
| Ce | a = 0.0172 | 0.7879 | Sr | a = -0.0423 | 0.9962 |
| | b= -12.199 | | | b = 41.6964 | |
| Pr | a = 0.0168 | 0.8263 | Rb | a = 0.0117 | 0.6431 |
| | b = -9.4122 | | | b = -13.4636 | |
| Nd | a = 0.0158 | 0.6599 | Pb | a = -0.0208 | 0.9889 |
| | b = -11.5146 | | | b = 18.6185 | |
| Sm | a = 0.013 | 0.5513 | Ba | a = -0.0172 | 0.9430 |
| | b = -9.0774 | | | b = 15.1324 | |
| Eu | a = 0.0124 | 0.5299 | Cs | a = 0.0107 | 1 |
| | b = -8.3964 | | | b = -13.7253 | |
| Gd | a = 0.0242 | 0.7778 | Li | a = 0.0019 | 1 |
| | b = -18.2584 | | | b = -7.1517 | |
| Tb | a = 0.0071 | 0.5365 | Be | a = -0.0036 | 1 |
| | b = -4.123 | | | b = 0.3951 | |
| Dy | a = 0.0232 | 0.9222 | Ga | a = -0.0093 | 1 |
| | b = -17.0307 | | | b = 8.2725 | |
| Y | a = 0.0241 | 0.8933 | U | a = 0.0023 | 1 |
| | b = -17.7467 | | | b = -1.8403 | |
| Ho | a = 0.0195 | 0.7806 | Hf | a = 0.0042 | 1 |
| | b = -14.2036 | | | b = -3.1787 | |
| Er | a = 0.0197 | 0.7903 | Nb | a = -0.01699 | 1 |
| | b = -14.2101 | | | b = 11.4511 | |
| Tm | a = 0.0172 | 0.7671 | Ta | a = -0.0172 | 1 |
| | b = -12.222 | | | b = 12.9424 | |
| Yb | a = 0.0191 | 0.7248 | | | |
| | b = -13.4256 | | | | |

**Table 14: Results from the linear regressions for the trace elements of zoisite, with Di=exp(aT+b).**

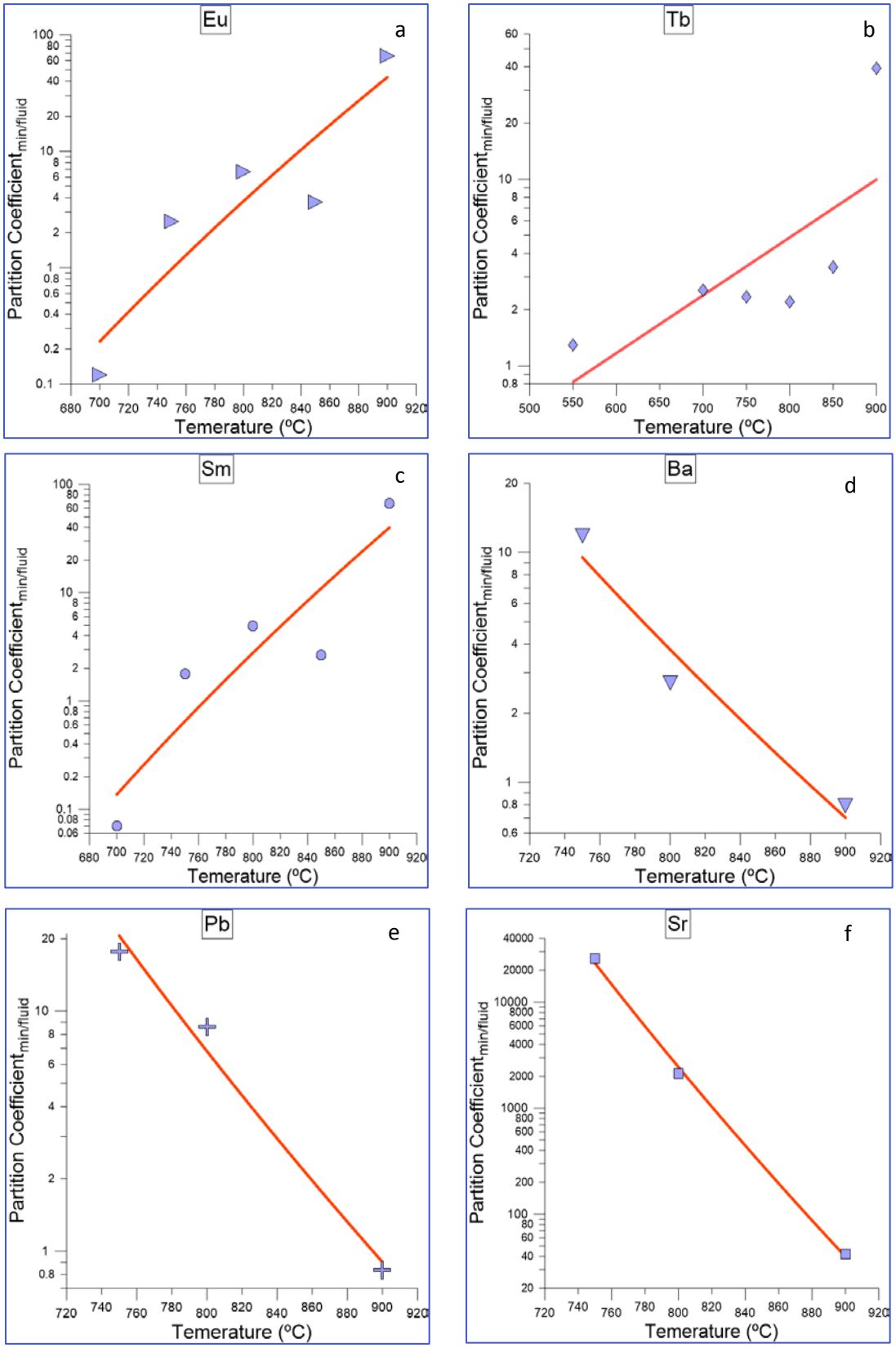


**Figure 21: The partition coefficient behaviour of 6 trace elements (three of the best and three of the worst fit) when plotted against temperature. a) Eu ($R^2$ = 0.5299) with data from Feineman et al. (2007) and Martin et al. (2011); b) Tb ($R^2$ = 0.5365) with data from Brunsmann et al. (2001), Feineman et al. (2007) and Martin et al. (2011); c) Sm ($R^2$ = 0.5513) with data from Feineman et al. (2007) and Martin et al. (2011); d) Ba ($R^2$ = 0.9430) with data from Brunsmann et al. (2001), Feineman et al. (2007) and Martin et al. (2011); e) Pb ($R^2$ = 0.9889) with data from Feineman et al. (2007) and Martin et al. (2011); and f) Sr ($R^2$ = 0.9962) with data from Feineman et al. (2007) and Martin et al. (2011). The symbols represent the available data for each element and the red line is the best-fit associated to these data.**

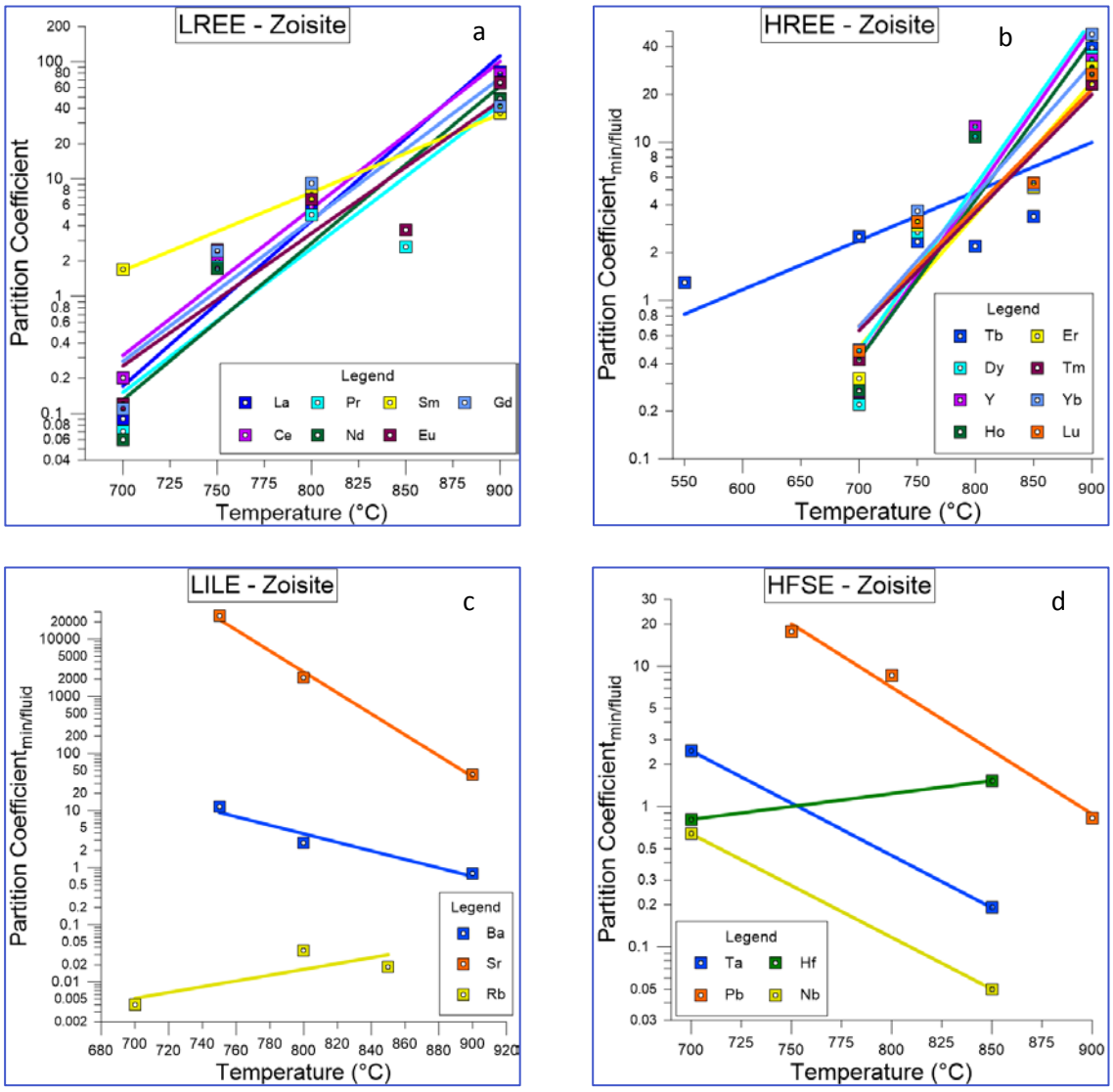


**Figure 22: Diagram with partition coefficient plotted against the temperature for: a) Light Rare Earth elements; b) Heavy Rare Earth elements; c) Large-ion Lithophile elements; d) Highfield-strength elements; The data is from Brunsmann et al. (2001), Feineman et al. (2007) and Martin et al. (2011). The squares and lines represent the available data and the respective fit lines.**

## 3.7 Other minerals

In addition, the methodology described in Chapter 2 was used for the formulation of temperature dependent partition coefficients for orthopyroxene and olivine. These minerals are not stable in the considered chemical system (i.e. the subducted oceanic crust), so their mineral-fluid partition coefficient is not relevant for the calculation of the trace elements composition of the slab crust fluids. Nonetheless, such partition coefficients can be useful to calculate the composition of a mantle metasomatized by slab fluids, and for this reason, all related information for these two minerals is added in the Appendix section in this dissertation.

## 3.8 Summary

This chapter contains the results from the formulation of temperature dependent regressions for the calculation of partition coefficients between different minerals and fluid. The influence of temperature is determined for six key minerals, representing the typical mineralogy of an altered subducted K-free basaltic oceanic crust. In general, with increasing temperature, most of the elements become more compatible with the fluid. Zoisite is the only mineral for which most of the trace elements become more compatible with this mineral with increasing temperature.

For amphibole, Equation 2.5 is used to acquire partition coefficient data, but due to the lack of data, only two points are used in the formulation of the temperature-dependent regression. The atomic radius influence on the *Di* is used for the calculation of the missing trace element *Di* values. For 650˚C, the extrapolation of these values is done for three elements, Ce, Nd and Sm, while for 920˚C, this extrapolation is used to determine the *Di* values for Pr, Tb, Er, Tm and Lu. Amphibole-fluid *Di* values for the studied trace elements decrease with increasing temperature, and this leads to an increase in the concentration of these elements in the fluid.

The clinopyroxene trace element partition coefficients are extrapolated from garnet. Pr, Tb, Ho and Tm are the trace elements for which the *Di* value is extrapolated for clinopyroxene. In general, the clinopyroxene–fluid partitioning has an inverse correlation with temperature, except scandium, rubidium, caesium and boron, which become more compatible with clinopyroxene with increasing temperature.

*Di* value of Pr, Tb, Ho and Tm are extrapolated for garnet. Most of the trace elements *Di* values of garnet have an inverse correlation with temperature, except for rubidium, yttrium, scandium and caesium, for which partition coefficients (slightly) increase.

Increasing temperature makes vanadium, uranium and chromium more compatible with lawsonite. The *Di* of V and Cr increases by about a factor 7 within a 50˚C temperature change, while lithium Di values decrease by three orders of magnitude over this range.

Rutile is a mineral that retains large amounts of HFSE in its structure. Due to the lack of data for rutile–fluid partition coefficients, even for HFSE, the *Di* values of Hf, U, Zr and Th are fixed (Table 11) and temperature dependent *Di* values are calculated only for Tantalum and Niobium, for which the *Di* decreases with increasing temperature.

Contrary to the minerals mention above, most of the trace elements become more compatible with zoisite as temperature increases. The elements Ba, Sr, Pb, Ta, Nb, Ga, and Be have an inverse correlation with temperature, while the *Di* value for strontium decreases with three orders of magnitude within 150 ˚C.

The paucity of mineral-fluid partitioning data limits the level of detail to which the temperature dependence of fluid-mineral *Di* values can be parameterised. However, this Chapter shows that even

the limited available data is often sufficient to create regressions that reliably characterise the temperature influence over the *Di*.

# 4. Application

## 4.1 Introduction

This chapter is an application of the temperature-dependent partition coefficients elaborated in Chapter 3. One of the goals of this dissertation is to formulate a model that calculates a possible composition of slab fluids derived from a K–free basaltic oceanic crust. Through a combination of Matlab and Perple_X software applications, I present a simple numerical model to calculate a possible composition of the slab fluids based for two actual subduction zones: the Marianas and Vanuatu. The Marianas represent a cold subduction zone (~150 Ma subducting Pacific plate), whereas Vanuatu represents a hot subducting system, where the Coral Sea plate, which is younger than 50 Ma, is subducting. The fluid signature is partly recorded in the arc primitive melts, and a direct comparison of LILE and FM elements between primitive IAB rocks and modelled fluids can provide a first order examination of the parameterisation derived in this dissertation. Primitive IAB rocks are used for this comparison [for Mg# > 65, where Mg# = Mg/(Mg+$Fe^{2+}$), and $Fe^{2+}$ is being recalculated when not measured with $Fe_2O_3$/FeO=0.2] so that they represent the mantle source metasomatized by slab fluids. In this case the LILE and FM elements concentrations are not far to represent the net additions of slab derived component as those elements are barely present in mantle rocks (e.g. Pearce et al. 2005).

Although the exact trace element composition of the slab fluids may be unknown, some trace element ratios of primitive IAB can be taken as indirect evidence of fluid interaction during the formation of the IAB magmas. Elements such as Ba, Sr, Li and B are transferred from the subducted oceanic crust to the mantle wedge. The anomalously high concentrations of these elements in the primitive melts result from slab dehydration processes, and only a minor quantity derives from the mantle source (Elliott 2003). Different trace element ratios can be used as a proxy for different types of rock reservoir (e.g. Pearce & Peate 1995; Pearce et al. 2005). For example, high La/Sm and Th/Yb ratio represent a sediment melt input ( Elliott 2003; Pearce et al. 2005; Ribeiro et al. 2013). On the other hand, the ratio between fluid mobile and fluid immobile elements, such as Ba/Ta, and Ba/Yb, are a good proxy for a shallow subduction component (Pearce et al. 2005; Pearce & Stern 2006; Ribeiro et al. 2013) representing the dehydration of the oceanic crust. Ba/Yb, Nb/Yb and Th/Yb ratios are used in section 4.3 of this chapter, to examine whether the fluids modelled in this dissertation are similar to those involved in the formation of IAB of the Marianas and Vanuatu.

The Northern Mariana subduction zone is part of the 2500 km long Izu-Bonin-Mariana subduction system (Lin et al. 1989). There, 150-Myr old Jurassic crust (Elliott et al. 1997; van Keken et al. 2011) is subducted underneath the Philippines sea plate with a convergence rate of 1.53 to 4 cm/yr (Elliott et al. 1997; Elliott 2003 Syracuse et al. 2010; van Keken et al. 2011). The oceanic crust

has a thickness of 6 km (Yamazaki et al. 2003), and since no nearby continents provide sediments, the thickness of the sediments is only around 0.2 km (Woodhead 1989; Syracuse et al. 2010; van Keken et al. 2011). The sediments are composed of pelagic clay (rich in REE), terrigenous turbidites (rich in U, Th and alkalis such as Rb and K) and biogenic oozes that can contain large amounts of Ba and Sr (Plank & Langmuir 1998). There is no evidence of sedimentary accumulation in the accretionary prism, which suggests that all sediments are subducted in the Mariana Trench (Elliott et al. 1997). The slab dip is shallow in the first 100 km depth and after that increases to almost 90˚ towards the transition zone (Sinton & Fryer 1987). The oceanic crust dehydration of this subduction zone occurs between 50 and 100 km (Pozgay et al. 2009). Sinton & Fryer (1987) conclude that, relative to a MORB source, the Mariana trough rock source is enriched, with concentrations in the following order: Ba > Rb > K > LREE > Sr, while it is relatively depleted in Y. The Ba/Nb ratio of general MORB rocks and sediments from the Mariana trench is around 4 and 19, respectively (Stern et al. 2006; Ribeiro et al. 2013). In order to compare the resulting fluid composition from my model with primitive arc basalts from this subduction zone, data from Kent & Elliott (2002), Stern et al. (2006) and Tamura et al. (2014) are used. Primitive IAB data from Kent & Elliott (2002) have Ba/Yb=41-196, Nb/Yb=0.26-0.34 and Th/Yb≈0.11. The data from Stern et al. (2006) have Ba/Yb=60-63, Nb/Yb=0.29-1.12 and Th/Yb=0.17-0.60. Finally, the data from Tamura et al. (2014) have the following values: Ba/Yb =66-82, Nb/Yb=0.19-0.35 and Th/Yb=1.02-1.34.

The Vanuatu subduction zone is a 1200-km-long trench where the Australian plate is subducting under the Pacific plate and is extending across the Southwest Pacific, between Ureparapara Island in the North and Hunters island in the South (Williams et al. 1974; Sorbadere et al. 2013; Beaumais et al. 2016). The 44-Myr old oceanic crust is subducted with a rate of 1.53 to 12 cm/yr (Syracuse et al. 2010; van Keken et al. 2011; Beaumais et al. 2016). The thickness of the sediments layer is between 0.2 and 0.65 km (Pearce & Peate 1995; Syracuse et al. 2010; van Keken et al. 2011) The subduction interface has a shallow dip, less than 15° over the first 20 - 40 km depth, and, beyond 40 km, it rapidly increases to approximately 40° (Baillard et al. 2015). The slab starts to lose its water around 40 km, but the dehydration peak is reached around 75 km depth (Baillard et al. 2015). This subduction zone has a sediment influx that is high in K and low in Ba relatively to other arcs (Peate et al. 1997). Data from Turner et al. (1999) and Sorbadere et al. (2011; 2013) are used to compare the fluid composition that results from my model with primitive arc basalts from this subduction zone. Primitive IAB data used from Kent & Elliott (2002) have the following values: Ba/Yb =91, Nb/Yb=0.49 and Th/Yb=0.167. The data from Sorbadere et al. (2011) have Ba/Yb=77-268, Nb/Yb=0.61-1.19 and Th/Yb=0.26-1.41. Finally, the data from Sorbadere et al. (2013) suggest Ba/Yb =31-150, Nb/Yb=0.6-6.3 and Th/Yb=0.12-0.89.

## 4.2 Methods for the calculation of the slab fluids

### *4.2.1 General information*

In this section, the methodology is given for the calculation of trace element fluid compositions by applying the temperature-dependent partition coefficients that are derived in this dissertation.

First, the PT paths for the two subduction zones are adopted from Syracuse et al. (2010) and imported into Perple_X (Connolly 2005) to establish the evolution of the mineral assemblage in the subducted oceanic crust. A Pacific K-free MORB composition in the $Na_2O$–CaO–FeO–MgO–$Al_2O_3$–$TiO_2$–$SiO_2$–$H_2O$ system is used as major element starting composition (Table 15). For the calculation of the trace element fluid composition, a fractional dehydration approach is used: when $H_2O$ is stable as a free phase, it is immediately extracted, under the assumption that it is in equilibrium with the calculated assemblage. In this dissertation, this corresponds to removing the fluid from the subducted oceanic crust each time step, i.e. immediately when the fluid is created.

| Subduction zone | Major element | w% | Subduction zone | Major element | w% |
|---|---|---|---|---|---|
| Mariana | $H_2O$ | 3.1 | Vanuatu | $H_2O$ | 3.1 |
| | $SiO_2$ | 50.25 | | $SiO_2$ | 50.74 |
| | $Al_2O_3$ | 15.02 | | $Al2O_3$ | 15.9 |
| | $TiO_2$ | 1.61 | | $TiO_2$ | 1.61 |
| | FeO | 9.84 | | FeO | 9.2 |
| | MgO | 5.9 | | MgO | 5.6 |
| | CaO | 11.57 | | CaO | 12.25 |
| | $Na_2O$ | 2.61 | | $Na_2O$ | 2.61 |

**Table 15: Major element composition used in Perple_X for each subduction zones. The slight differences between them are to prevent the formation of hydrous minerals such as talc in the subducted oceanic crust mineral assemblage, which circumvents the problems related to the lack of data on their partition coefficients. The major element compositions are adapted from White & Klein (2013).**

The thermodynamic database used in the Perple_X calculation is adopted from Bouilhol et al. (2015). For each time step, Perple_X uses this thermodynamic database to calculate the stable mineral assemblage for the given composition and PT conditions. At the PT conditions when the hydrous minerals are not stable, Perple_X recalculates the mineral assemblage in a way that the free fluid is extracted from the system. This will lead to decrease, until a point where no hydrous mineral is stable. During this process, the amount of anhydrous minerals, with exception of rutile, will slowly increase.

A MATLAB script is created for the second step, in which the mineral and water fraction, calculated with Perple_X are used to calculate the bulk partition coefficients between the oceanic crust and fluids. So, for each time step, the bulk partition coefficient is calculated as:

$$Di_{BULK} = F_{MIN1}Di_{MIN1} + F_{MIN2}Di_{MIN2} + \cdots + F_{MINn}Di_{MINn} \quad (4.1)$$

where $F_{MINi}$ is the fraction of mineral $i$ at a specific temperature, $Di_{MINi}$ is the respective mineral–fluid partition coefficient at the same temperature, with $i$ between 1 and $n$.

Next, the trace element fluid composition is calculated using the bulk partition coefficient in the Rayleigh distillation equation:

$$X_{fluid/SLAB} = X_{SLAB} * \frac{1}{Di_{SLAB/FLUID}} * (1 - F_{fluid})^{\left(\frac{1}{Di_{SLAB}/_{FLUID}} - 1\right)} \quad (4.2)$$

where $X_{SLAB}$ is the trace element composition of the slab, $F_{fluid}$ is the weight fraction of the fluid released from the slab, given by Perple_X and $Di_{Slab/Fluid}$ is bulk rock partition coefficient at a specific temperature. The adapted Rayleigh distillation equation (Equation 4.2) is an exponential relation that describes the partitioning of a trace element between two systems and calculates the composition of the fluid that is released from the slab. Table 16 contains the trace element composition of an altered oceanic crust, used in Equation 4.2 (from Kelley et al. (2003), with the exception of Tm, Y and B which are from White & Klein (2013)).

| TE | ppm | TE | ppm | TE | ppm | TE | ppm |
|---|---|---|---|---|---|---|---|
| Rb | 13.7 | Pr | 2.06 | Y | 40.7 | U | 0.39 |
| Ba | 15.6 | Nd | 11.3 | Ho | 1.43 | Zr | 112 |
| Sr | 109 | Sm | 3.95 | Er | 4.09 | Hf | 3.07 |
| Li | 14.1 | Eu | 1.34 | Tm | 0.57 | Nb | 2.89 |
| B | 1.38 | Gd | 5.55 | Yb | 4.02 | Ta | 0.21 |
| La | 3.4 | Tb | 1.01 | Lu | 0.636 | Pb | 0.437 |
| Ce | 11.4 | Dy | 6.56 | Th | 0.173 | Be | 0.584 |

**Table 16: Initial bulk trace element composition of the subducted oceanic crust used in Rayleigh distillation equation for the calculation of the trace element composition of the slab fluids of the two natural examples. The values are from Kelley et al. (2003) and White & Klein (2013). TE=trace elements**

The altered oceanic basaltic crust can contain an elevated number of different accessory phases such as rutile, apatite and titanite. From all these accessory minerals, only data for rutile-fluid partition coefficients are available. White & Klein (2013) determined that the Pacific basaltic oceanic crust has between 1.61 and 1.71 wt% of $TiO_2$ in its composition, for my models, I used 1.61 wt% of $TiO_2$ in Perple_X. For each time step, Perple_X is recalculating the mineral assemblage considering the released fluid and always the 1.61 wt% of $TiO_2$, i.e. for each time step, the amount of hydrous minerals is decreasing with the increasing PT conditions and the mineral assemblage will have always approximately 1.61 wt% of rutile.

For each time step, Perple_X gives the density data of the system. This allows me to calculate the amount of water (Equation 4.3) released from 1 $m^3$ of rock, by applying cross multiplication between the density and the total wt.% of fluid released for each batch.

$$M = \frac{\rho * F_{fluid}}{100} \quad (4.3)$$

where *M* is the amount of water released from the system for each timestep, $F_{fluid}$ is the weight fraction of the fluid released from the slab and $\rho$ is the total density of the system for each time step.

### *4.2.2 Implications for the models*

Several factors can influence the trace element concentration in the fluids, such as pressure, temperature, initial trace element concentration in the oceanic crust, and dehydration rates.

As elucidated in the section 4.2.1 of this Chapter, the PT path is taken from Syracuse et al. (2010) and imported to Perple_X. Due to in limited data on the pressure influence on the mineral-fluid partition coefficient, the variation of the pressure was made dependent on the variation of temperature. This will allow to study the influence of the temperature on the trace element fluid composition.

Another factor that needs discussion is the influence of the dehydration rates of the oceanic crust. To investigate the degree of this influence, the trace element fluid concentration was calculated using Equation 4.2, at the same temperature (T = 489˚C), but using a different amount of fluid released from the oceanic crust, i.e. a different weight fraction of the fluid released from the slab. Table 17 shows that the dehydration rate of the basaltic oceanic crust does not influence the concentration of trace elements in the fluid. When changing the amount of water that will interact with the basaltic oceanic crust from 1.2761 x$10^{-5}$ to 1.2761 x$10^{-1}$ wt% of $H_2O$, the variation of trace element concentration in the fluids changes by less than 0.079 and 0.12%, even for fluid mobile elements such as B and Li, respectively.

To sum up, the all steps used in my models to calculate the composition of the fluids for each element are:

- When the fluid exists as a free phase in the system, the first thing that my model calculates is the bulk partition coefficient (Equation 4.1), i.e. the partition coefficient of each element between all minerals and the fluid. The Equation 4.1 is simple multiplication between the fraction of each mineral and the partition coefficient of specific element at specific temperature.;
- The second step is using the bulk *Di* in Equation 4.2. Rayleigh distillation equation uses the relationship between the bulk partition coefficient, the amount of trace elements existent in the slab and the amount of water released from the hydrous minerals. The amount of water does not influence the trace element concentration of the fluids.

| T | 489˚C | | | | |
|---|---|---|---|---|---|
| wt% $H_2O$ | 1.2761 x$10^{-5}$ | 1.2761 x$10^{-4}$ | 1.2761 x$10^{-3}$ | 1.2761 x$10^{-2}$ | 1.2761 x$10^{-1}$ |
| **Elements** | **X1** | **X2** | **X3** | **X4** | **X5** |
| **Rb** | 5.6322x$10^{2}$ | 5.6320 x$10^{2}$ | 5.6294 x$10^{2}$ | 5.6035 x$10^{2}$ | 5.3510 x$10^{2}$ |
| **Ba** | 5.4122x$10^{-2}$ | 5.4123 $10^{-2}$ | 5.4123x$10^{-2}$ | 5.4129x$10^{-2}$ | 5.4191x$10^{-2}$ |
| **Sr** | 1.2147 | 1.2147 | 1.2147 | 1.2149 | 1.2162 |
| **Li** | 1.3797x$10^{-5}$ | 1.3797x$10^{-5}$ | 1.3797x$10^{-5}$ | 1.3798x$10^{-5}$ | 1.3814x$10^{-5}$ |
| **B** | 1.2609 | 1.2609 | 1.2609 | 1.2609 | 1.2610 |
| **La** | 3.5984 x$10^{-2}$ | 3.5984 x$10^{-2}$ | 3.5985 x$10^{-2}$ | 3.5989 x$10^{-2}$ | 3.6030 x$10^{-2}$ |
| **Ce** | 5.0492 x$10^{-2}$ | 5.0492 x$10^{-2}$ | 5.0493 x$10^{-2}$ | 5.0499 x$10^{-2}$ | 5.0556 x$10^{-2}$ |
| **Pr** | 7.0036 x$10^{-3}$ | 7.0036 x$10^{-3}$ | 7.0037 x$10^{-3}$ | 7.0045 x$10^{-3}$ | 7.0125 x$10^{-3}$ |
| **Nd** | 3.4003 x$10^{-2}$ | 3.4003 x$10^{-2}$ | 3.4004 x$10^{-2}$ | 3.4008 x$10^{-2}$ | 3.4047 x$10^{-2}$ |
| **Sm** | 8.5722 x$10^{-3}$ | 8.5722 x$10^{-3}$ | 8.5723 x$10^{-3}$ | 8.5732 x$10^{-3}$ | 8.5831 x$10^{-3}$ |
| **Eu** | 3.5873 x$10^{-3}$ | 3.5873 x$10^{-3}$ | 3.5873 x$10^{-3}$ | 3.5877 x$10^{-3}$ | 3.5919 x$10^{-3}$ |
| **Gd** | 9.6582 x$10^{-3}$ | 9.6582 x$10^{-3}$ | 9.6583 x$10^{-3}$ | 9.6594 x$10^{-3}$ | 9.6705 x$10^{-3}$ |
| **Tb** | 2.4162 x$10^{-3}$ | 2.4162 x$10^{-3}$ | 2.4162 x$10^{-3}$ | 2.4165 x$10^{-3}$ | 2.4193 x$10^{-3}$ |
| **Dy** | 1.8097 x$10^{-2}$ | 1.8097 x$10^{-2}$ | 1.8097 x$10^{-2}$ | 1.8099 x$10^{-2}$ | 1.8120 x$10^{-2}$ |
| **Y** | 2.7108 x$10^{-1}$ | 2.7108 x$10^{-1}$ | 2.7108 x$10^{-1}$ | 2.7111E x$10^{-1}$ | 2.7142 x$10^{-1}$ |
| **Ho** | 3.2748 x$10^{-3}$ | 3.2749 x$10^{-3}$ | 3.2749 x$10^{-3}$ | 3.2753 x$10^{-3}$ | 3.2790 x$10^{-3}$ |
| **Er** | 1.1515 x$10^{-2}$ | 1.1515 x$10^{-2}$ | 1.1515 x$10^{-2}$ | 1.1516 x$10^{-2}$ | 1.1529 x$10^{-2}$ |
| **Tm** | 1.2359 x$10^{-3}$ | 1.2359 x$10^{-3}$ | 1.2359 x$10^{-3}$ | 1.2361 x$10^{-3}$ | 1.2375 x$10^{-3}$ |
| **Yb** | 7.2547 x$10^{-3}$ | 7.2547 x$10^{-3}$ | 7.2548 x$10^{-3}$ | 7.2556 x$10^{-3}$ | 7.2640 x$10^{-3}$ |
| **Lu** | 1.1665 x$10^{-3}$ | 1.1665 x$10^{-3}$ | 1.1665 x$10^{-3}$ | 1.1666 x$10^{-3}$ | 1.1680 x$10^{-3}$ |
| **Th** | 5.8726 x$10^{-4}$ | 5.8727 x$10^{-4}$ | 5.8727 x$10^{-4}$ | 5.8734 x$10^{-4}$ | 5.8801 x$10^{-4}$ |
| **U** | 3.9051 x$10^{-3}$ | 3.9051 x$10^{-3}$ | 3.9052 x$10^{-3}$ | 3.9056 x$10^{-3}$ | 3.9101 x$10^{-3}$ |
| **Zr** | 9.7753 x$10^{-2}$ | 9.7753 x$10^{-2}$ | 9.7755 x$10^{-2}$ | 9.7766 x$10^{-2}$ | 9.7878 x$10^{-2}$ |
| **Hf** | 2.9266 x$10^{-3}$ | 2.9266 x$10^{-3}$ | 2.9266 x$10^{-3}$ | 2.9269 x$10^{-3}$ | 2.9303 x$10^{-3}$ |
| **Nb** | 1.8374 x$10^{-4}$ | 1.8374 x$10^{-4}$ | 1.8374 x$10^{-4}$ | 1.8376 x$10^{-4}$ | 1.8397 x$10^{-4}$ |
| **Ta** | 2.0819 x$10^{-5}$ | 2.0819 x$10^{-5}$ | 2.0819 x$10^{-5}$ | 2.0821 x$10^{-5}$ | 2.0845 x$10^{-5}$ |
| **Pb** | 1.5594 x$10^{-2}$ | 1.5594 x$10^{-2}$ | 1.5595 x$10^{-2}$ | 1.5596 x$10^{-2}$ | 1.5614 x$10^{-2}$ |
| **Be** | 2.9175 x$10^{-4}$ | 2.9175 x$10^{-4}$ | 2.9175 x$10^{-4}$ | 2.9179 x$10^{-4}$ | 2.9212 x$10^{-4}$ |

**Table 17: Results from the calculation of the trace fluid composition calculated at the same temperature (489˚C) but different amount of water.**

## 4.3 Results

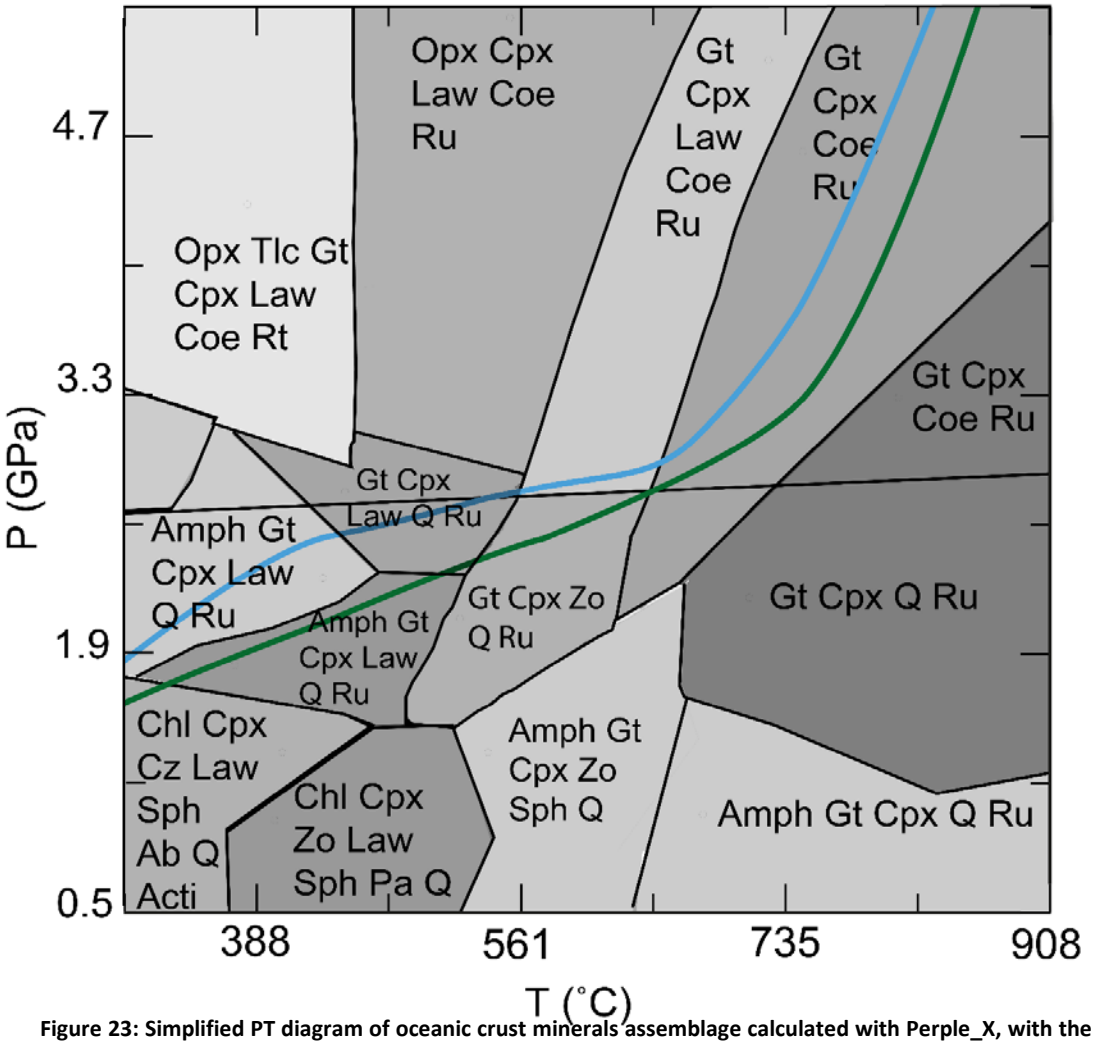


**Figure 23: Simplified PT diagram of oceanic crust minerals assemblage calculated with Perple_X, with the PT path of Mariana and Vanuatu subduction zones from Syracuse et al. (2010). The blue line represents the PT path of the Mariana subduction zone and the green line shows the PT path of the Vanuatu subduction zone. T=temperature, P=pressure, Ab=albite, Acti=actinolite, Amph=amphibole, Chl=chlorite, Cz=clinozoisite, Coe=coesite, Cpx=clinopyroxene, Gt=garnet, Law=lawsonite, Q=quartz, Ol=olivine, Opx=orthopyroxene, Pa=paragonite, Ru=rutile, Sph=sphene, Tlc=talc and Zo=zoisite**

A simplified PT diagram of a K-free mineral assemblage calculated with Perple_X and the PT path of the two subduction zones is shown in Figure 23. The higher temperature of the Vanuatu oceanic slab allows the formation of amphibole, lawsonite and zoisite as major hydrous phases, while the hydrous minerals in the Mariana subducted oceanic crust are amphibole and lawsonite. For the calculation of the amount of water released from the system, Equation 4.3 was used.

This section is divided into 3 subsections. The first two of the subsections contain the results for Mariana and Vanuatu subduction zones, respectively. The evolution of the fluid composition will be shown from the first fluid released in the shallow depths until the breaking down of the last hydrous mineral that will produce the last fluid. The third section contains general results of both

areas, in which I compare the calculated results with the compositions of primitive IAB and other rocks found in the two subduction systems.

### *4.3.1 Northern Mariana*

Based on the Perple_X calculations, the dehydration of the oceanic crust of the northern Marianas starts at a depth of 78 km and continues until 86 km (Figure 24). The fluids generated along the PT path result from the breakdown of amphibole and lawsonite. Overall, with the input criteria in Perple_X, the $H_2O$ phase is released in 19 batches, so the trace element compositions of these 19 fluids are determined for this subduction zone.

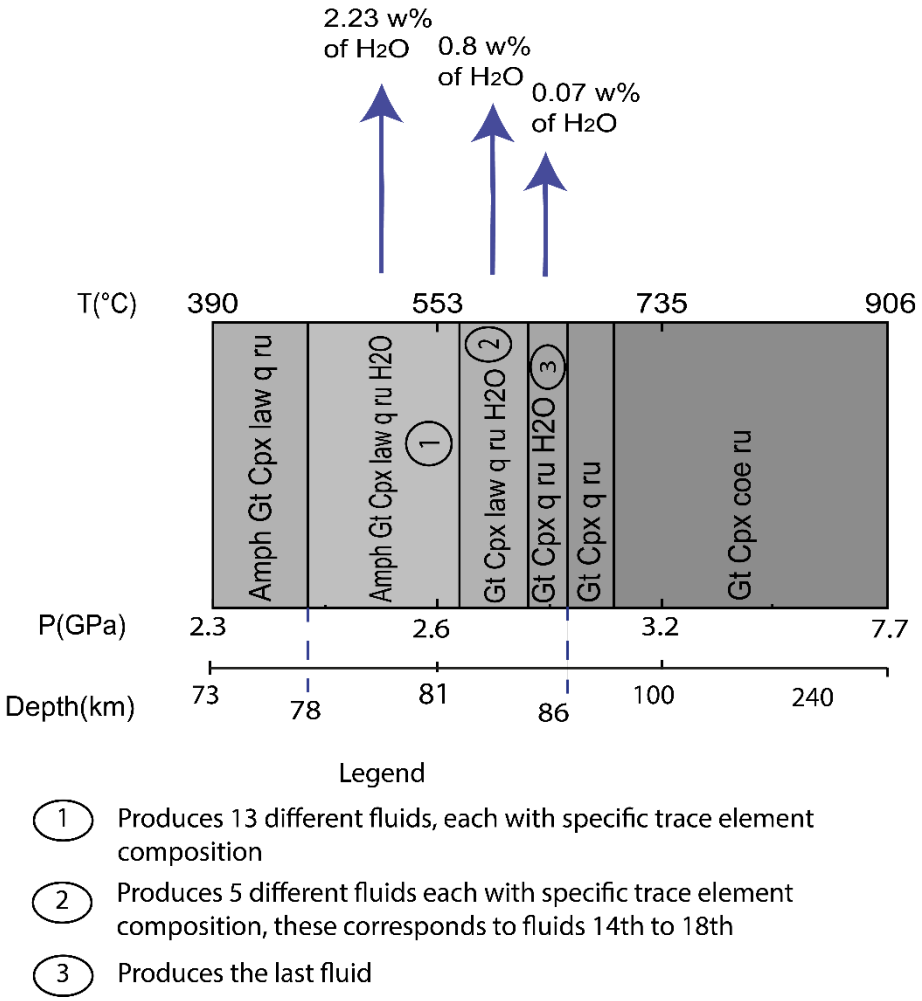


**Figure 24: Mineral assemblage and the quantity of water released by the crust in Northern Mariana, calculated with Perple_X. The water is released as a stable phase nineteen times. T=temperature, P=pressure, Amph=amphibole, Coe=coesite, Cpx=clinopyroxene, Gt=garnet, law=lawsonite, q=quartz and ru=rutile.**

Amphibole and lawsonite start to dehydrate at 489˚C, and the last amphibole breaks down between 594 and 603˚C. So, with the chosen PT path and major element composition in this model, the amphibole is stable at pressures between 2.5 and 2.6 GPa (78 - 83 km depth). Figure 25 shows the trace element composition of four of the batches of fluid, released at increasing temperatures from the amphibole + lawsonite + clinopyroxene + garnet + rutile + quartz assemblage (indicated

with (1) in Figure 24). During the dehydration of these two minerals, the concentration of lithium in the fluid increases by about five orders of magnitude (from $1.38x10^{-5}$ to 4.7 ppm). The concentration of Be increases by four orders of magnitude in the fluid (from $2.92x10^{-4}$ to 0.12 ppm, respectively), while Nb and Ba concentrations increase by two orders (from $1.84x10^{-4}$ to $1.48x10^{-2}$ ppm and $5.4x10^{-2}$ to 6.98 ppm, respectively). Finally, the Lead concentration increases by one order of magnitude, from $1.56x10^{-2}$ to 0.13 ppm. $^{2}$ to 6.98 ppm, respectively). Finally, the Lead concentration increases by one order of magnitude, from $1.56x10^{-2}$ to 0.13 ppm.

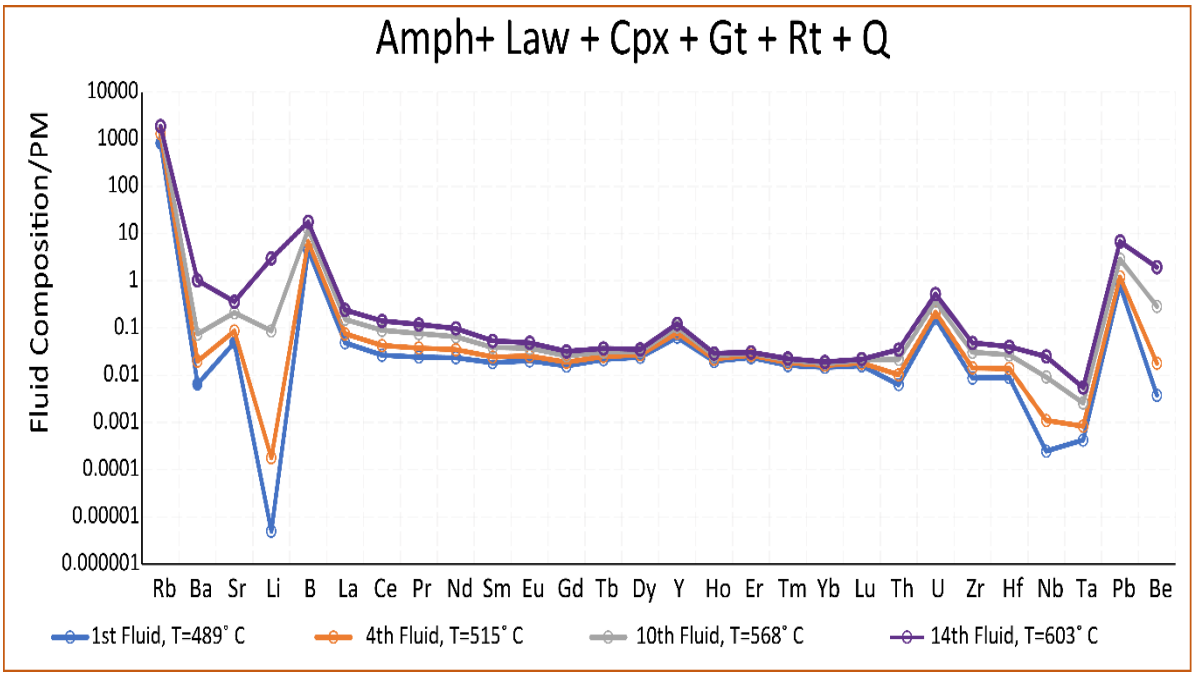


**Figure 25: Fluid composition released from the subducted oceanic crust at Mariana subduction zone. Each fluid results from the dehydration of amphibole and lawsonite and from the interaction with the other minerals from the mineral assemblage, between 489 and 603˚C and depth between 78 and 83 km.**

In general, lawsonite has a larger stability field than amphiboles and is the main crustal water carrier. Lawsonite starts to dehydrate at 489˚C (2.5 GPa), and it is the last mineral to break down before 646˚C and 2.78 GPa. Figure 26 shows the fluid compositions that result from lawsonite dehydration, from lawsonite + clinopyroxene + garnet + rutile + quartz mineral assemblage (indicated with (2) in Figure 24). Comparison between figures 25 and 26 show that exist less variation in the trace element composition of the fluids that result from the lawsonite + clinopyroxene + garnet + rutile + quartz mineral assemblage than the amphibole + lawsonite + clinopyroxene + garnet + rutile + quartz mineral assemblage.

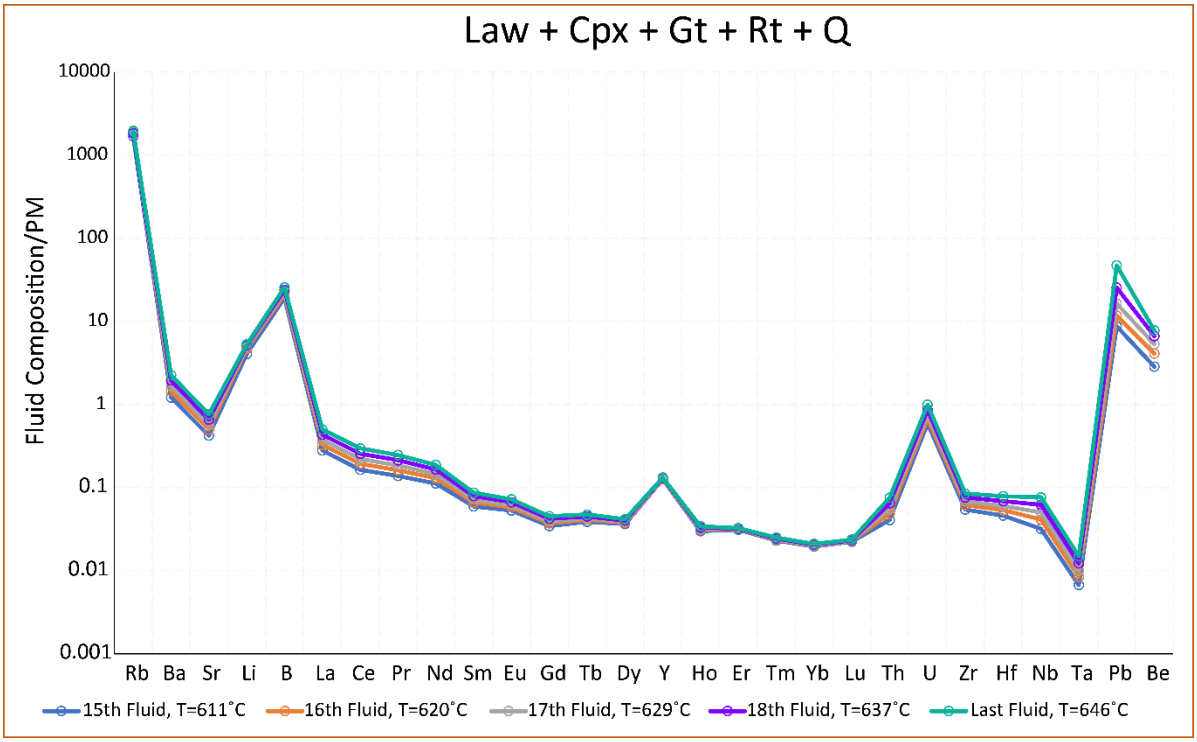


**Figure 26: Fluid composition that results from the dehydration of lawsonite at Mariana subduction zones Each fluid results from the dehydration of lawsonite and from the interaction with the other minerals from the mineral assemblage, from 486˚C and 2.5 GPa until 646˚C and 2.7 GPa.**

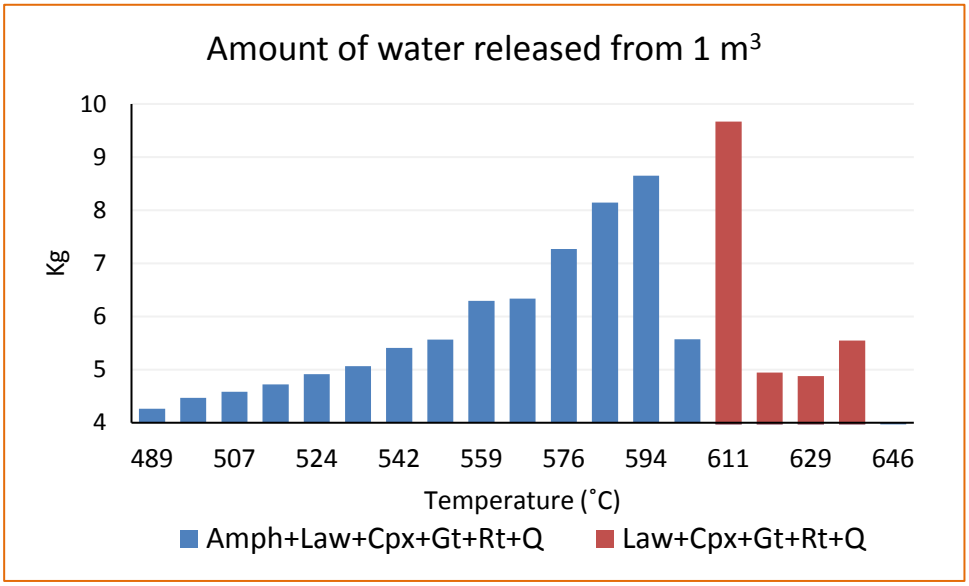


**Figure 27: Amount of water released from 1 m³ of altered oceanic crust at the Mariana subduction zone. Breaking down of the final amphibole occurs at 603˚C.**

The results from this model show that the total amount water released from 1 $m^3$ of the altered subducted oceanic crust is 100.75 kg for the Mariana subduction zone (Figure 27). Total of 8.65 kg are released at 603 C, resulting from the breakdown of the last amphiboles and of lawsonite.

Figure 27 shows also that at 611˚C, the lawsonite releases around 9.66 kg of water. This is due to the big quantity of lawsonite breaking down, i.e.~1.2 wt% of the lawsonite present in the system breaks down.

### *4.3.2 Northern Vanuatu*

Based on Perple_X calculations, the dehydration of North of Vanuatu subduction zone starts at a depth of 79 km and continues until 88 km (Figure 28). The dehydration at this subduction zone happens between 511 and 741˚C and pressures between 2.5 and 2.8 GPa. According to the input criteria in Perple_X, the fluids at this subduction zone will result from breaking down of amphibole, lawsonite and zoisite (Figure 28). Overall, with the input criteria in Perple_X, the $H_2O$ phase is released as a stable phase twenty-four times, so the trace element compositions of these twenty-four fluids are determined for this subduction zone.

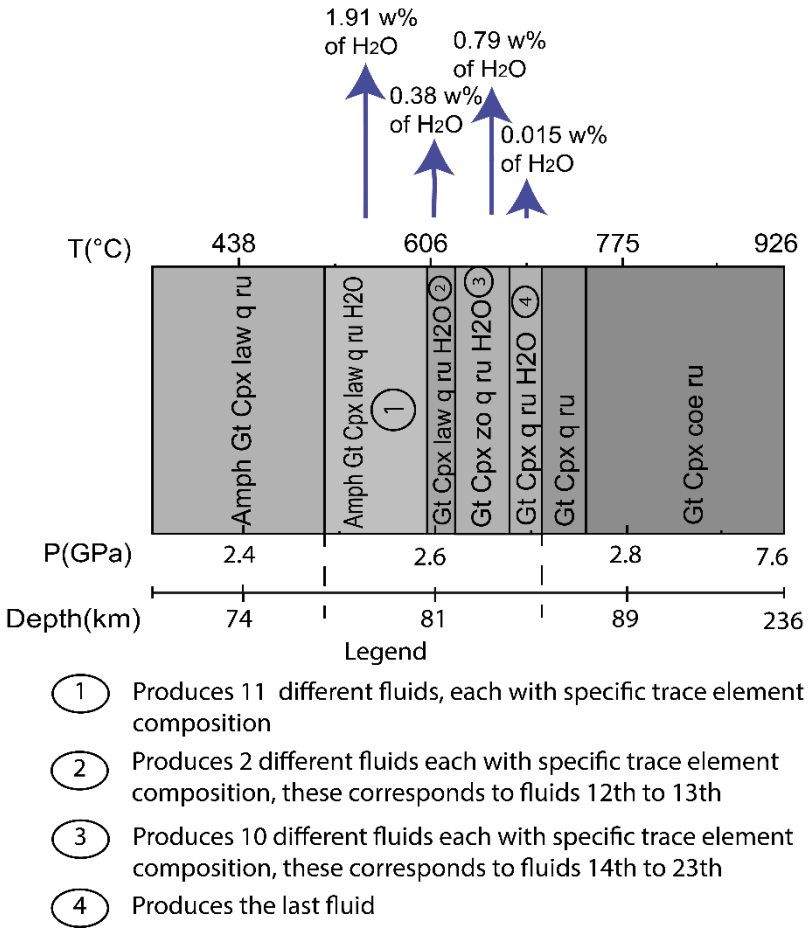


**Figure 28: Mineral assemblage and the quantity of water released for Vanuatu subduction zone, calculated with Perple_X. The water is released as a stable phase twenty-four times. T=temperature, P=pressure, Amph=amphibole, Coe=coesite, Cpx=clinopyroxene, Gt=garnet, law=lawsonite, q=quartz, ru=rutile and Zo=zoisite.**

Amphibole and lawsonite are releasing fluid simultaneously between 511 and 596˚C. The last amphibole breaks down between 596 and 605˚C, around 81 km of depth. Figure 29 shows the evolution of the fluids' trace element concentration released at different temperatures from the amphibole + lawsonite + clinopyroxene + garnet + rutile + quartz assemblage (indicated with (1) in Figure 28). As for the Marianas, during the dehydration of amphibole and lawsonite, the Li concentration in the fluids increases by five orders of magnitude (from $2.41x10^{-5}$ to 5.03 ppm). The fluid concentration of Ba, Nb and Be increases by two orders of magnitude (from $6.35x10^{-2}$ to 4.67, from $2.34x10^{-4}$ to $1.55x10^{-2}$ and $3.69x10^{-4}$ to 0.12 ppm) while the concentration of Ta, Pb increases from $2.3x10^{-5}$ to $2.46x10^{-2}$ and $1.64x10^{-2}$ to 0.13, respectively.

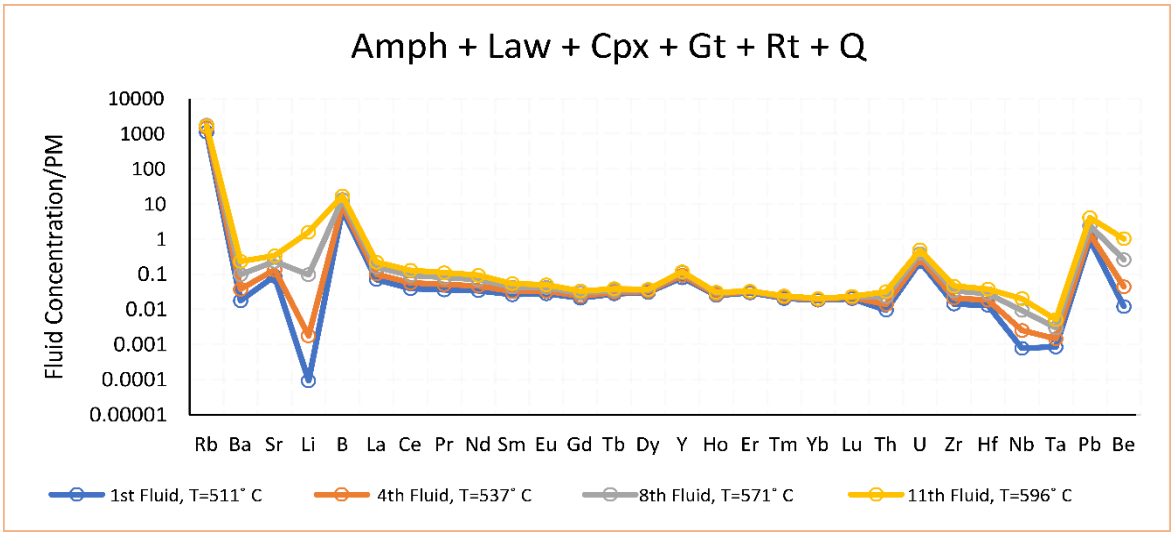


**Figure 30: Fluid composition released from the subducted oceanic crust at the Vanuatu subduction zone. Each fluid results from the dehydration of amphibole and lawsonite and from the interaction with the other minerals from the mineral assemblage, between 511 and 596˚C and depth between 79 and 80 km.**

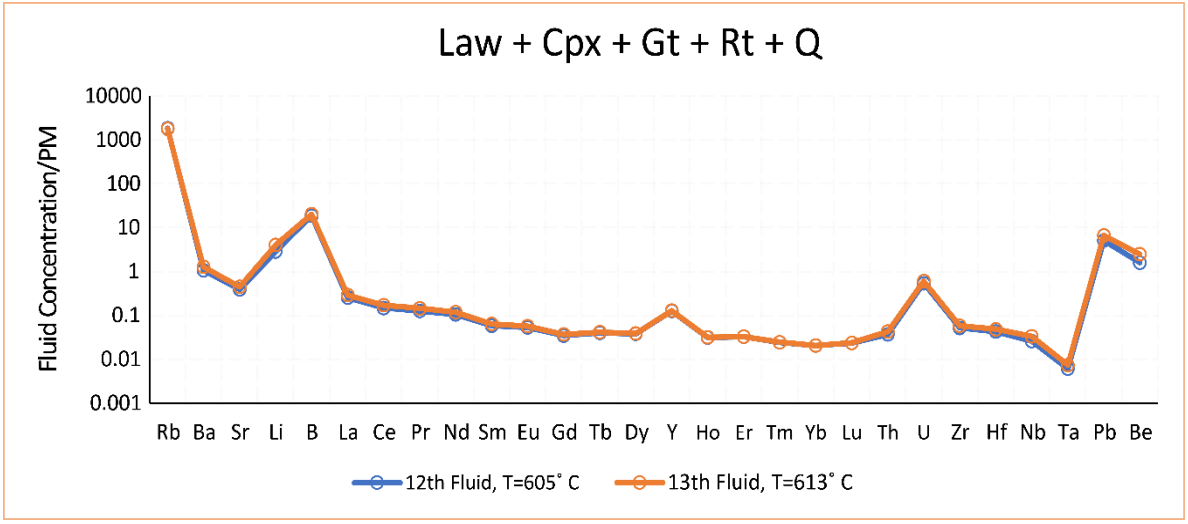


**Figure 29: Fluid composition that results from the dehydration of lawsonite at Vanuatu subduction zone. Each fluid results from the dehydration of lawsonite and from the interaction with the other minerals from the mineral assemblage, between 605 and 613˚C, this correspond to depths between 80 and 81 km.**

When lawsonite is the only hydrous phase in the system, there are only two fluid batches released (Figure 30), resulting from the dehydration process. Lawsonite is the only hydrous phase stable between 605 and 613˚C, around 81 km. Between 613 and 622˚C, lawsonite transforms to zoisite, releasing 0.65 wt% of water.

From 622 to 741˚C, zoisite is the only hydrous phase present in the system (Figure 31). Fluid concentrations of strontium increase by six orders of magnitude (from $4.03x10^{-4}$ to 67.23 ppm) during its breakdown. Furthermore, the Pb fluid concentration increases by two orders of magnitude (from $2.6x10^{-2}$ to 2.56 ppm), while the concentration of Ba increases from 2.53 to 73.6 ppm.

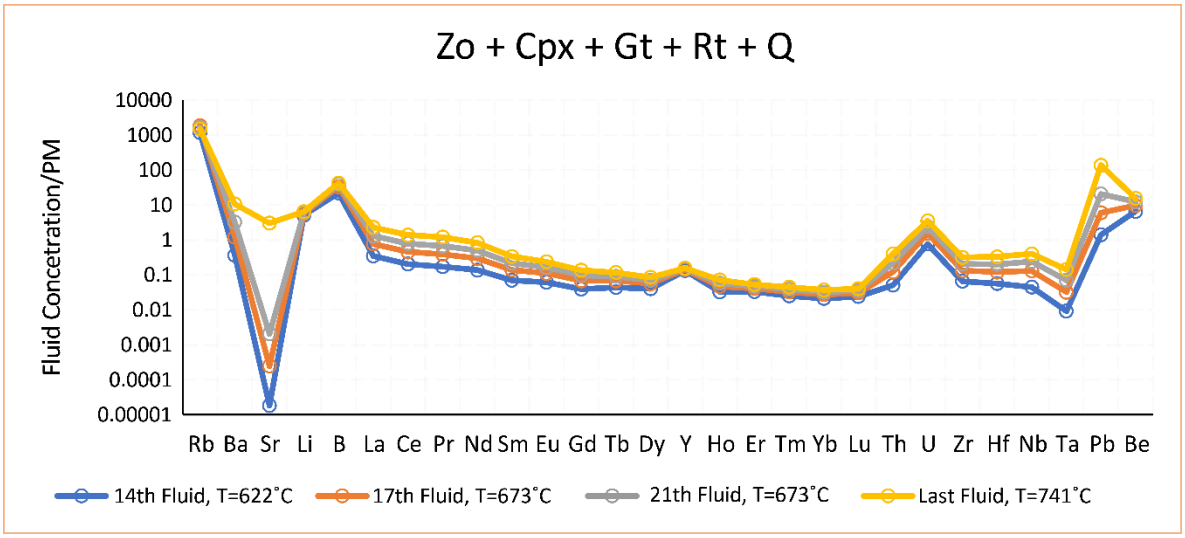


**Figure 31: Fluid composition that results from the dehydration of zoisite at Vanuatu subduction zone. Zoisite is the only hydrous phase between 622 and 741˚C, this correspond to depths between 81 and 88 km. Each fluid results from the dehydration of zoisite and from the interaction with the other minerals from the mineral assemblage.**

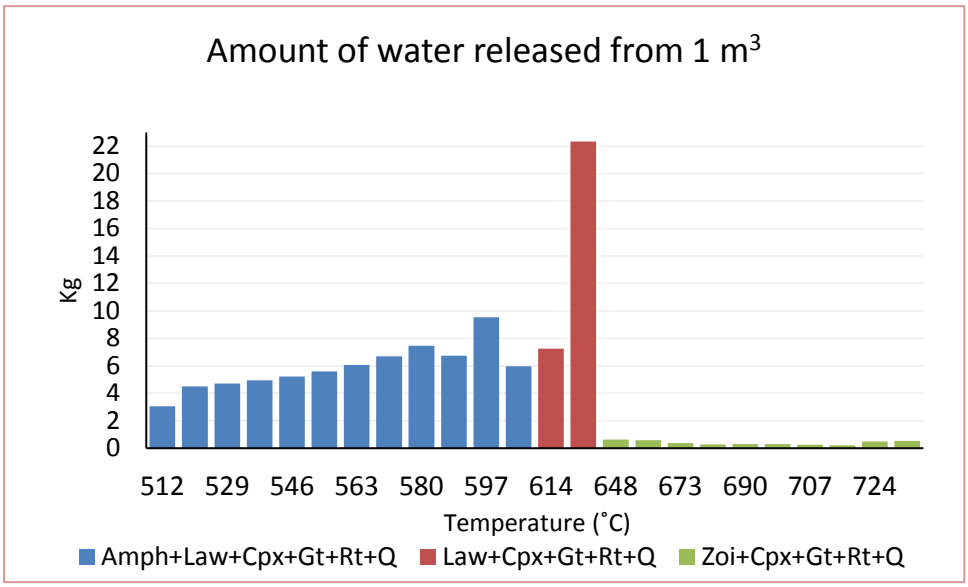


**Figure 32: Amount of water released from 1 $m^3$ of altered oceanic crust at Vanuatu subduction zone. Breaking down of the final amphibole occurs at 605˚C. Lawsonite is the only hydrous phase between 605 and 613˚C. Between 613 and 622˚C, lawsonite transforms to zoisite, releasing 22 kg of water.**

For the Vanuatu subduction zone, the presented model gives a total amount of 103.02 kg released from 1 $m^3$ of altered oceanic crust. Figure 32 shows that, at 622˚C, the amount of water released from the oceanic crust is around 22 kg. The high value is due to the transformation of 7.46 wt% of lawsonite to 5.72 wt% of zoisite. It is important to mention, that after the breakdown of lawsonite, only 3.94 kg of water remains in the oceanic crust inside of zoisite.

### *4.3.3 General Results*

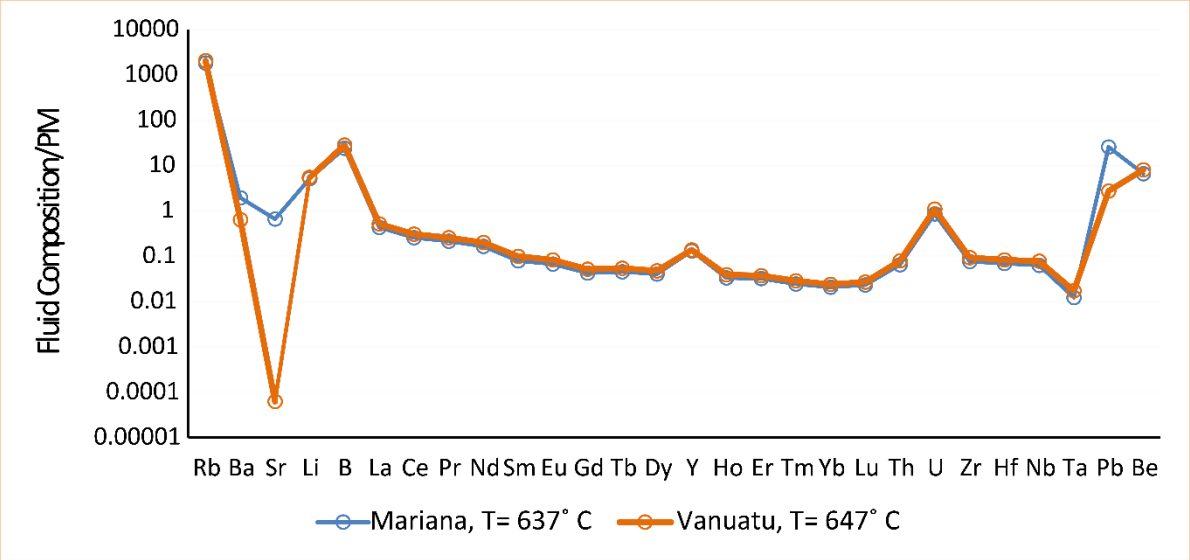


**Figure 33: Fluid composition for similar temperatures but different mineral assemblages. The blue line and dots represents the Marianas data at 637˚C and with mineral assemblage: amphibole + lawsonite + clinopyroxene + garnet + rutile + quartz. The green line and dots represent the Vanuatu subduction zone 647˚C and with the follow mineral assemblage: zoisite + clinopyroxene + garnet + rutile + quartz.**

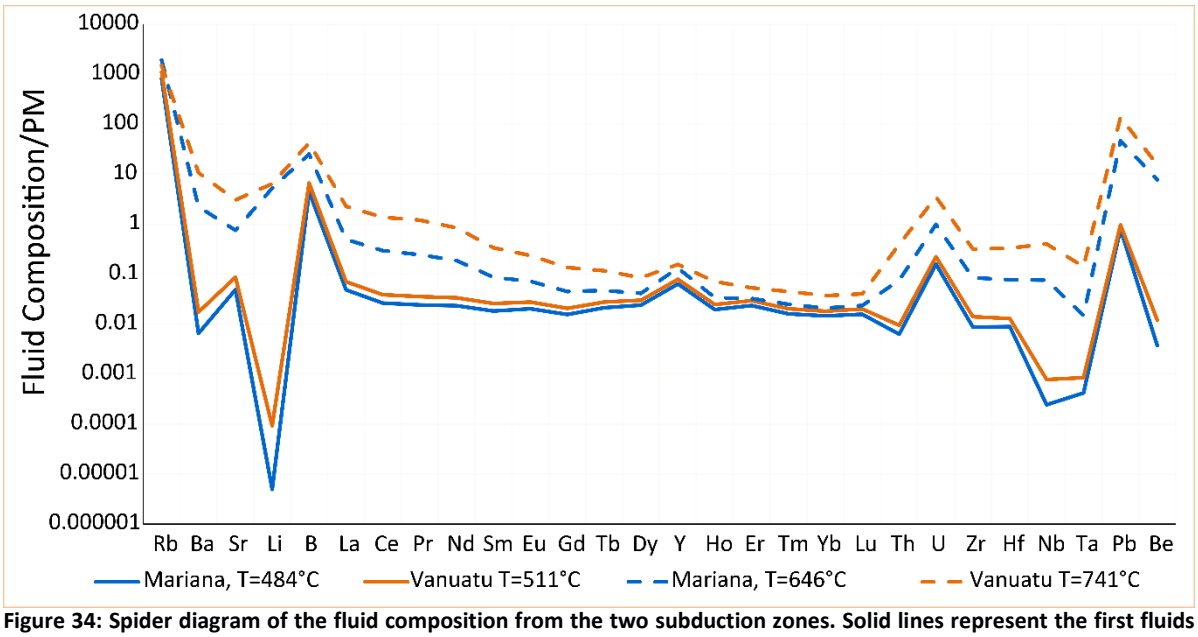


**Figure 34: Spider diagram of the fluid composition from the two subduction zones. Solid lines represent the first fluids released from the dehydration of the hydrous minerals. Dashed lines are representing the fluid that comes from the breakdown of the last hydrous minerals, which, for Mariana, is lawsonite and, for Vanuatu, is zoisite.**

The fluid concentrations of Ba, Sr, B, and Pb differ between Mariana and Vanuatu models for similar temperature conditions (Figure 33). The trace elements with the biggest difference between the fluids from the two examples are Ba, Sr and Pb. The fluids representing the cold subduction zone have more than double the concentration of Ba, ten times more Pb and fifty times more Sr than those that simulate the fluids released from the hot subduction zone.

Figure 34 contains the composition of the first and the last fluids from each subduction zone. It is worth noting that the last fluids are more enriched in trace elements in comparison with the first fluids from the same subduction zone.

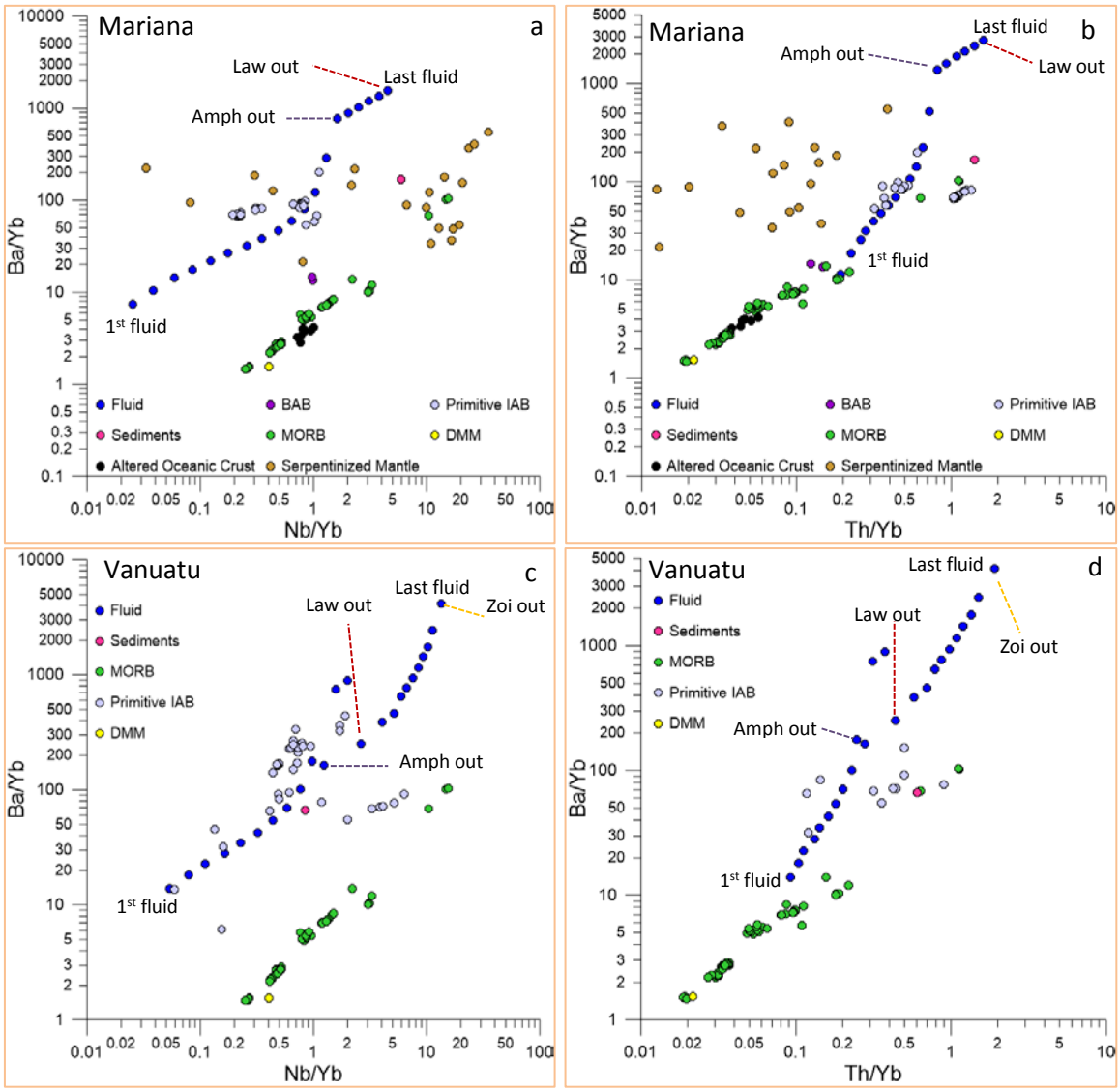


**Figure 35: Geochemical ratios used as proxies to describe total subduction component of North Mariana and North Vanuatu subduction zone. The blue dots represent the fluids composition calculated in my models. Data for the different rocks reservoir are: Altered Oceanic Crust from Kelley et al. (2003) and White & Klein (2013); sediments from Plank & Langmuir (1998); MORB and BAB from Jenner & O'Neill (2012); DMM from Workman & Hart (2005); and Primitive IAB from Turner et al. (1999) and Sorbadere et al. (2011), Sorbadere et al. (2013), Kent & Elliott (2002), and Tamura et al. (2004). Amph= amphibole, Law=lawsonite and Zoi=zoisite.**

In Figure 35, the trace element ratios are shown for data from the major types of rocks and from the fluids calculated in this dissertation, for Mariana (Figure 35 a and b) and Vanuatu (Figure 35 c and d) subduction zones. The black dashes lines represent the moment (i.e. PT condition) when the amphibole disappears from the mineral assemblage, while the red and yellow dashes lines represent the disappearance from the mineral assemblage of lawsonite and zoisite, respectively. Extremely high Ba/Yb and Th/Y ratios can be observed for the last fluids resulting from lawsonite and zoisite dehydration. An overlap between ratios of primitive IAB rocks and some of the fluids is observed for the total subduction components for both subduction zones. More specifically, a similarity of Ba/Yb, Th/Yb and Nb/Yb ratios exists between the primitive IAB and the fluids that result from the amphibole + lawsonite + garnet + clinopyroxene + rutile + quartz mineral assemblage. For the examples demonstrated in Figure 34, there is no similarity of the Ba/Yb, Th/Yb, and Nb/Yb ratios between the fluids calculated in this dissertation and the sediments, MORB, BAB, serpentinized mantle, and altered oceanic crust data.

## 4.4 Discussion

The enrichment of LILE and relative depletion of HFSE in IAB show the influence of the slab-derived fluids in the creation of arc basalts. Elliott (2003) states that slab fluids have little influence on removing the HFSE from the oceanic crust. The fluids modelled in this dissertation have a high proportion of HFSE when normalised with the primitive mantle (Figure 33). This is probably due to the absence of certain accessory minerals, such as apatite and titanite, that would retain a high content of HFSE in their composition. The presented model for the Mariana subduction zone shows that during the dehydration of the oceanic crust, the fluid LREE concentration increases by one order of magnitude and the last fluid contains Ba=15.4 ppm, Li=8.4 ppm, Sr= 16.7 ppm, Nb=0.04 ppm, Pb=0.87 ppm and Be=0.48 ppm. On other hand, in the model that represents the fluids resulting from the dehydration processes at Vanuatu subduction zones, the La, Ce and Nd concentrations in these fluids increase by two orders of magnitude during the total dehydration process (from $4.83x10^{-2}$ to 1.57 ppm, from $6.82x10^{-2}$ to 2.43 ppm and from $4.55x10^{-2}$ to 1.13 ppm, respectively). The last fluid of this model contains Ba= 73.6 ppm, Li=10.39 ppm, Sr= 67.2 ppm, Nb=0.24 ppm, Pb=2.57 ppm and Be=0.96 ppm. In the models of this dissertation, some of the PT windows where transformation and dehydration of hydrous minerals occur are very small (Figure 30). When the PT windows are so small some of the reactions can be incomplete or even occur at high PT conditions due to kinetic limitations.

Two major factors that influence the trace element concentrations in the fluids need discussion: the PT conditions of the subduction zone and the mineral assemblage of the subducting slab, which changes with the PT conditions. The PT conditions influence the fluid composition, and

due to the inverse correlation of the partition coefficients with temperature (Figures 6, 11, 15 and 17), a warmer oceanic crust will produce more enriched fluids at the same depth than a colder one. Moreover, the concentration of the fluids released in the shallow parts of the subduction zone is less enriched in trace elements than the fluids released at greater depths. The mineral assemblage also has an important role in controlling the fluid composition, especially for certain elements. In the presence of zoisite, the trace elements compatible with this mineral, such as Sr and Pb, will be retained in the oceanic crust (Figure 33). This can be observed for the Vanuatu subduction zone, the fluid resulting from the breakdown of lawsonite has 9.9 ppm of Sr, while, after lawsonite transforms to zoisite, the Sr concentration in the fluids drops to $4x10^{-3}$ ppm. Furthermore, the fluids resulting from the zoisite breakdown have $4x10^{-3}$ to $2x10^{-1}$ ppm of Sr, while the fluid resulting from the breakdown of the last zoisite minerals have around 67 ppm. This result clearly shows that when this mineral is present in the mineral assemblage, the fluids will be depleted in Sr.

Zoisite also controls the concentration of Pb in the fluids (Appendix III and IV). Although Pb concentrations do not vary a lot during the whole dehydration process, they drop by one order of magnitude in the fluid when zoisite appears in the mineral assemblage. In contrast, the fluid concentration of Pb increases by one order of magnitude when the last zoisite mineral breaks down.

Barium is another trace element for which fluid concentrations is controlled by the mineral assemblage (Appendix III and IV). In both subduction zone models, Ba concentrations in the fluid increase by a factor 2 immediately after the last amphibole disappears. On the other hand, the fluid concentration of Ba decreases by a factor of three when lawsonite transforms to zoisite and increases by a factor of two when the last zoisite breaks down.

Lithium and thorium concentrations in the fluid are not influenced by the presented mineral assemblage. In the models presented in this dissertation, the concentration of these two elements in the fluids is only influenced by temperature, due to the absence of minerals that contain a high amount of these elements.

Barium is not the only element which has elevated quantities in the fluid. Some of the Rb/Th ratios calculated in the models are four to five orders of magnitude higher than the published IAB data. Xiao et al. (2012) argue that at ultrahigh pressures, metamorphic rocks contain high quantities of Sr, Pb, Rb, Th, REE and U. During prograde metamorphic processes, the newly formed minerals in the altered oceanic crust can remove large amounts of fluid-mobile elements from the fluid. For example, paragonite minerals (Na-mica) from their study accommodate Sr and have one to two orders of magnitude more LILE than chondrites. Phengite (K-mica) is another example, and this mineral has two to three orders of magnitude more Ba and Rb in comparison to chondritic values. The extremely high values of Ba and Rb in the fluids (Figure 35) can be explained by the absence of

phengite and paragonite in the modelled altered oceanic crust mineral assemblage. Those minerals are not present in the models, due to the K-free basalts used as starting composition, which does not allow the formation of K-rich hydrous minerals, such as micas, which are stable at high PT conditions.

During the migration of fluids from the altered subducted oceanic crust to the mantle wedge above, these fluids can be exposed to chemical re-equilibration with minerals from the sediments above the slab. Xiao et al. (2012) observed that paragonite and phengite in metamorphic rocks from sedimentary protoliths could retain a higher amount of Ba, Th, Sr, Pb and Rb in comparison to basaltic protoliths. The fluid compositions modelled in this dissertation do not account for any interaction between these fluids and the sediments adjacent to the slab, and this could be the cause of the values of Rb and Ba in the higher PT modelled fluid compositions, which don't reflect observed values from natural systems. The lack of partition coefficient data about sediment-fluid interaction makes the quantification of these processes impossible in this work.

The results from the Ba/Yb vs. Th/Yb diagrams (Figure 35 b and d) need further discussion. As mentioned in the introduction, a high Th/Nb ratio represents a sediment input into the subduction zone (Pearce et al. 2005; Ribeiro et al. 2013; Elliott 2003). Due to the absence of K-rich minerals in the mineral assemblage, such as micas, which contain large amounts of Th, the only factor that controls the Th concentration in my models is the temperature. In the case of a K-free mineral assemblage-fluid interaction, Figure 35 shows some similarity of Th/Yb ratios between the primitive IAB rocks and the same ratio determined for the fluids in my models. A possible explanation for this similarity is that the low Th/Yb ratios of the arc basalts result from the subducted altered basaltic crust and the high Th/Yb ratio from the sediment component. However, more studies are necessary to understand the influence of sediments and basaltic crust on the Th fluid composition and Th behaviour between K-rich mineral assemblages and aqueous fluids.

High Ba/Yb and Ba/Nb values represent the shallow component of the basaltic oceanic crust in the subduction zone (Pearce et al. 2005; Pearce & Stern 2006; Ribeiro et al. 2013). The Ba/Yb vs. Nb/Yb and Ba/Yb vs. Th/Yb diagrams (Figure 35) show that the ratios from the primitive IAB are similar to those of the fluids calculated in my models. These results indicate that the fluids calculated in the models possibly have a similar composition to the fluids involved in the formation of the primitive IAB rocks used as a natural example.

Figures 27 and 32 show that in the presented models, the last fluids released from the altered oceanic crust of the slab, form a very small proportion of the total flux. Figure 34 shows that the same last fluids contain a higher concentration of trace elements in comparison with the fluids released in the first stages in the models. Furthermore, Figure 35 shows a certain similarity between trace element ration from primitive IAB rocks and those of the fluids calculated in this dissertation. These

similarities are, in general, between the fluids released in the beginning and in the middle stages of the models and never between the most enriched fluid and the primitive IAB rocks. Considering all said above, the possible interaction between the mantle wedge above the subducted slab and the fluids released from the slab could be modelled using two types of fluid-rock interaction. For Mariana subduction zone, due to the larger amount of fluids released from each batch, probably the fluids pressure will increase and will create instant channels through which the fluids will migrate to the zone of the mantle wedge where melts are created. In consequence, these fluids will not interact with metasomatized mantle wedge. For the Vanuatu subduction zone, the fluids released from amphibole + lawsonite + clinopyroxene + garnet + rutile + quartz mineral assemblage and probably from lawsonite + clinopyroxene + garnet + rutile + quartz mineral assemblage will be also transported by a focused flow. While the fluids that result from zoisite+ clinopyroxene + garnet + rutile + quartz mineral assemblage will be transported by porous flow to the overlying sediment layer and/or to the mantle wedge. Although these fluids are heavily enriched in trace elements, the amount of fluids released is extremely low, and thus they do not have the capacity to induce big chemical changes on the sediment layer above the subduction zone. Therefore, the fluids will be incorporated to the existent hydrous minerals or will mix with the fluids released from the sediments and migrate to the mantle wedge immediately above the slab and metasomatize it, i. e. the fluid will stay in the mantle wedge as hydrous minerals such as amphiboles and serpentinite. Afterwards, the serpentinized mantle is dragged down along with the slab and, when reaching certain PT condition, the hydrous minerals will break down and create fluids with trace element composition in equilibrium with the altered mantle wedge.

## 4.5 Conclusions

This chapter shows possible trace elements fluid compositions resulting from the dehydration of K-free altered oceanic crust for two natural examples. Mariana and Vanuatu fluid compositions were determined by integrating the temperature-dependent partition coefficients, calculated in Chapter 3, using the Rayleigh distillation Equation 4.2.

In the Vanuatu subduction zone, the subducted oceanic crust is warmer, and so at the same depth, the fluid released in this subduction zone will mostly be richer in trace elements than the fluids released at the Marianas due to the lower *Di* values at higher temperatures. Moreover, this also results in a fluid richer in trace elements deeper in the subduction zone than in the shallower parts.

Trace element concentrations in the fluids also depend on the mineral assemblage from which these fluids result. A good example of this is the existence of epidote in the altered oceanic crust. Strontium and lead are highly compatible with zoisite, so when this mineral is present, the fluid created from the subducted oceanic crust is depleted in these elements. barium is compatible with

amphibole and zoisite. Fluids resulting from the dehydration of those minerals or even fluids that approach an equilibrium state with them will have a low concentration of barium. The concentration of thorium and lithium in the fluids, in my models, do not show any variation with changes in the mineral assemblage and depend only on temperature variations. A possible explanation for this is the absence of minerals which are significant hosts of these elements, such as phengite and paragonite.

A similarity exists between the trace element ratios used as fluid proxies (Ba/Yb and Th/Yb) from the fluids modelled in this dissertation and the same ratios from natural examples of primitive IAB rocks. A possible conclusion from this result is that fluids involved in the generation of primitive arc basalts could have a similar composition as the fluids modelled in this dissertation.

The results from this chapter show that integrating a temperature-dependent partition coefficient in the Rayleigh distillation equation is a good method to calculate the evolution of the fluids composition with increasing temperature. The applications of this method are still limited due to the uncertainty and absence of partition coefficients data between several important groups of minerals and fluid. Other limitations are the lack of data on the influence of oxygen fugacity, pressure, and pH over the partition coefficients. Despite these limitations, this method can be used to quantify rock-fluid interaction during metamorphic processes in any tectonic environment. The problems related to the paucity of data on the actual composition of slab fluids, their influence on the alteration of the mantle wedge above the slab, and their influence on the formation/interaction with the IAB magmas can be constrained with detailed laboratory study of mineral-fluid interactions to determine partition coefficients more accurately. Moreover, establishing temperature-dependent regressions for the calculation of partition coefficients for K-bearing minerals will allow a better understanding of trace element exchanges between the subducted oceanic crust/sediments and aqueous fluids. Furthermore, this method can be applied to study the trace element distributions of mineral and ore deposits, such as hydrothermal systems and the depositional environment of skarn and pegmatites.

# 5. General conclusion and future work

In this dissertation, temperature-dependent regressions were developed, for the first time, in order to predict the trace element behaviour between six key minerals involved in slab crust devolatilization and aqueous fluids using their partition coefficients. Furthermore, those partition coefficients were used to calculate the fluid compositions resulting from the dehydration of subducting K-free basaltic oceanic crust. The PT conditions of Mariana and Vanuatu subduction zones were used to simulate the fluid composition of a cold and a hot natural subduction example, respectively.

Using temperature-dependent partition coefficients instead of fixed values helps to better understand the trace element behaviour during rock-fluid interactions in metamorphic processes. Overall, for the studied minerals in this dissertation, the compatibility of the trace elements with the fluid increases with temperature. The only exception is in the presence of zoisite: if this mineral is present in the system, higher temperatures make the trace elements more compatible with this mineral.

In this dissertation, for both subduction models, the fluids released in the last stages of dehydration are more enriched in trace elements than the fluids released from the breakdown of the first hydrous minerals. In addition, during the dehydration of the K-free basaltic slab, a small variation of the fluid trace element composition can be observed due to changes in the mineral assemblage. By recognising that trace elements have different compatibilities with different minerals, it becomes evident that the largest variations of trace elements fluid concentrations occur when a mineral phase appears or breaks down. Furthermore, comparison of the Ba/Yb and Th/Yb ratios between the fluids from the models and primitive IAB data show that the fluids involved in the generation of these primitive IAB rocks have a similar composition as the modelled fluids.

Despite the promising results described in Chapter 4, the models developed in this dissertation are still in a preliminary stage. The partition coefficients between K-bearing minerals and fluids are essential to constrain better the fluid composition resulting from dehydration of the oceanic slab. New partition coefficients data can easily be integrated into the models to better constrain the temperature-dependent regressions shown in Chapter 3. Furthermore, once the influence of pressure and other external factors on the partition coefficients are better understood, multiple regression analyses can be used, for the cases where Di behaviour is systematic with the T, to quantify the influence of each factor to determine an accurate composition of the slab fluids.

Temperature-dependent partition coefficients can be used to quantify rock-fluid interactions in metamorphic processes at any tectonic environment. Furthermore, it can be used to predict the trace element behaviour and distribution in ore deposits.

A possible next step of this work could be the calculation of the composition of early Earth subduction zone fluids. Using the methodology described in section 4.2, and using a primitive Earth oceanic crust composition and tectonic PT conditions, will allow the modelling of not only fluid composition released from the slab but also the compositional evolution of the mantle wedge above the slab through time.

## 6. Bibliography


Adam, J. & Green, T., 2006. Trace element partitioning between mica- and amphibole-bearing garnet lherzolite and hydrous basanitic melt: 1. Experimental results and the investigation of controls on partitioning behaviour. *Contributions to Mineralogy and Petrology*, 152(1), pp.1–17.

Adam, J., Green, T.H., Sie, S.H. & Ryan, C.G., 1997. Trace element partitioning between aqueous fluids, silicate melts and minerals.pdf. *European Journal of Mineralogy*, 9, pp.569–584.

Ague, J.J., 2014. Fluid Flow in the Deep Crust. In *Treatise on Geochemistry: Second Edition*. Elsevier Ltd., pp. 203–247. Available at: http://dx.doi.org/10.1016/B978-0-08-095975-7.00306-5.

Akaogi, M. & Akimoto, S., 1977. Pyroxene-Garnet solid-solution equilibria in the systems Mg4Si4O12-Mg3Al2Si3O12 and Fe4Si4O12-Fe3Al2Si3O12 at high pressure and temperatures. *Physics of the Earth and Planetary Interiors*, 15, pp.90–106.

Ayers, J., 1998. Trace element modeling of aqueous fluid - peridotite interaction in the mantle wedge of subduction zones. *Contributions to Mineralogy and Petrology*, 132(4), pp.390–404.

Ayers, J.C., Dittmer, S.K. & Layne, G.D., 1997. Partitioning of elements between peridotite and H2O at 2.0-3.0 GPa and 900-1100°C, and application to models of subduction zone processes. *Earth and Planetary Science Letters*, 150, pp.381–398.

Baillard, C., Crawford, W.C., Ballu, V., Régnier, M., Pelletier, B. & Garaebiti, E., 2015. Seismicity and shallow slab geometry in the central Vanuatu subduction zone. *Journal of Geophysical Research B: Solid Earth*, 120(8), pp.5606–5623.

Banks, D.A., Yardley, B.W.D., Campbell, A.R. & Jarvis, K.E., 1994. REE composition of an aqueous magmatic fluid: A fluid inclusion study from the Capitan Pluton, New Mexico, U.S.A. *Chemical Geology*, 113(3–4), pp.259–272.

Bau, M., 1996. Controls on the fractionation of isovalent trace elements in magmatic and aqueous systems: evidence from Y/Ho, Zr/Hf, and lanthanide tetrad effect. *Contrib Mineral Petrol*, 123, pp.323–333.

Beaumais, A., Bertrand, H., Chazot, G., Dosso, L. & Robin, C., 2016. Temporal magma source changes at Gaua volcano, Vanuatu island arc. *Journal of Volcanology and Geothermal Research*, 322, pp.30–47. Available at: http://dx.doi.org/10.1016/j.jvolgeores.2016.02.026.

Bebout, G.E., 1991. Field-based evidence for devolatilization in subduction zones: implications for arc

magmatism. *Science*, 251(4992), pp.413–416. Available at: http://www.sciencemag.org/content/251/4992/413.short.

Belousova, E.A., Griffin, W.L., O'Reilly, S.Y. & Fisher, N.I., 2002. Apatite as an indicator mineral for mineral exploration: Trace-element compositions and their relationship to host rock type. *Journal of Geochemical Exploration*, 76(1), pp.45–69.

Berthelot, M., 1872. Sur les qui Président au Partage D'un Corps entre Deux Dissolvants (Théorie). *Ann. Chim. Phys.*, 4th Ser 26, pp.408–417.

Bloch, W., Kummerow, J., Salazar, P., Wigger, P. & Shapiro, S.A., 2014. High-resolution image of the North Chilean subduction zone: Seismicity, reflectivity and fluids. *Geophysical Journal International*, 197(3), pp.1744–1749.

Blundy, J. & Wood, B., 1994. Prediction of crystal-melt partition coefficients from elastic moduli. *Nature*, 372(6505), pp.452–454.

Boettcher, A.L., 1970. The System CaO-Al2O3-SiO2-H2O at High Pressures and Temperatures. *J. Petrol.*, 11(69), pp.337–379.

Bouilhol, P., Magni, V., van Hunen, J. & Kaislaniemi, L., 2015. A numerical approach to melting in warm subduction zones. *Earth and Planetary Science Letters*, 411, pp.37–44. Available at: http://linkinghub.elsevier.com/retrieve/pii/S0012821X14007432.

Brady, L., 1953. Chemical nature of silica carried by Steam. *Adsorption Journal Of The International Adsorption Society*, 57(6), pp.706–710.

Breeding, C.M. & Ague, J.J., 2002. Slab-derived fluids and quartz-vein formation in an accretionary prism, Otago Schist, New Zealand. *Geology*, 30(6), pp.499–502.

Brenan, J.M., Ryerson, F.J. & Shaw, H.F., 1998. The role of aqueous fluids in the slab-to-mantle transfer of boron, beryllium, and lithium during subduction: Experiments and models. *Geochimica et Cosmochimica Acta*, 62(19–20), pp.3337–3347.

Brenan, J.M., Shaw, H.F., Phinney, D.L. & Ryerson, F.J., 1994. Rutile-aqueous fluid partitioning of Nb, Ta, Hf, Zr, U and Th: implications for high field strength element depletions in island-arc basalts. *Earth and Planetary Science Letters*, 128(3–4), pp.327–339.

Brenan, J.M., Shaw, H.F., Ryerson, F.J. & Phinney, D.L., 1995. Mineral-aqueous fluid partitioning of trace elements at 900°C and 2.0 GPa: Constraints on the trace element chemistry of mantle and

deep crustal fluids. *Geochimica et Cosmochimica Acta*, 59(16), pp.3331–3350.

Brenan, J.M. & Watson, E.B., 1991. Partitioning of trace elements between olivine and aqueous fluids at high P-T conditions: implications for the effect of fluid composition on trace-element transport. *Earth and Planetary Science Letters*, 107(3–4), pp.672–688.

Brice, J.C., 1975. Some thermodynamic aspects of the growth of strained crystals. *Journal of Crystal Growth*, 28(2), pp.249–253. Available at: http://linkinghub.elsevier.com/retrieve/pii/0022024875902419.

Brunsmann, A., Franz, G. & Erzinger, J., 2001. REE mobilization during small-scale high-pressure fluid-rock interaction and zoisite/fluid partitioning of La to Eu. *Geochimica et Cosmochimica Acta*, 65(4), pp.559–570.

Caciagli, N., Brenan, J.M., McDonough, W.F. & Phinney, D., 2011. Mineral-fluid partitioning of lithium and implications for slab-mantle interaction. *Chemical Geology*, 280(3–4), pp.384–398.

Cao, Y., Song, S., Su, L., Jung, H. & Niu, Y., 2016. Highly refractory peridotites in Songshugou, Qinling orogen: Insights into partial melting and melt/fluid-rock reactions in forearc mantle. *Lithos*, 252–253, pp.234–254.

Carswell, D. a. & Cuthbert, S.J., 1986. Eclogite facies metamorphism in the lower continental crust. *Geological Society, London, Special Publications*, 24(1), pp.193–209. Available at: http://sp.lyellcollection.org/cgi/doi/10.1144/GSL.SP.1986.024.01.18.

Connolly, J.A.D., 2005. Computation of phase equilibria by linear programming: A tool for geodynamic modeling and its application to subduction zone decarbonation. *Earth and Planetary Science Letters*, 236(1–2), pp.524–541. Available at: http://linkinghub.elsevier.com/retrieve/pii/S0012821X05002839.

Connolly, J.A.D., 2010. The mechanics of metamorphic fluid expulsion. *Elements*, 6(3), pp.165–172.

Connolly, J.A.D. & Podladchikov, Y.Y., 2014. An analytical solution for solitary porosity waves: Dynamic permeability and fluidization of nonlinear viscous and viscoplastic rock. *Geofluids*, 15(1–2), pp.269–292.

Cullers, R.L., Medaris, L.G. & Haskin, L.A., 1973. Experimental studies of the distribution of rare earths as trace elements among silicate minerals and liquids and water. *Geochim. Cosmochim. Acta*, 37, pp.1499–1512.

Davidson, J., Turner, S., Handley, H., Macpherson, C. & Dosseto, A., 2007. Amphibole “sponge” in arc crust? *Geology*, 35(9), pp.787–790.

Deer, W.A., Howie, R.A. & Zussman, J., 1992. *An Introduction to the Rock-Forming Minerals* 3rd ed., Addison Wesley Longman Limited, London.

Edwards, C., Menzies, M. & Thirlwall, M., 1991. Evidence from muriah, indonesia, for the interplay of supra-subduction zone and intraplate processes in the genesis of potassic alkaline magmas. *Journal of Petrology*, 32(3), pp.555–592.

Elliott, T., 2003. Tracers of the slab. *Inside the Subduction Factory*, 138, pp.23–45. Available at: http://dx.doi.org/10.1029/138GM03.

Elliott, T., Plank, T., Zindler, A., White, W. & Bourdon, B., 1997. arc Guguan have and Agrigan have the least negative systematics. *Most*, 102.

Ellis, D.J. & Thompson, A.B., 1986. Subsolidus and partial melting reactions in the quartz-excess CaO + MgO + Al2O3 + SiO2 + H2O system under water excess and water-deficient conditions to 10 kbar: some implications for the origin of peraluminous melts from mafic rocks. *Journal of Petrology*, 27, pp.91–121.

Engvik, A.K., Austrheim, H. & Erambert, M., 2001. Interaction between fluid flow, fracturing and mineral growth during eclogitization, and example from the Sunnfjord area, Western Gneiss Region, Norway. *Lithos*, 57, pp.111–141.

Fabbrizio, A., Stalder, R., Hametner, K., Günther, D. & Marquardt, K., 2013. Experimental partitioning of halogens and other trace elements between olivine, pyroxenes, amphibole and aqueous fluid at 2 GPa and 900-1,300°C. *Contributions to Mineralogy and Petrology*, 166(2), pp.639–653.

Feineman, M.D., Ryerson, F.J., DePaolo, D.J. & Plank, T., 2007. Zoisite-aqueous fluid trace element partitioning with implications for subduction zone fluid composition. *Chemical Geology*, 239(3–4), pp.250–265.

Frost, R.B. & Beard, J.S., 2007. On silica activity and serpentinization. *Journal of Petrology*, 48(7), pp.1351–1368.

Garrido, C.J., Bodinier, J.L. & Alard, O., 2000. Incompatible trace element partitioning and residence in anhydrous spinel peridotites and websterites from the Ronda orogenic peridotite. *Earth and Planetary Science Letters*, 181(3), pp.341–358.

Green, T.H. & Adam, J., 2003. Experimentally-determined trace element characteristics of aqueous fluid from partially dehydrated mafic oceanic crust at 3.0 GPa, 650-700°C. *European Journal of Mineralogy*, 15(5), pp.815–830.

Green, T.H., Blundy, J.D., Adam, J. & Yaxley, G.M., 2000. SIMS determination of trace element partition coefficients between garnet, clinopyroxene and hydrous basaltic liquids at 2-7.5 GPa and 1080-1200°C. *Lithos*, 53, pp.165–187.

Grove, T., Chatterke, N., Parman, S. & Medard, E., 2006. The influence of H2O on mantle wedge melting. *Earth and Planetary Science Letters*, 249(1–2), pp.74–89. Available at: http://linkinghub.elsevier.com/retrieve/pii/S0012821X06004869.

Hacker, B.R., 2008. H2O subduction beyond arcs. *Geochemistry Geophysics Geosystems*, 9, p.24.

Hawkesworth, C.J., Gallagher, K., Hergt, J.M. & McDermott, F., 1993. Mantle and Slab Contributions in Arc Magmas. *Annual Review of Earth and Planetary Sciences*, 21, pp.175–204.

Hermann, J., 2002. Allanite: thorium and light rare earth element carrier in subducted crust. *Chemical Geology*, 192(3), pp.289–306.

Hermann, J. & Green, D.H., 2001. Experimental constraints on high pressure melting in subducted crust. *Earth and Planetary Science Letters*, 188(1–2), pp.149–168. Available at: http://linkinghub.elsevier.com/retrieve/pii/S0012821X01003211%5Cnpapers2://publication/doi/10.1016/S0012-821X(01)00321-1.

Hermann, J., Spandler, C., Hack, A. & Korsakov, A. V., 2006. Aqueous fluids and hydrous melts in high-pressure and ultra-high pressure rocks: Implications for element transfer in subduction zones. *Lithos*, 92(3–4), pp.399–417.

Hollister, L.S., 1966. Garnet Zoning : An Interpretation Based on the Rayleigh Fractionation Model. *Science (New York, N.Y.)*, 154(3757), pp.1647–1651.

van Huene, R. & Scholl, D.W., 1991. AT CONVERGENT MARGINS CONCERNING SEDIMENT SUBDUCTION , EROSION , AND THE GROWTH CRUST and truncation caused by. *Reviews of Geophysics*, 29(3), pp.279–316.

Ikemoto, A. & Iwamori, H., 2014. Numerical modeling of trace element transportation in subduction zones: implications for geofluid processes. *Earth, Planets and Space*, 66(1), p.26. Available at: http://www.earth-planets-space.com/content/66/1/26.

Inoue, T., Irifune, T., Yurimoto, H. & Miyagi, I., 1998. Decomposition of K-amphibole at high pressures and implications for subduction zone volcanism. *Physics of the Earth and Planetary Interiors*, 107(1–3), pp.221–231.

Ionov, D.A. & Hofmann, A.W., 1995. Nb-Ta-Rich Mantle Amphiboles and Micas - Implications for Subduction-Related Metasomatic Trace-Element Fractionations. *Earth and Planetary Science Letters*, 131(3–4), pp.341–356. Available at: g:%5CREF%5CPAPERS%5C2818.pdf.

Iwamori, H., 2004. Phase relations of peridotites under H2O-saturated conditions and ability of subducting plates for transportation of H2O. *Earth and Planetary Science Letters*, 227, pp.57–71.

Iwamori, H., 1998. Transportation of H2O and melting in subduction zones. *Earth and Planetary Science Letters*, 160(1–2), pp.65–80.

Jenkins, D.M., Newton, R.C. & Goldsmith, J.R., 1985. Relative Stability of Fe-Free Zoisite and Clinozoisite. *The Journal of Geology*, 93(6), pp.663–672.

Jenner, F.E. & O'Neill, H.S.C., 2012. Analysis of 60 elements in 616 ocean floor basaltic glasses. *Geochemistry, Geophysics, Geosystems*, 13(1), pp.1–11.

Jenner, G.A., Foley, S.F., Jackson, S.E., Green, T.H., Fryer, B.J. & Longerich, H.P., 1993. Determination of partition coefficients for trace elements in high pressure-temperature experimental run products by laser ablation microprobe-inductively coupled plasma-mass spectrometry (LAM-ICP-MS). *Geochimica et Cosmochimica Acta*, 57(23–24), pp.5099–5103.

Kato, T., 2003. Geodetic evidence of back-arc spreading in the Mariana Trough. *Geophysical Research Letters*, 30(12), p.1625. Available at: http://doi.wiley.com/10.1029/2002GL016757.

Kelley, K.A., Plank, T., Ludden, J. & Staudigel, H., 2003. Composition of altered oceanic crust at ODP Sites 801 and 1149. *Geochemistry, Geophysics, Geosystems*, 4(6).

Kessel, R., Schmidt, M.W., Ulmer, P. & Pettke, T., 2005. Trace element signature of subduction-zone fluids, melts and supercritical liquids at 120-180 km depth. *Nature*, 437(7059), pp.724–727.

Kimura, J.I. & Yoshida, T., 2006. Contributions of slab fluid, mantle wedge and crust to the origin of quaternary lavas in the NE Japan arc. *Journal of Petrology*, 47(11), pp.2185–2232.

Kogiso, T., Tatsumi, Y. & Nakano, S., 1997. Trace element transport during dehydration processes in the subducted oceanic crust: 1. Experiments and implications for the origin of ocean island

basalts. , 148, pp.193–205.

El Korh, A., Schmidt, S.T., Ulianov, A. & Potel, S., 2009. Trace element partitioning in HP-LT metamorphic assemblages during subduction-related metamorphism, Ile de Groix, France: A detailed LA-ICPMS study. *Journal of Petrology*, 50(6), pp.1107–1148.

Kushiro, I. & Yoder, H.S.J., 1966. Anorthite-Forsterite and Anorthite-Enstatite Reactions and their bearing on the Basalt-Eclogite Transformation. *Journal of Petrology*, 7(3), pp.337–62.

Laudise, R.A. & Ballman, A.A., 1961. The Solubility of Quartz Under Hydrothermal Conditions. , 65(7), pp.1396–1400.

Lesnov, F.P., 2010. *Rare Earth Elements in Ultramafic and Mafic Rocks and their Minerals* G. V. Polyakov & G. N. Anashin, eds., CRC Press.

Lin, P.-N., Stern, R.J. & Bloomer, S.H., 1989. Shoshonitic volcanism in the Northern Mariana Arc: 2. Large-ion lithophile and rare earth element abundances: Evidence for the source of incompatible element enrichments in intraoceanic arcs. *Journal of Geophysical Research*, 94, p.4497.

Macgregor, I.D., 1970. The effect of CaO, Cr2O3, Fe2O3 and Al2O3 on the stability of spinel and garnet peridotites. *Physics of the Earth and Planetary Interiors*, 3(C), pp.372–377.

Magni, V., Bouilhol, P. & van Hunen, J., 2014. Deep water recycling through time. *AGU Publications*, pp.4203–4216.

Manning, C.E., 2004. The chemistry of subduction-zone fluids. *Earth and Planetary Science Letters*, 223(1–2), pp.1–16. Available at: http://linkinghub.elsevier.com/retrieve/pii/S0012821X0400278X.

Marschall, H.R., Altherr, R., Ludwig, T., Kalt, A., Gméling, K. & Kasztovszky, Z., 2006. Partitioning and budget of Li, Be and B in high-pressure metamorphic rocks. *Geochimica et Cosmochimica Acta*, 70(18), pp.4750–4769.

Marschall, H.R., Altherr, R. & Rupke, L., 2007. Squeezing out the slab - modelling the release of Li, Be and B during progressive high-pressure metamorphism. *Chemical Geology*, 239(3–4), pp.323–335.

Martin, L.A.J., Wood, B.J., Turner, S. & Rushmer, T., 2011. Experimental measurements of trace element partitioning between lawsonite, zoisite and fluid and their implication for the

composition of arc magmas. *Journal of Petrology*, 52(6), pp.1049–1075.

McIntire, W.L., 1963. Trace element partition coefficients—a review of theory and applications to geology. *Geochimica et Cosmochimica Acta*, 27(12), pp.1209–1264.

Mibe, K., Kanzaki, M., Kawamoto, T., Matsukage, K.N., Fei, Y. & Ono, S., 2004. Determination of the second critical end point in silicate-H2O systems using high-pressure and high-temperature X-ray radiography. *Geochimica et Cosmochimica Acta*, 68(24), pp.5189–5195.

Miesch, A., 1967. Theory of Error in Geochemical Data. , p.17. Available at: http://pubs.er.usgs.gov/publication/pp574A.

Miller, C., Zanetti, A., Thoni, M. & Konzett, J., 2007. Eclogitisation of gabbroic rocks : Redistribution of trace elements and Zr in rutile thermometry in an Eo-Alpine subduction zone (Eastern Alps). *Chemical geology*, 239(1–2), pp.96–123. Available at: http://cat.inist.fr/?aModele=afficheN&cpsidt=18605268 [Accessed September 26, 2016].

Mukhopadhyay, B., 1991. Garnet breakdown in some deep seated garnetiferous xenoliths from the central Sierra Nevada: Petrologic and tectonic implications. *Lithos*, 27(1), pp.59–78.

Nagasawa, H., 1966. Trace element Partition Coefficient in Ionic Crystal. *Science*, 121, pp.767–770.

von Nernst, W., 1891. Verteilung eines Stoffes zwischen zwei Lösungsmitteln und zwischen Lösungsmittel und Dampfraum).

Otamendi, J.E., de la Rosa, J.D., Patino Douce, A.E. & Castro, A., 2002. Rayleigh fractionation of heavy rare earths and yttrium during metamorphic garnet growth. *Geology*, 30(2), pp.159–162.

Peacock, S.M., 1989. Processes Subduction Zones. *Science*, 329, pp.329–337.

Peacock, S.M., 1993. The importance of blueschist — » eclogite dehydration reactions in subducting oceanic crust. , 0(May), pp.684–694.

Pearce, J.A. & Peate, D.W., 1995. Tectonic implications of the composition of Volcanic Arc Magmas. In *Annual Reviews Earth Planet Science*. pp. 251–285.

Pearce, J.A. & Stern, R.J., 2006. Origin of Back-Arc Basin Magmas : Trace Element and Isotope Perspectives. *American Geophysical Union*, pp.63–86.

Pearce, J.A., Stern, R.J., Bloomer, S.H. & Fryer, P., 2005. Geochemical mapping of the Mariana arc-basin system: Implications for the nature and distribution of subduction components.

*Geochemistry, Geophysics, Geosystems*, 6(7).

Pearce, J. a. & Cann, J.R., 1973. Tectonic setting of basic volcanic rocks determined using trace element analyses. *Earth and Planetary Science Letters*, 19, pp.290–300.

Peate, D.W., Pearce, J. a., Hawkesworth, C.J., Colley, H., Edwards, C.M.H. & Hirose, K., 1997. Geochemical Variations in Vanuatu Arc Lavas: the Role of Subducted Material and a Variable Mantle Wedge Composition. *Journal of Petrology*, 38(10), pp.1331–1358. Available at: http://petrology.oxfordjournals.org/content/38/10/1331.abstract.

Perfit, M.R., Gust, D.A., Bence, A.E., Arculus, R.J. & Taylor, S.R., 1980. Chemical Characteristics of Island-Arc Basalts: Implications for Mantle Sources. *Chemical Geology*, 30, pp.227–256.

Plank, T., 2005. Constraints from Thorium/Lanthanum on sediment recycling at subduction zones and the evolution of the continents. *Journal of Petrology*, 46(5), pp.921–944.

Plank, T. & Langmuir, C.H., 1998. The chemical composition of subducting sediment and its consequences for the crust and mantle. *Chemical Geology*, 145(3–4), pp.325–394.

Poli, S., 1993a. The Amphibole-eclogite transformation: an experimental study on basalt.pdf. *American Journal of Science*, 293, pp.1061–1107.

Poli, S., 1993b. The Amphibolite-Ecologite Transformation: An Experimental study on Basalt. *American Journal of Science*, 293, pp.1061–1107.

Poli, S. & Schmidt, M.W., 2004. Experimental Subsolidus Studies on Epidote Minerals. *Reviews in Mineralogy and Geochemistry*, 56(1), pp.171–195. Available at: http://rimg.geoscienceworld.org/cgi/doi/10.2138/gsrmg.56.1.171.

Poli, S. & Schmidt, M.W., 1995. H2O transport and release in subduction zones: Experimental constraints on basaltic and andesitic systems. *Journal of Geophysical Research*, 100(B11), p.22299.

Pozgay, S.H., Wiens, D.A., Conder, J.A., Shiobara, H. & Sugioka, H., 2009. Seismic attenuation tomography of the Mariana subduction system: Implications for thermal structure, volatile distribution, and slow spreading dynamics. *Geochemistry, Geophysics, Geosystems*, 10(4).

Rayleigh, Lord, 1896. Theoretical considerations respecting the separation of gases by diffusion and similar processes. *Philosophical Magazine*, 42(259), pp.493–498.

Ribeiro, J.M., Stern, R.J., Kelley, K.A., Martinez, F., Ishizuka, O., Manton, W.I. & Ohara, Y., 2013. Nature

and distribution of slab-derived fluids and mantle sources beneath the Southeast Mariana forearc rift. *Geochemistry, Geophysics, Geosystems*, 14(10), pp.4585–4607.

Ridolfi, F., Renzulli, A. & Puerini, M., 2010. Stability and chemical equilibrium of amphibole in calc-alkaline magmas: An overview, new thermobarometric formulations and application to subduction-related volcanoes. *Contributions to Mineralogy and Petrology*, 160(1), pp.45–66.

Ringwood, A.E. & Major, A., 1968. High-pressure transformations in pyroxenes II. *Earth and Planetary Science Letters*, 5(4857), pp.76–78. Available at: http://www.nature.com/doifinder/10.1038/196883a0%5Cnpapers2://publication/doi/10.1038/196883a0%5Cnhttp://linkinghub.elsevier.com/retrieve/pii/S0012821X68800172.

Robinson, J.A.C. & Wood, B.J., 1998. The depth of the spinel to garnet transition at the peridotite solidus. *Earth and Planetary Science Letters*, 164(1–2), pp.277–284.

Rudnick, R.L., 1995. Making continental crust. *Nature*, 378(6557), pp.571–578.

Saunders, A.D., Norry, M. & Tarney, J., 1991. Fluid influence on the trace element compositions of subduction zone magmas. *Philosophical Transactions of the Royal Society of London. Series A: Physical and Engineering Sciences*, 335(1638), pp.377–392. Available at: http://rsta.royalsocietypublishing.org/content/335/1638/377.short.

Schmidt, M.W. & Poli, S., 2013. Desvolatilization During Subduction. In K. Turekian & H. Holland, eds. *Treatise on Geochemistry*. Elsevier, pp. 669–701.

Schmidt, M.W. & Poli, S., 2013. Devolatilization During Subduction. In *Treatise on Geochemistry: Second Edition*. pp. 669–701.

Schmidt, M.W. & Poli, S., 1998. Experimentally based water budgets for dehydrating slabs and consequences for arc magma generation. *Earth and Planetary Science Letters*, 163(1–4), pp.361–379. Available at: http://www.sciencedirect.com/science/article/B6V61-3V7HY2H-1F/2/3785fe1f51ab387be9bd447223b17c17.

Schmidt, M.W. & Poli, S., 1994. The stability of lawsonite and zoisite at high pressures: Experiments in CASH to 92 kbar and implications for the presence of hydrous phases in subducted lithosphere. *Earth and Planetary Science Letters*, 124(1–4), pp.105–118.

Schmidt, M.W., Vielzeuf, D. & Auzanneau, E., 2004. Melting and dissolution of subducting crust at high pressures: The key role of white mica. *Earth and Planetary Science Letters*, 228(1–2), pp.65–84.

Shannon, R.D., 1976. Revised Effective Ionic Radii and Systematic Studies of Interatomie Distances in Halides and Chaleogenides Central Research and Development Department , Experimental Station , E . L Du Pont de Nemours The effective ionic radii of Shannon & Prewitt [ Acta.

Sinton, J.M. & Fryer, P., 1987. Mariana Trough Lavas from 18 N: Implications for the Origins of Back Arc Basin Basalts. *Journal of Geophysical Research*, 92(5), pp.782–802.

Sorbadere, F., Schiano, P., Métrich, N. & Bertagnini, A., 2013. Small-scale coexistence of island-arc- and enriched-MORB-type basalts in the central Vanuatu arc. *Contributions to Mineralogy and Petrology*, 166(5), pp.1305–1321.

Sorbadere, F., Schiano, P., Métrich, N. & Garaebiti, E., 2011. Insights into the origin of primitive silica-undersaturated arc magmas of Aoba volcano (Vanuatu arc). *Contributions to Mineralogy and Petrology*, 162(5), pp.995–1009.

Spandler, C., Hermann, J., Arculus, R. & Mavrogenes, J., 2003. Redistribution of trace elements during prograde metamorphism from lawsonite blueschist to eclogite facies; implications for deep subduction-zone processes. *Contributions to Mineralogy and Petrology*, 146(2), pp.205–222.

Spandler, C. & Pirard, C., 2013. Element recycling from subducting slabs to arc crust: A review. *Lithos*, 170–171, pp.208–223. Available at: http://dx.doi.org/10.1016/j.lithos.2013.02.016.

Stalder, R., Foley, S.F., Brey, G.P. & Horn, I., 1998. Mineral-aqueous fluid partitioning of trace elements at 900–1200°C and 3.0–5.7 GPa: new experimental data for garnet, clinopyroxene, and rutile, and implications for mantle metasomatism. *Geochimica et Cosmochimica Acta*, 62(10), pp.1781–1801.

Stern, R.J., Kohut, E., Bloomer, S.H., Leybourne, M., Fouch, M. & Vervoort, J., 2006. Subduction factory processes beneath the Guguan cross-chain, Mariana Arc: No role for sediments, are serpentinites important? *Contributions to Mineralogy and Petrology*, 151(2), pp.202–221.

Stolper, E. & Newman, S., 1994. The role of water in the petrogenesis of Mariana trough magmas. *Earth and Planetary Science Letters*, 121(3–4), pp.293–325.

Stolz, A.J., Jochum, K.P., Spettel, B. & Hofmann, A.W., 1996. Fluid- and melt-related enrichment in the subarc mantle: Evidence from Nb/Ta variations in island-arc basalts. *Geology*, 24(7), pp.587–590.

Syracuse, E.M., van Keken, P.E. & Abers, G.A., 2010. The global range of subduction zone thermal models. *Physics of the Earth and Planetary Interiors*, 183(1–2), pp.73–90. Available at:

http://linkinghub.elsevier.com/retrieve/pii/S0031920110000300.

Tamura, Y. et al., 2014. Mission Immiscible: Distinct subduction components generatetwo primary magmas at Pagan Volcano, Mariana Arc. *Journal of Petrology*, 55(1), pp.63–101.

Tatsumi, Y., 1989. Migration of fluids phases and genesis of basalt magmas in subduction zone. *Journal of Geophysicla Research*, 94, pp.4697–4707.

Tatsumi, Y., Hamilton, D.L. & Nesbitt, R.W., 1986. Chemical characteristics of fluid phase released from a subducted lithosphere and origin of arc magmas: Evidence from high-pressure experiments and natural rocks. *Journal of Volcanology and Geothermal Research*, 29(1–4), pp.293–309. Available at: http://www.sciencedirect.com/science/article/pii/0377027386900491.

Tiepolo, M., Oberti, R., Zanetti, a., Vannucci, R. & Foley, S.F., 2007. Trace-Element Partitioning Between Amphibole and Silicate Melt. *Reviews in Mineralogy and Geochemistry*, 67(1), pp.417–452.

Tribuzio, R., Tiepolo, M., Vannucci, R. & Bottazzi, P., 1999. Trace element distribution within olivine-bearing gabbros from the Northern Apennine ophiolites (Italy): evidence for post-cumulus crystallization in MOR-type gabbroic rocks. *Contributions to Mineralogy and Petrology*, 134(2–3), pp.123–133.

Turner, S.P., Peate, D.W., Hawkesworth, C.J., Eggins, S.M. & Crawford, A.J., 1999. Two mantle domains and the time scales of fluid transfer beneath the Vanuatu arc. *Geology*, 27(11), pp.963–966.

Usui, T., Kobayashi, K., Nakamura, E. & Helmstaedt, H., 2007. Trace element fractionation in deep subduction zones inferred from a lawsonite-eclogite xenolith from the Colorado Plateau. *Chemical Geology*, 239(3–4), pp.336–351.

van Keken, P.E., Hacker, B.R., Syracuse, E.M. & Abers, G.A., 2011. Subduction factory: 4. Depth-dependent flux of H2O from subducting slabs worldwide. *Journal of Geophysical Research: Solid Earth*, 116(1).

Varne, R. & Graham, A.L., 1971. Rare earth abundances in hornblende and clinopyroxene of a hornblende lherzolite xenolith: Implications for upper mantle fractionation processes. *Earth and Planetary Science Letters*, 13(1), pp.11–18.

Walther, J.V. & Helgeson, H.C., 1977. Calculation of the Thermodynamic Properties of Aqueous Silica

and the Solubility of Quartz and Its Polymorphs at High Pressurea and Temperatures. *American Journal of Science*, 277, pp.135–1351.

White, W.M. & Klein, E.M., 2013. *Composition of the Oceanic Crust* 2nd ed., Elsevier Ltd. Available at: http://dx.doi.org/10.1016/B978-0-08-095975-7.00315-6.

Williams, H., Kennedy, M.J. & Neale, E.R.W., 1974. *The Ocean Basins And Margins: the Pacific Ocean*,

Witt-eickschen, G., Kaminsky, W., Kramm, U. & Harte, B., 1998. The Nature of Young Vein Metasomatism in the Lithosphere of the West Eifel ( Germany ): Geochemical and Isotopic Constraints from Composite Mantle Xenoliths from the Meerfelder Maar. *Journal of Petrology*, 39(1), pp.155–185.

Wood, B.J. & Blundy, J.D., 1997. A predictive model for rare earth element partitioning between clinopyroxene and anhydrous silicate melt. *Contributions to Mineralogy and Petrology*, 129(2–3), pp.166–181.

Woodhead, J.D., 1989. Geochemistry of the Mariana arc (western Pacific): Source composition and processes. *Chemical Geology*, 76(1–2), pp.1–24.

Woodland, A., Seitz, H.-M., Altherr, R., Marschall, H., Olker, B. & Ludwig, T., 2002. Li abundances in eclogite minerals: a clue to a crustal or mantle origin? *Contributions to Mineralogy and Petrology*, 143(5), pp.587–601. Available at: http://dx.doi.org/10.1007/s00410-002-0363-8.

Wyllie, P.J. & Tuttle, O.F., 1960. Experimental investigation of silicate systems containing two volatile components part I. Geochemical considerations.pdf. *American Journal of Science*, 258, pp.498–517.

Xiao, Y., Lavis, S., Niu, Y., Pearce, J.A., Li, H., Wang, H. & Davidson, J., 2012. Trace-element transport during subduction-zone ultrahigh-pressure metamorphism: Evidence from Western Tianshan, China. *Bulletin of the Geological Society of America*, 124(7–8), pp.1113–1129.

Yamazaki, T., Seama, N., Okino, K., Kitada, K., Joshima, M., Oda, H. & Naka, J., 2003. Spreading process of the northern Mariana Trough: Rifting-spreading transition at 22??N. *Geochemistry, Geophysics, Geosystems*, 4(9).

Zack, T., Foley, S.F. & Jenner, G.A., 1997. A consistent partition coefficient set for clinopyroxene, amphibole and garnet from laser ablation microprobe analysis of garnet pyroxenite from Kakanui, New Zealand. *N. Jb. Miner. Abh.*, 172, pp.23–41.

Zack, T., Foley, S.F. & Rivers, T., 2002. Equilibrium and Disequilibrium Trace Element Partitioning in Hydrous Eclogites (Trescolmen, Central Alps). *Journal of Petrology*, 43(10), pp.1947–1974.

Zack, T. & John, T., 2007. An evaluation of reactive fluid flow and trace element mobility in subducting slabs. *Chemical Geology*, 237(1–2), pp.5–22.

Zotov, N. & Keppler, H., 2000. In-situ Raman spectra of dissolved silica species in aqueous fluids to 900 °C ad 14 kbar. *American Mineralogist*, 85(3–4), pp.600–604.

Webpages used:

Clemson.ed, (n.d.). *Linear Regression on Excel.* (n.d). [online] Available at https://www.clemson.edu/ces/phoenix/tutorials/excel/regression.html [Accessed at 15 October 2017].

Jassay, D., (n.d.). Investopedia. *How do you calculate the R-squared in excel*. [online] Available at http://www.investopedia.com/ask/answers/012615/how-do-you-calculate-rsquared-excel.asp [Accessed 15 October 2017].

Stattrek.com, (n.d.). *Coefficient of Determination: Definition*. [online] Available at: http://stattrek.com/statistics/dictionary.aspx?definition=coefficient_of_determination [Accessed 15 October 2017].

Investopedia Staff, (n.d.). Investopedia. *Correlation Coefficient*. [online] Available at http://www.investopedia.com/terms/c/correlationcoefficient.asp [Accessed 15 October 2017].

Investopedia Staff, (n.d.). Investopedia. *Coefficient of Determination*. [online] Available at http://www.investopedia.com/terms/c/coefficient-of-determination.asp [Accessed 15 October 2017].

Zady, M., (n.d.). *Z-14: Estimating Analytical Errors Using Regression Statistic – Westgard.* [online] Available at https://www.westgard.com/lesson44.htm [Accessed 15 October 2017].

## Appendix I: Standard deviations (1σ and 2σ) and standard error

The standard deviations and standard errors from each paper are used to show the analytical error of the instruments used in the determination of the partition coefficient. For each mineral, I created a table with the partition coefficient data and the standard deviation/standard error given for each element, in each study. When the information is provided in the original paper, on the label of each table is given information about how the standard deviation and standard error were calculated.

| | Zack et al. (2002) | | |
|---|---|---|---|
| amphibole | **Temperature** | 920˚C | |
| | **Elements** | **Di(min/min)** | **SE** |
| | Li | 0.04 | 22.00 |
| | Be | 0.80 | 15.00 |
| | B | 2.50 | 9.00 |
| | Sr | 0.17 | 22.00 |
| | Y | 3.60 | 14.00 |
| | Zr | 1.40 | 12.00 |
| | Nb | 3.60 | 39.00 |
| | Ba | 187.00 | 36.00 |
| | Ce | 0.18 | 29.00 |
| | Nd | 0.16 | 16.00 |
| | Sm | 0.20 | 15.00 |
| | Pb | 0.30 | 21.00 |
| | Th | 0.22 | 80.00 |
| | U | 0.71 | 48.00 |

**Table 18: Standard error of amphibole-clinopyroxene partition coefficient from Zack et al. (2002).**

| clinopyroxene | Brenan et al. (1995) | | | | | |
|---|---|---|---|---|---|---|
| | **Temperature** | 900˚C | | 900˚C | | 900˚C | |
| | **Element** | **Di(min/fluid)** | **SE** | **Di(min/fluid)** | **SE** | **Di(min/fluid)** | **SE** |
| | Ba | $8.8x10^{-4}$ | $3.3x10^{-4}$ | $4.4x10^{-4}$ | $0.5x10^{-4}$ | $6.6x10^{-4}$ | $1.5x10^{-4}$ |
| | Sr | 4.60 | 0.30 | 3.00 | 0.10 | 1.30 | 0.10 |
| | Pb | 0.05 | 0.011 | 0.03 | 0.002 | 0.04 | 0.004 |

**Table 19: Standard deviation of clinopyroxene-fluid partition coefficient from Brenan et al. (1995). Brenan et al. (1995) measured, at the same temperature, several times the partition coefficient between the cpx and the fluid. The calculations of 1σ error are based on the larger of either counting statistics or replicated analyses.**

| clinopyroxene | Brenan et al. (1995) | | | |
|---|---|---|---|---|
| | **Temperature** | 900˚C | | 900˚C | |
| | **Element** | **Di(min/fluid)** | **SE** | **Di(min/fluid)** | **SE** |
| | Sr | 3.50 | 0.30 | 5.00 | 0.70 |
| | Pb | 5.00 | 0.01 | - | |

**Table 20: Continuation**

| | Brenan et al. (1995) | | | | | | |
|---|---|---|---|---|---|---|---|
| | Temperature | 900˚C | | 900˚C | | 900˚C | |
| | Element | Di(min/fluid) | 1σ[a] | Di(min/fluid) | 1σ[a] | Di(min/luid) | 1σ[a] |
| garnet | Sr | $4.24x10^{-3}$ | $0.6x10^{-3}$ | $134x10^{-3}$ | $64x10^{-3}$ | $394x10^{-3}$ | $34x10^{-3}$ |
| | Ba | $3.24x10^{-4}$ | 1.30 | $3.34x10^{-4}$ | $1.84x10^{-4}$ | | - |
| | Pb | $1.24x10^{-2}$ | $0.84x10^{-2}$ | $1.64x10^{-2}$ | $0.44x10^{-2}$ | | - |
| | Th | 0.08 | 0.04 | | - | | - |
| | U | 0.88 | 0.35 | | - | | - |

**Table 21: Standard deviation for garnet-fluid partition coefficient from Brenan et al. (1995) and Kessel et al. (2005).**
**1σ[a] error based on the larger of either counting statistics or replicated analyses.**
**1σ[b] standard deviation of the distribution of analyses.**

| | Kessel et al. (2005) | | | | | |
|---|---|---|---|---|---|---|
| | Temperature | 700˚C | | 800˚C | | 900˚C | |
| | Element | Di(min/fluid) | 1σ[b] | Di(min/fluid) | 1σ[b] | Di(min/fluid) | 1σ[b] |
| garnet | Li | 51.75 | 9.68 | 37.19 | 7.21 | 67.58 | 13.67 |
| | Be | 24.49 | 16.45 | 29.84 | 12.33 | 21.21 | 4.48 |
| | B | 32.33 | 13.09 | 28.06 | 13.31 | 13.33 | 4.89 |
| | Rb | 1.17 | 0.43 | 0.95 | 0.38 | 0.67 | 0.20 |
| | Cs | 1.56 | 1.13 | 1.31 | 0.76 | 1.93 | 2.61 |
| | Sr | 2.36 | 1.64 | 1.98 | 1.22 | 0.59 | 0.21 |
| | Ba | 2.07 | 1.70 | 1.80 | 1.34 | 1.33 | 0.87 |
| | Ti | 88.78 | 6.82 | 67.79 | 22.47 | 73.79 | 15.22 |
| | Nb | 90.44 | 53.59 | 68.10 | 15.79 | 6.06 | 4.70 |
| | Ta | 65.52 | 39.49 | 51.79 | 15.15 | 6.08 | 5.22 |
| | Zr | 38.26 | 15.27 | 103.22 | 6.56 | 85.03 | 16.91 |
| | Hf | 37.93 | 14.50 | 120.41 | 12.94 | 90.57 | 25.74 |
| | La | 2.24 | 1.21 | 2.50 | 1.43 | 1.21 | 1.08 |
| | Ce | 3.70 | 1.43 | 7.17 | 2.47 | 3.73 | 3.22 |
| | Nd | 37.03 | 7.28 | 66.59 | 16.80 | 41.15 | 16.37 |
| | Sm | 221.91 | 11.86 | 189.48 | 22.34 | 165.83 | 20.83 |
| | Eu | 368.60 | 21.63 | 309.28 | 14.05 | 244.43 | 31.25 |
| | Gd | 550.85 | 33.25 | 382.01 | 33.57 | 330.34 | 36.12 |
| | Dy | 776.01 | 101.75 | 588.00 | 117.99 | 428.50 | 73.96 |
| | Er | 710.77 | 120.83 | 661.02 | 147.51 | 454.23 | 115.42 |
| | Yb | 732.63 | 135.68 | 768.56 | 201.17 | 507.15 | 179.50 |
| | Lu | 417.61 | 78.84 | 453.93 | 110.31 | 300.98 | 114.55 |
| | Y | 37.93 | 14.50 | 120.41 | 12.94 | 90.57 | 25.74 |
| | Sc | 328.52 | 23.83 | 321.00 | 51.65 | 295.52 | 94.64 |
| | Pb | 5.82 | 3.08 | 2.50 | 1.94 | 1.73 | 1.74 |
| | Th | 8.68 | 4.68 | 4.91 | 1.18 | 6.28 | 5.37 |
| | U | 110.56 | 39.42 | 117.86 | 22.65 | 37.71 | 24.84 |

**Table 20: Continuation.**

| lawsonite | Martin et al. (2011) | | | | |
|---|---|---|---|---|---|
| | **Temperature** | 650˚C | | 700˚C | |
| | **Element** | **Di(min/fluid)** | **1σ** | **Di(min/fluid)** | **1σ** |
| | Cs | 0·005 | 0·002 | - | - |
| | Rb | 0·005 | 0·002 | 0·002 | 0·001 |
| | K | 0·05 | 0·03 | 0·07 | 0·05 |
| | Li | 0·01 | 0·01 | 0·0004 | 0·0002 |
| | Ba | 0·01 | 0·01 | 0·006 | 0·003 |
| | Sr | 0·25 | 0·02 | 0·14 | 0·02 |
| | Mg | 0·66 | 0·12 | 1·19 | 0·48 |
| | Be | 6·05 | 1·83 | 0·61 | 0·07 |
| | Ga | 12·55 | 3·49 | 5·86 | 1·45 |
| | B | 0·06 | 0·02 | 0·02 | 0·01 |
| | La | 2·91 | 0·66 | 1·48 | 0·51 |
| | Ce | 4·28 | 1·16 | 1·54 | 0·56 |
| | Pr | 3·80 | 0·80 | 2·67 | 0·80 |
| | Nd | 3·56 | 0·78 | 2·07 | 0·66 |
| | Ms | 3·13 | 0·61 | 1·85 | 0·54 |
| | Eu | 4·29 | 0·93 | 2·22 | 0·65 |
| | Gd | 2·68 | 0·49 | 1·09 | 0·31 |
| | Tb | 2·60 | 0·52 | 1·05 | 0·28 |
| | Dy | 2·69 | 0·50 | 1·00 | 0·27 |
| | Ho | 2·61 | 0·46 | 0·92 | 0·21 |
| | Er | 2·54 | 0·46 | 0·88 | 0·19 |
| | Tm | 2·38 | 0·39 | 0·78 | 0·17 |
| | Yb | 2·34 | 0·31 | 0·90 | 0·18 |
| | Lu | 2·19 | 0·34 | 0·69 | 0·18 |
| | Th | 0·96 | 0·39 | 0·38 | 0·29 |
| | U | - | - | 0·31 | 0·59 |
| | Zr | 0·75 | 0·25 | - | - |
| | Hf | 1·00 | 0·24 | - | - |
| | Nb | 1·08 | 0·83 | - | - |
| | Ta | 0·84 | 0·58 | - | - |

**Table 22: Standard deviation of the average composition of lawsonite-fluid partition coefficient from Martin et al. (2011).**

| rutile | Brenan et al. (1994) | | | | |
|---|---|---|---|---|---|
| | **Temperature** | 900˚C | | 900˚C | |
| | **Element** | **Di(min/fluid)** | **1σ** | **Di(min/fluid)** | **1σ** |
| | Nb | 237.00 | 43.00 | 196.00 | 68.00 |
| | Ta | 189.00 | 47.00 | 147.00 | 46.00 |
| | Hf | 99.00 | 49.00 | - | - |
| | Zr | 206.00 | 149.00 | - | - |
| | U | 0.36 | 0.10 | 89.00 | 21.00 |
| | Th | 4.6x10-4 | 2.3x10-4 | 0.10 | 0.09 |

**Table 23: Standard deviation of rutile-fluid partition coefficient from Brenan et al. (1994). The 1σ error is based on 15-20 EMP analyses from single experiment of different rutile grains.**

| rutile | Brenan et al. (1994) | | | | |
|---|---|---|---|---|---|
| | **Temperature** | 900˚C | | 900˚C | |
| | **Element** | **Di(min/fluid)** | **1σ** | **Di(min/fluid)** | **1σ** |
| | Nb | 187.00 | 61.00 | 167.00 | 54.00 |
| | Ta | 119.00 | 42.00 | 133.00 | 55.00 |

**Table 22: Continuation**

| rutile | Brenan et al. 1994 | | | | | | | |
|---|---|---|---|---|---|---|---|---|
| | Temperature | 900˚C | | 900˚C | | 900˚C | | 900˚C | |
| | **Element** | **Di(min/fluid)** | **1σ** | **Di(min/fluid)** | **1σ** | **Di(min/fluid)** | **1σ** | **Di(min/fluid)** | **1σ** |
| | Nb | 195.00 | 68.00 | 176.00 | 40.00 | 231.00 | 67.00 | 327.00 | 41.00 |
| | Ta | 161.00 | 50.00 | 167.00 | 67.00 | 354.00 | 95.00 | 471.00 | 411.00 |

**Table 22: Continuation**

| rutile | Brenan et al. (1994) | | | | | |
|---|---|---|---|---|---|---|
| | **Temperature** | 900 ˚c | | 1000 ˚c | | 1100 ˚c | |
| | **Element** | **Di(min/fluid)** | **1σ** | **Di(min/fluid)** | **1σ** | **Di(min/fluid)** | **1σ** |
| | Nb | 164.00 | 79.00 | 54.00 | 19.00 | 38.00 | 11.00 |
| | Ta | 115.00 | 61.00 | 65.00 | 29.00 | 41.00 | 24.00 |

**Table 22: Continuation**

| | | Martin et al. (2011) | | | |
|---|---|---|---|---|---|
| | **Temperature** | 700˚C | | 850˚C | |
| | **Element** | **Di(min/fluid)** | **1 σ[c]** | **Di(min/fluid)** | **1 σ[c]** |
| **zoisite** | Cs | 0·002 | 0·001 | 0·01 | 0·01 |
| | Rb | 0·004 | 0·001 | 0·018 | 0·001 |
| | K | NC | NC | NC | NC |
| | Li | 0·003 | 0·003 | 0·004 | 0·003 |
| | Ba | 0·04 | 0·02 | 0·04 | 0·01 |
| | Sr | 3·61 | 1·16 | 2·19 | 0·32 |
| | Mg | 69·53 | 24·12 | 2·15 | 0·93 |
| | Be | 0·12 | 0·02 | 0·07 | 0·04 |
| | Ga | 5·78 | 1·82 | 1·43 | 0·25 |
| | B | 0·04 | 0·01 | NC | NC |
| | La | 0·09 | 0·05 | 2·29 | 0·99 |
| | Ce | 0·20 | 0·12 | 5·06 | 1·16 |
| | Pr | 0·07 | 0·04 | 2·66 | 1·25 |
| | Nd | 0·06 | 0·04 | 2·51 | 1·14 |
| | Sm | 0·09 | 0·06 | 3·07 | 1·23 |
| | Eu | 0·12 | 0·07 | 3·68 | 1·34 |
| | Gd | 0·11 | 0·06 | 2·97 | 1·05 |
| | Tb | 0·16 | 0·09 | 3·39 | 1·01 |
| | Dy | 0·22 | 0·12 | 4·18 | 1·05 |
| | Ho | 0·27 | 0·13 | 4·34 | 0·92 |
| | Er | 0·32 | 0·14 | 5·15 | 1·01 |
| | Tm | 0·42 | 0·18 | 5·48 | 0·83 |
| | Yb | 0·49 | 0·18 | 5·36 | 0·61 |
| | Lu | 0·48 | 0·16 | 5·53 | 0·80 |
| | Th | NC | NC | 1·76 | 0·72 |
| | U | 0·004 | 0·002 | 0·02 | 0·02 |
| | Zr | 0·77 | 0·08 | 1·08 | 0·44 |
| | Hf | 0·81 | 0·08 | 1·53 | 0·40 |
| | Nb | 0·64 | 0·22 | 0·05 | 0·02 |
| | Ta | 2·50 | 0·46 | 0·19 | 0·04 |
| | Y | - | - | - | - |
| | Pb | - | - | - | - |

**Table 24: Standard deviation of zoisite-fluid partition coefficient from Brunsmann et al. (2001), Feineman et al. (2007) and Martin et al. (2011).**
**1σ[c] standard deviation of the average composition.**
**1σ[d] and 1σ[e] standard deviation.**

| zoisite | Freineman et al. (2007) | | | | | | |
|---|---|---|---|---|---|---|---|
| | **Temperature** | 750˚C | | 800˚C | | 900˚C | |
| | **Element** | **Di(min/fluid)** | **1σ$^d$** | **Di(min/fluid)** | **1σ$^d$** | **Di(min/fluid)** | **1σ$^d$** |
| | Cs | - | - | - | - | - | - |
| | Rb | - | - | - | - | - | - |
| | K | - | - | - | - | - | - |
| | Li | - | - | - | - | - | - |
| | Ba | 11.8 | 2.4 | 3.58 | 0.29 | 0.79 | 0.22 |
| | Sr | $2.56x10^4$ | 370 | 165 | 80 | 41.9 | 17.6 |
| | Mg | - | - | - | - | - | - |
| | Be | - | - | - | - | - | - |
| | Ga | - | - | - | - | - | - |
| | B | - | - | - | - | - | - |
| | La | 1.71 | 0.51 | 4.96 | 1.95 | 15.9 | 0.5 |
| | Ce | 1.97 | 0.4 | 6.3 | 2.6 | 44.4 | 4.9 |
| | Pr | - | - | - | - | - | - |
| | Nd | 1.72 | 0.39 | 5.78 | 2.31 | 29.1 | 2.3 |
| | Sm | 1.69 | 0.29 | 6.62 | 2.51 | 25.5 | 2.2 |
| | Eu | 2.48 | 0.25 | 10.5 | 4.1 | 49.9 | 5.4 |
| | Gd | - | - | - | - | - | - |
| | Tb | - | - | - | - | - | - |
| | Dy | - | - | - | - | - | - |
| | Ho | 1.83 | 0.19 | 11.1 | 3.2 | 29.4 | 2.6 |
| | Er | - | - | - | - | - | - |
| | Tm | 2.45 | 0.29 | 14.7 | 4.4 | 22 | 2.4 |
| | Yb | 3.64 | 0.4 | 25.2 | 9.8 | 46.1 | 10.5 |
| | Lu | 3.13 | 0.41 | 20.2 | 6.2 | 25.7 | 3.2 |
| | Th | - | - | - | - | - | - |
| | U | - | - | - | - | - | - |
| | Zr | - | - | - | - | - | - |
| | Hf | - | - | - | - | - | - |
| | Nb | - | - | - | - | - | - |
| | Ta | - | - | - | - | - | - |
| | Y | 27.2 | 9.6 | 10.3 | 3 | 14.2 | 1.6 |
| | Pb | 17.7 | 6.8 | 12.6 | 1 | 1.93 | 0.27 |

**Table 23 Continuation.**

| | | Freineman et al. (2007) | | | | Brunsmann et al. (2001) | |
|---|---|---|---|---|---|---|---|
| | **Temperature** | 900˚C | | 800˚C | | 550˚C | |
| | **Element** | **Di(min/fluid)** | **1σ[d]** | **Di(min/fluid)** | **1σ[d]** | **Di(min/fluid)** | **1σ[e]** |
| **zoisite** | Cs | - | - | - | - | - | - |
| | Rb | - | - | 3.53 | 1.85 | - | - |
| | K | - | - | - | - | - | - |
| | Li | - | - | - | - | - | - |
| | Ba | 2.48 | 1.40 | 2.71 | 0.50 | - | - |
| | Sr | 58.20 | 25.30 | $2.12x10^3$ | 17.20 | - | - |
| | Mg | - | - | - | - | - | - |
| | Be | - | - | - | - | - | - |
| | Ga | - | - | - | - | - | - |
| | B | - | - | - | - | - | - |
| | La | 24.40 | 20.80 | 6.61 | 1.15 | 0.08 | 0.02 |
| | Ce | 1120 | 239.0 | 8.76 | 1.62 | 0.11 | 0.03 |
| | Pr | - | - | - | - | - | - |
| | Nd | 66.60 | 89.20 | 7.62 | 1.54 | 0.19 | 0.05 |
| | Sm | 47.50 | 36.30 | 8.09 | 2.05 | 0.50 | 0.02 |
| | Eu | 81.70 | 41.70 | 10.60 | 2.40 | 0.80 | 0.01 |
| | Gd | - | - | - | - | - | - |
| | Tb | - | - | - | - | - | - |
| | Dy | - | - | - | - | - | - |
| | Ho | 30.20 | 2.20 | 10.40 | 1.90 | - | - |
| | Er | - | - | - | - | - | - |
| | Tm | 24.30 | 7.60 | 11.60 | 1.40 | - | - |
| | Yb | 49.40 | 35.90 | 19.80 | 2.20 | - | - |
| | Lu | 27.60 | 12.80 | 15.10 | 1.40 | - | - |
| | Th | - | - | | 2.60 | - | - |
| | U | - | - | | 2.09 | - | - |
| | Zr | - | - | - | - | - | - |
| | Hf | - | - | - | - | - | - |
| | Nb | - | - | - | - | - | - |
| | Ta | - | - | - | - | - | - |
| | Y | 15.4 | 1.80 | 7.76 | 1.32 | - | - |
| | Pb | 0.83 | 0.19 | 8.59 | 0.60 | - | - |

**Table 23: Continuation.**

## Appendix II: Olivine

### General information

Olivine is the generic name of solid solution between forsterite and fayalite, with structural formula $(Mg,Fe)_2SiO_4$. These orthorhombic minerals have an igneous petrogenesis and can be found in rocks such as basalts, dolerites and gabbros. Metamorphic olivine can result from alteration of basic rocks or iron-rich sediments:

$$2\ \text{Olivine} + 3H_2O \rightleftarrows\ \text{Serpentine} + \text{Brucite} \qquad (A.1)$$

Serpentinisation is a most common alteration of the olivine, and it is a low-grade metamorphic process, under 400°C and at 0.1 GPa (Frost & Beard 2007) (reaction A.1).

REE partitioning between olivine and fluid is temperature-dependent, and an increase of temperature decreases the REE concentration in the olivine (Cullers et al. 1973). $Di$ values are also affected by the fluid composition, and the presence of salt decreases the partitioning (Brenan & Watson 1991). Olivines have a low REE content, with the exception of Yb (Brenan & Watson 1991), and low amounts of LILEs and Sr (Fabbrizio et al. 2013).

In the presence of water, olivine reaches the solidus at 2 GPa and 1400°C (Kushiro & Yoder 1966), so any higher PT conditions were not considered for the calculation of the trace element partitioning. The data from single olivine assemblages were preferred over data from multiple-phase mineral assemblages. Moreover, the *Di* values for olivine were ignored when olivine is in the same mineral assemblage as clinopyroxene or amphibole, since these minerals can influence the Di values for olivine. For this mineral, all published studies used a mixture of pure water and inorganic components such as NaCl, $MgF_2$ and $CaF_2$, and no Di was determined in the presence of only pure $H_2O$. For the prediction of the olivine–fluid partition coefficients, the data from Brenan et al. (1995), Caciagli et al. (2011) and Fabbrizio et al. (2013) are used.

Olivine contains extremely low concentrations of REE and other incompatible trace elements (Lesnov 2010). Therefore, enough data is available to create regressions for only nine trace elements. For the same reason, it is also not possible to predict Di values for these elements on the basis of their ionic radius.

Caciagli et al. (2011) published a linear regression for the calculation of lithium Di values, with $R^2$ = 0.82. This study also provides an alternative exponential equation predicted with data from Fabbrizio et al. (2013) and Caciagli et al. (2011), with $R^2$=0.7057.

Table 24 contains 1 and 2σ standard deviation for olivine-fluid partition coefficient from Caciagli et al. (2011) and Fabbrizio et al. (2013).

| | Caciagli et al (2011) | | |
|---|---|---|---|
| | Element | Li | |
| | Temperature | Di(min/fluid) | 2σ |
| olivine | 1000 | 0.47 | 0.04 |
| | 900 | 0.14 | 0.06 |
| | 1100 | 0.07 | 0.02 |
| | 1200 | 0.47 | 0.04 |
| | 800 | 0.14 | 0.02 |
| | 900 | 1.34 | 0.02 |

**Table 25: Standard deviation of olivine-fluid partition coefficient from Caciagli et al. (2011) and Fabbrizio et al. (2013).**
**1σ standard deviation.**
**2σ standard deviation of n analyses and reflects the degree of sample heterogeneity.**

| Fabbrizio et al. (2013) | | | | | | | | | | | |
|---|---|---|---|---|---|---|---|---|---|---|---|
| olivine | Temperature | 1300˚C | | 1200˚C | | 1100˚C | | 1000˚C | | 900˚C | |
| | Element | Di(min/fluid) | 1σ | Di(min/fluid) | 1σ | Di(min/fluid) | 1σ | Di(min/fluid) | 1σ | Di(min/fluid) | 1σ |
| | Cl | 0.000 | 2.000 | 0.000 | 16.000 | 0.000 | 0.000 | 0.000 | 8.000 | 0.000 | 3.000 |
| | Li | 0.130 | 4.000 | 0.070 | 3.000 | 0.330 | 13.000 | 0.270 | 10.000 | 0.350 | 7.000 |
| | Na | 0.005 | 2.000 | 0.002 | 2.000 | 0.002 | 1.000 | 0.004 | 24.000 | 0.003 | 4.000 |
| | Rb | 0.012 | 11.000 | | - | - | - | 0.002 | 8.000 | - | - |
| | Sr | 0.007 | 4.000 | 0.000 | 8.000 | - | - | 0.006 | 4.000 | 0.003 | 19.000 |
| | Ca | 0.012 | 3.000 | 0.005 | 2.000 | 0.160 | 8.000 | 0.049 | 39.000 | 0.025 | 11.000 |
| | Mg | 3.300 | 38.000 | 9.000 | 3.000 | 38.000 | 9.000 | 81.000 | 37.000 | 122.000 | 93.000 |
| | Mn | 0.460 | 8.000 | 0.780 | 28.000 | 1.170 | 57.000 | 2.000 | 1.000 | 1.400 | 1.000 |
| | Fe | 13.000 | 4.000 | 7.000 | 4.000 | 15.000 | 7.000 | 6.000 | 1.000 | 32.000 | 9.000 |
| | Ni | 113.000 | 32.000 | 45.000 | 27.000 | 113.000 | 71.000 | 243.000 | 113.000 | 175.000 | 15.000 |
| | B | 0.022 | 6.000 | 0.085 | 59.000 | 0.830 | 46.000 | 0.073 | 16.000 | 0.500 | 10.000 |
| | Al | 0.005 | 24.000 | 0.004 | 1.000 | 0.015 | 7.000 | 0.100 | 6.000 | 0.053 | 26.000 |
| | Cr | 0.750 | 8.000 | 1.750 | 81.000 | 12.000 | 4.000 | 5.000 | 4.000 | 21.000 | 6.000 |
| | Sc | 0.130 | 2.000 | 0.280 | 11.000 | 1.380 | 54.000 | 9.000 | 5.000 | - | - |
| | Ce | 0.008 | 40.000 | | 15.000 | 0.022 | 15.000 | 0.012 | 9.000 | 0.016 | 11.000 |
| | Lu | 0.017 | 4.000 | 0.017 | 23.000 | 0.043 | 23.000 | 0.250 | 17.000 | 0.200 | 8.000 |
| | Ti | 0.009 | 3.000 | 0.009 | 6.000 | 0.022 | 6.000 | 0.170 | 8.000 | 0.140 | 5.000 |
| | V | 0.002 | 4.000 | 0.002 | 7.000 | 0.008 | 36.000 | - | - | 0.046 | 27.000 |
| | P | 0.120 | 2.000 | 0.090 | 3.000 | 0.230 | 10.000 | 0.014 | 5.000 | 0.210 | 9.000 |
| | Nb | 0.009 | 3.000 | - | - | - | - | - | - | - | - |
| | Ta | 0.009 | 23.000 | - | - | 0.080 | 4.000 | - | - | - | - |

**Table 26: Continuation.**

### Di coefficients and results

The temperature dependent regressions for Ce, Rb and Sr have only two data points. Other trace element *Di* behaviour is plotted in Figure 36. The Niobium fit has the lowest $R^2$ (0.5507), while other trace elements have an $R^2$ above 0.70 (Table 25). Strontium and the rubidium are the only trace elements for which the Di values have a direct correlation with temperature.

| Element | Coefficients | $R^2$ | Element | Coefficients | $R^2$ |
|---|---|---|---|---|---|
| **Ce** | a = -0.0052 | 1* | **Rb** | a = 0.000085 | 1* |
| | b = 1.8861 | | | b = -4.53302 | |
| **Lu** | a = -0.0046 | 0.7500 | **Sr** | a = 0.04153 | 1* |
| | b = 1.8027 | | | b = -58.9533 | |
| **B** | a = -0.0079 | 0.9787 | **Nb** | a = -0.0055 | 0.5507 |
| | b = 8.5236 | | | b = 2.39008 | |
| **V** | a = -0.00737 | 0.7225 | **Li** | a = -0.0048 | 0.7057 |
| | b = 3.05395 | | | b = 3.9662 | |
| **Cr** | a = -0.0139 | 0.9520 | **Sc** | a = -0.0118 | 0.9608 |
| | b = 17.5545 | | | b = 13.1768 | |

**Table 27: Results from the exponential regressions for the trace elements of olivine, with Di=exp(aT+b). The prediction models use data from Brenan et al. (1995), Caciagli et al. (2011) and Fabbrizio et al. (2013). *These regressions were created with only two data point so the value $R^2$ is not representative.**

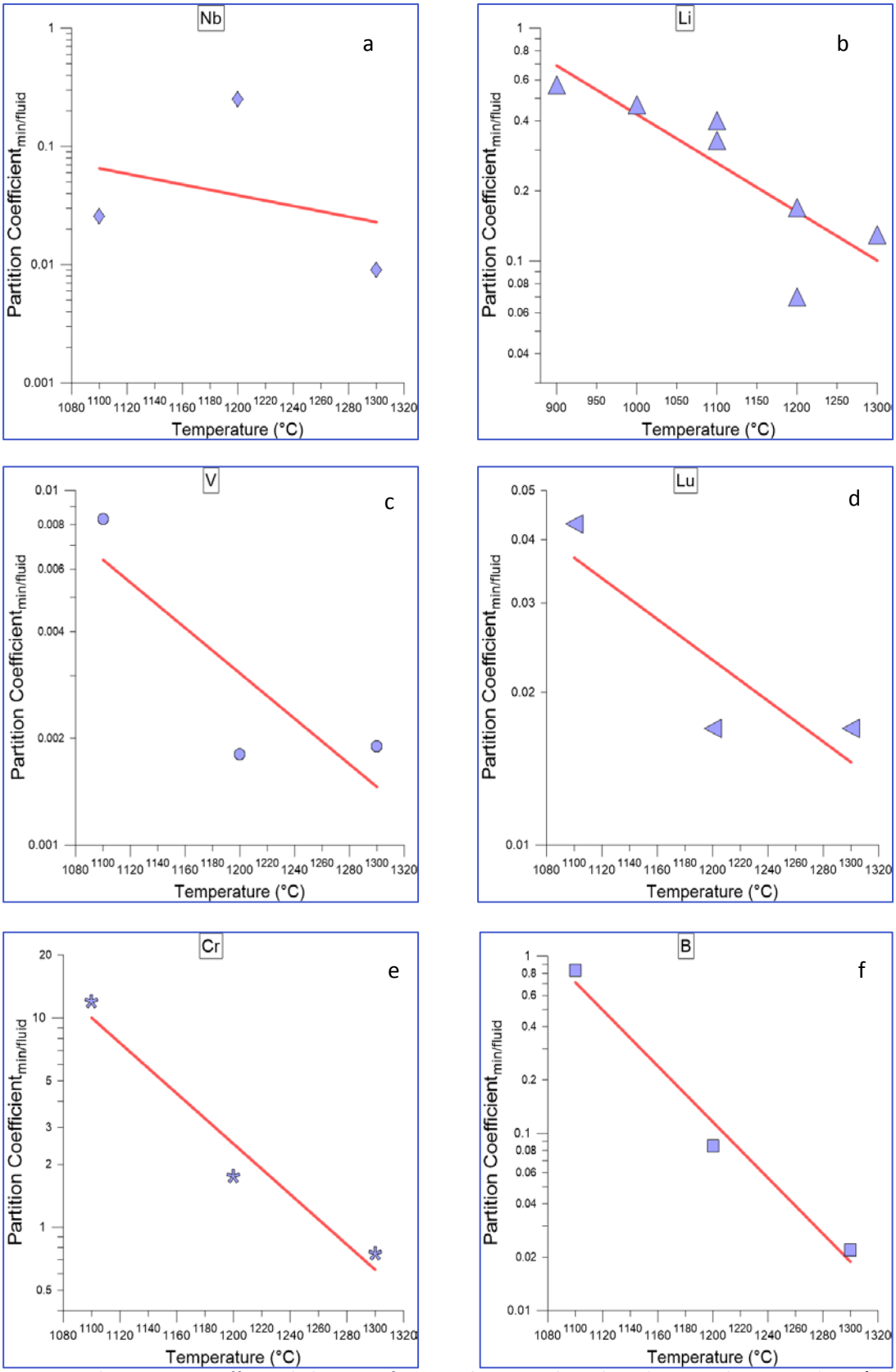


**Figure 36: The partition coefficient behaviour of 6 trace elements when plotted against the ionic radius. a) Nb ($R^2$ = 0.5507) with data from Fabbrizio et al. (2013) and Brenan et al. (1995); b) followed by Li ($R^2$ =0.7057) with data from Caciagli et al. (2011); c) V ($R^2$ =0.7225) with data from Fabbrizio et al. (2013); d) Lu ($R^2$ = 0.75) with data from Fabbrizio et al. (2013); e) Cr ($R^2$ = 0.9520) with data from Fabbrizio et al. (2013); and f) B ($R^2$ = 0.9787 with data from Fabbrizio et al. (2013). The symbols represent the available data for each element and the red line is the best-fit associated to these data.**

## Appendix III: Orthopyroxene

### General information

Orthopyroxene is an orthorhombic pyroxene with a general structural formula $(Mg,Fe)SiO_3$. Ions such as Ca, Mn, Ni, Cr, Al, Ti and $Fe^{3+}$ are present in these pyroxenes but never exceed more than 10 mol% The magnesium-rich member (enstatite) is common in ultrabasic rocks, e.g. lherzolites, pyroxenites and harzburgite. Ferrosilite, the iron-rich member, is rare in igneous rocks but can occur in highly differentiated rocks, e.g. granites (Deer et al., 1992).

$$\text{talc} + \text{forsterite} \rightleftarrows \text{enstatite} + H_2O \qquad \text{(A.2)}$$

Reaction A.2 demonstrates enstatite crystallisation for PT conditions above 700°C and at 0.03 GPa. Enstatite can be stable up to 985°C.

LILE are moderately incompatible with orthopyroxene. The concentrations of REEs in this mineral is between those for clinopyroxene and olivine, and orthopyroxene is depleted in LREE relatively to HREE (Garrido et al. 2000; Fabbrizio et al. 2013; Lesnov 2010).

The available data for orthopyroxene–fluid partitioning is limited, so it is necessary to calculate the mineral–fluid partitioning using opx–cpx partition coefficients and cpx–fluid partition coefficients, as explained in Section 3.1. The data for the orthopyroxene–clinopyroxene partitioning was taken from (Garrido et al. 2000) and for clinopyroxene–fluid from (Kessel et al. 2005). Fabbrizio et al. (2013) performed experiments about orthopyroxene–fluid partitioning at three different temperatures. The experiments at 900°C has a mineral assemblage composed of olivine, orthopyroxene, clinopyroxene and amphibole. The presence of amphibole in the system can buffer the orthopyroxene Di, so the 900°C experiments of Fabbrizio et al. (2013) was not considered in the formulation of the predicted models for this mineral. The data used for the Di parameterisation for this mineral is from Fabbrizio et al. (2013), Garrido et al. (2000) and Kessel et al. (2005).

Table 26 contains 1σ standard deviation for orthopyroxene-fluid partition coefficient from Fabbrizio et al. (2013).

| orthopyroxene | Fabbrizio et al. (2013) | | | | | |
|---|---|---|---|---|---|---|
| | **Temperature** | 1100˚C | | 1000˚C | | 900˚C | |
| | **Element** | **Di(min/fluid)** | **1σ** | **Di(min/fluid)** | **1σ** | **Di(min/fluid)** | **1σ** |
| | Cl | 0.00017 | 8 | 0.00037 | 3 | 0.00015 | 7 |
| | Li | 0.31 | 9 | 0.18 | 6 | 0.48 | 7 |
| | Na | 0.018 | 2 | 0.002 | 0 | 0.018 | 3 |
| | Rb | 0.008 | 5 | - | - | - | - |
| | Sr | 0.0018 | 9 | 0.0021 | 14 | 0.0034 | 23 |
| | Ca | 0.58 | 24 | 0.96 | 73 | 0.78 | 34 |
| | Mg | 24 | 6 | 51 | 23 | 77 | 59 |
| | Mn | 4 | 2 | 4 | 2 | 4.1 | 1 |
| | Fe | 32 | 14 | 10 | 2 | 60 | 15 |
| | Ni | 50 | 32 | 94 | 44 | 80 | 7 |
| | B | 0.8 | 4 | - | - | - | - |
| | Al | 0.86 | 25 | 4 | 2 | 3 | 2 |
| | Cr | 4 | 1 | 24 | 15 | 15 | 5 |
| | Sc | 23 | 6 | 76 | 38 | - | - |
| | Ce | 0.015 | 9 | - | - | - | - |
| | Lu | 1.3 | 6 | 4 | 3 | 8 | 3 |
| | Y | 0.41 | 19 | 0.27 | 22 | 0.54 | 26 |
| | Ti | 0.51 | 12 | 4 | 2 | 4 | 1 |
| | Zr | 0.042 | 26 | - | - | - | - |
| | V | 0.039 | 17 | 0.073 | 65 | 0.22 | 12 |
| | Pr | 0.22 | 10 | 0.28 | 7 | 0.35 | 17 |

**Table 28: Standard deviation of orthopyroxene-fluid partition coefficient from Fabbrizio et al. (2013).**

| orthopyroxene | Fabbrizio et al. (2013) | | | |
|---|---|---|---|---|
| | **Temperature** | 1100˚C | 1000˚C | 900˚C |
| | **Element** | **1σ** | | |
| | Cl | 8 | 3 | 7 |
| | Li | 9 | 6 | 7 |
| | Na | 2 | 0 | 3 |
| | Rb | 5 | - | - |
| | Sr | 9 | 14 | 23 |
| | Ca | 24 | 73 | 34 |
| | Mg | 6 | 23 | 59 |
| | Mn | 2 | 2 | 1 |
| | Fe | 14 | 2 | 15 |
| | Ni | 32 | 44 | 7 |
| | B | 4 | - | - |
| | Al | 25 | 2 | 2 |
| | Cr | 1 | 15 | 5 |
| | Sc | 6 | 38 | - |
| | Ce | 9 | - | - |
| | Lu | 6 | 3 | 3 |
| | Y | 19 | 22 | 26 |
| | Ti | 12 | 2 | 1 |
| | Zr | 26 | - | - |
| | V | 17 | 65 | 12 |
| | Pr | 10 | 7 | 17 |

**Table 29: Continuation.**

### Calculation of the missing REE data

| T | Coefficients | $R^2$ |
|---|---|---|
| **700** | a = -14.1773 | 0.7847 |
| | b = 14.25055 | |
| **800** | a = -21.8792 | 0.9167 |
| | b = 21.77988 | |
| **900** | a = -29.9455 | 0.9288 |
| | b = 28.97896 | |

**Table 30: The coefficients and the $R^2$ resulting from the exponential regression used for the prediction of the missing REE.**

Figure 37 shows the behaviour of $Di_{(REE)}$ plotted versus the ionic radius for three different temperatures. Ce and Eu are the only elements for which Di values deviate considerably from the best-fit line. At 700 and 800°C, the partition coefficients decrease by one order of magnitude between La and Lu, and at 900°C, the Di values decrease by two orders of magnitude, when plotted versus the ionic radius. The $R^2$ value is above 0.70 for the three predictions. praseodymium, terbium,

dysprosium and dolmium are the elements which Di's values were predicted using this method. Table 27 contains all the coefficients and the $R^2$ that results from these predictions.

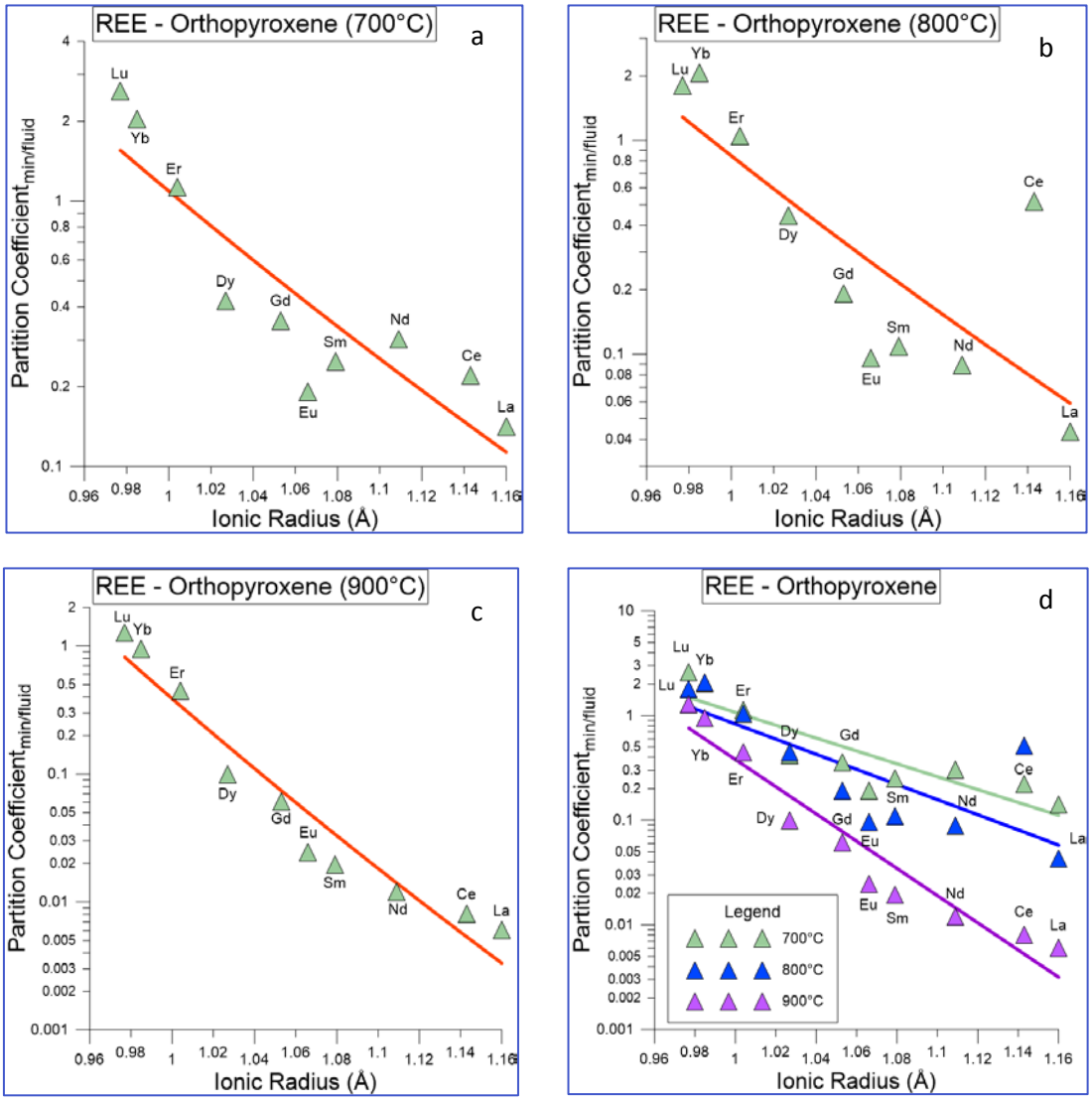


**Figure 37: The partition coefficient behaviour plotted versus the ionic radius of orthopyroxene: a) 700˚C exponential regression; b) 800˚C with exponential regression; and c) 900˚C with exponential regression. The spades symbols represent the calculated data from Garrido et al. (2000) and Kessel et al. (2005), and the red line is representing the best possible fit to this data. d) contains the all REE´s partition coefficients plotted together. the red line is the best-fit associate to these data.**

## Di coefficients and results

Exponential equations were used to calculate the partition coefficients behaviours. From 38 trace elements *Di*'s predictions, 4 of the regressions have $R^2$ under 0.7, and 14 of the regressions have $R^2$above 0.9 (Table 28). Figure 36 contains three examples of the worst and the best fit produced for the prediction of *Di*'s behaviour.

| Element | Coefficients | $R^2$ | Element | Coefficients | $R^2$ |
|---|---|---|---|---|---|
| **La** | a = -0.0158<br>b = 9.2460 | 0.9795 | **Lu** | a = -0.00059<br>b = 1.22018 | 0.0369 |
| **Ce** | a = -0.0066<br>b = 2.4113 | 0.5974 | **Zr** | a = -0.0129<br>b = 10.2702 | 0.7978 |
| **Pr** | a = 0.00198<br>b = -3.6221 | 0.2659 | **Hf** | a = -0.0173<br>b = 13.5177 | 0.9969 |
| **Nd** | a = -0.0161<br>b = 10.2207 | 0.9810 | **Nb** | a = -0.0125<br>b = 9.8904 | 0.8007 |
| **Sm** | a = -0.0127<br>b = 7.6820 | 0.9614 | **Ba** | a = -0.0075<br>b = 4.2286 | 0.9973 |
| **Eu** | a = -0.01028<br>b = 5.6544 | 0.9656 | **Sr** | a = -0.0098<br>b = 3.68497 | 0.8402 |
| **Gd** | a = -0.0088<br>b = 5.2005 | 0.9828 | **Ta** | a = -0.0157<br>b = 12.3346 | 0.9995 |
| **Tb** | a = -0.0084<br>b = 5.4709 | 0.9633 | **Th** | a = -0.0175<br>b = 13.8396 | 0.9493 |
| **Dy** | a = -0.0072<br>b = 4.4636 | 0.7196 | **U** | a = -0.0149<br>b = 9.9067 | 0.9608 |
| **Y** | a = 0.0042<br>b = -5.4867 | 1* | **Li** | a = 0.0054<br>b = - 7.15095 | 1* |
| **Ho** | a = -0.0064<br>b = 4.4441 | 0.9088 | **Cr** | a = 0.0179<br>b = -16.5313 | 1* |
| **Er** | a = -0.0047<br>b = 3.50479 | 0.8105 | **V** | a = -0.0063<br>b = 3.6517 | 1* |
| **Tm** | a = -0.004<br>b = 2.9672 | 0.7356 | **Rb** | a = -0.0019<br>b = 2.439 | 0.2609 |
| **Yb** | a = -0.0038<br>b = 3.371 | 0.7417 | **Sc** | a = 0.0084<br>b = -5.2045 | 0.9254 |

**Table 31: Results from the linear regressions for the trace elements of orthopyroxene, with Di=exp(aT+b). *These regressions were created with only two data point so the value $R^2$ is not representative.**

For the available data of ortopyroxene the behaviour of the partition coefficients of trace elements in the same group are not so homogeneous as other minerals (Figure 39). The partition coefficient behaviour has an inverse correlation with the temperature for most of the trace elements, with the exception of yttrium, praseodymium, lithium, chromium and scandium. The variation of the *Di´*s value is between one and two orders of magnitude.

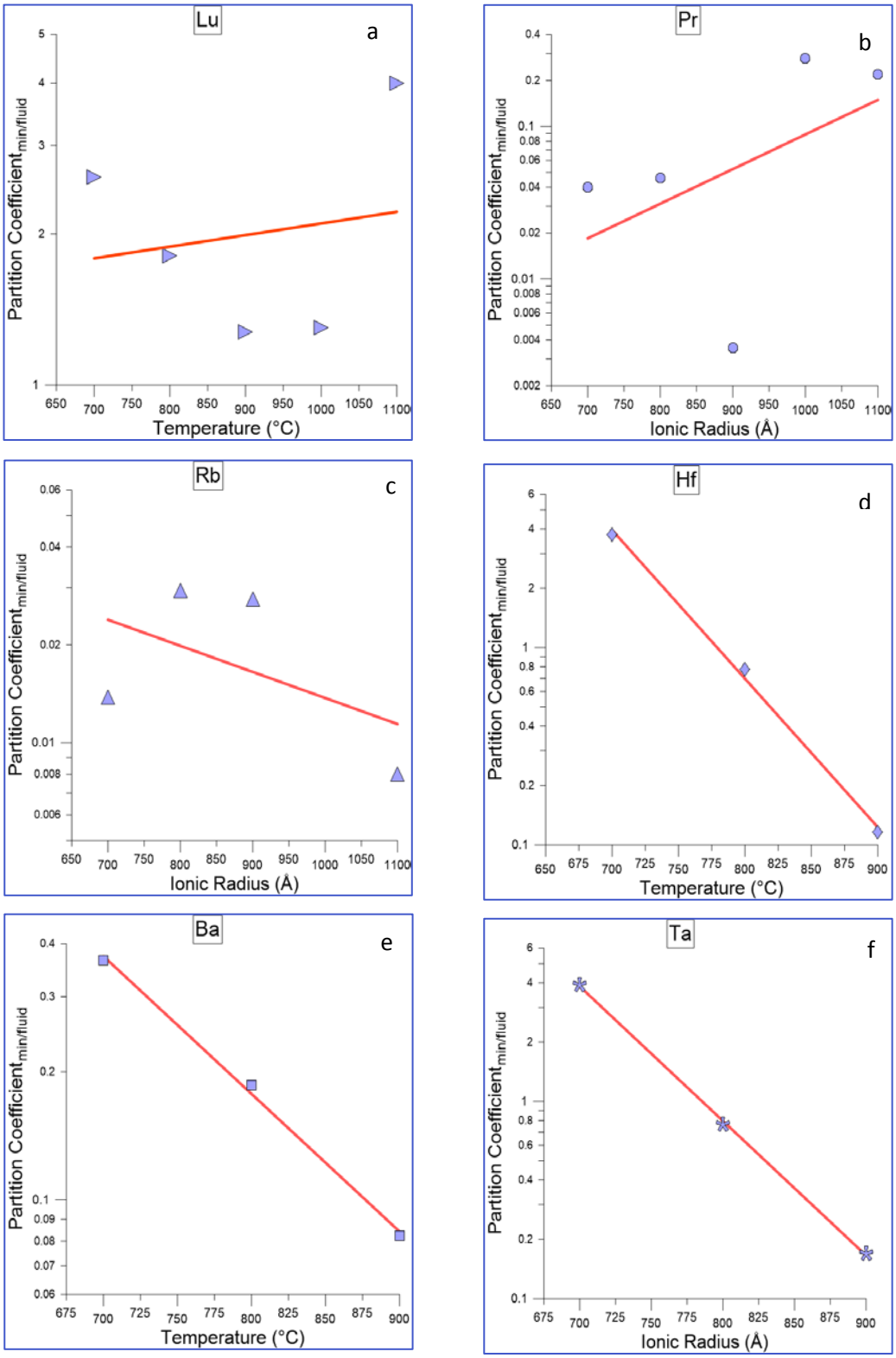


**Figure 38: The partition coefficient behaviour of 6 trace elements when plotted against the ionic radius. a) Lu ($R^2$ = 0.0369) with data from Fabbrizio et al. (2013), Garrido et al. (2000) and Kessel et al. (2005); b) Pr ($R^2$ =0.2659) with data from Fabbrizio et al. (2013), Garrido et al. (2000) and Kessel et al. (2005); c) Rb ($R^2$ = 0.2609) with data from Fabbrizio et al. (2013), Garrido et al. (2000) and Fabbrizio et al. (2013); d) Hf ($R^2$ = 0.9969) with data from Garrido et al. (2000) and Kessel et al. (2005); e) Ba ($R^2$= 0.9973) with data from Garrido et al. (2000) and Kessel et al. (2005); and f) Ta ($R^2$ = 0.9995) with data from Garrido et al. (2000) and Kessel et al. (2005). The symbols represent the available data for each element and the red line is the best-fit associate to these data.**

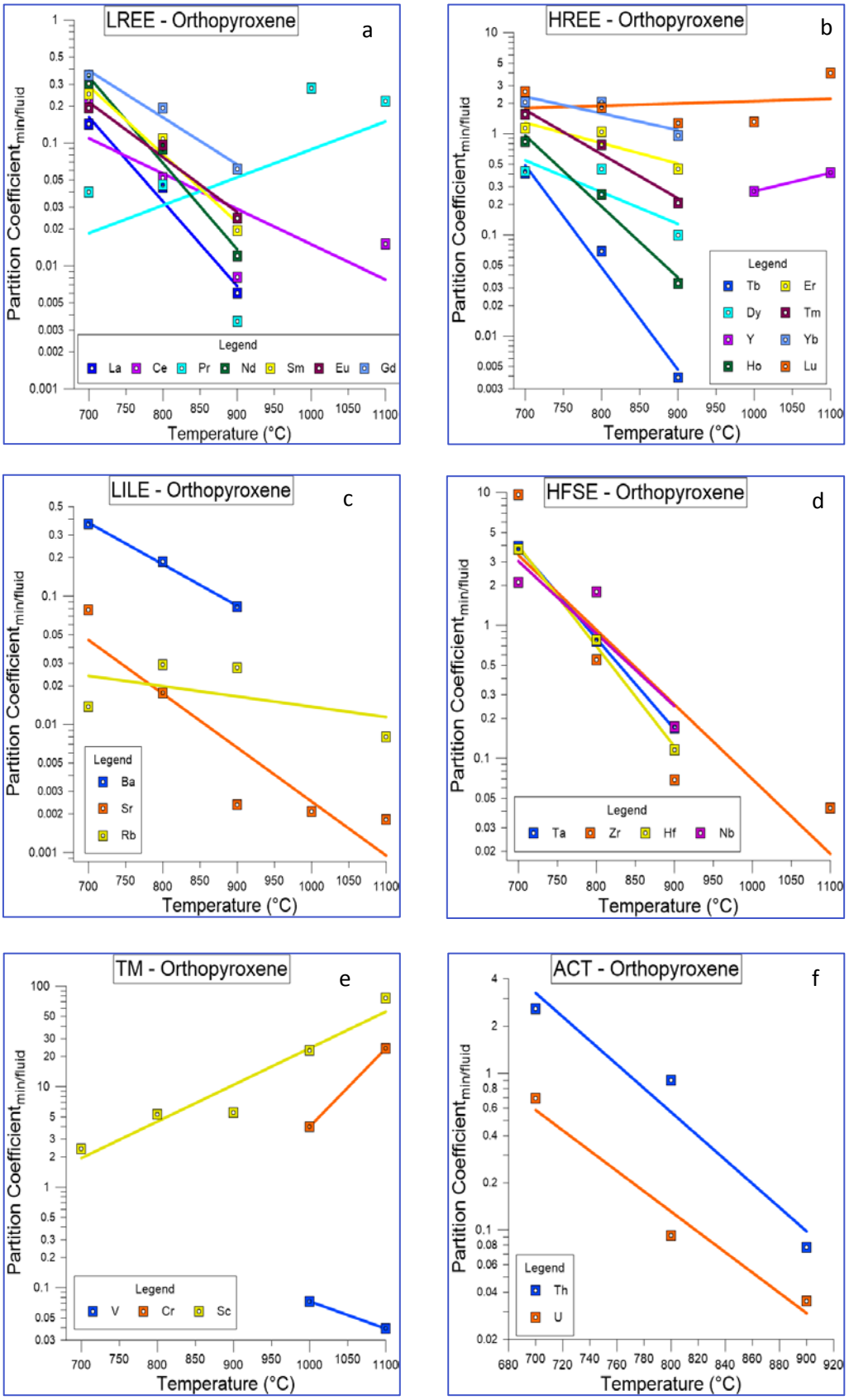


**Figure 39: Diagram with partition coefficient plotted against the temperature for: a) Light Rare Earth elements; b) Heavy Rare Earth elements; c) Large-ion Lithophile elements; d) Highfield-strength elements; e) Transition metals; and f) Actinide element. The data is from Garrido et al. (2000), Fabbrizio et al. (2013) and Kessel et al. (2005). The squares and lines represent the available data and the respective fit lines.**

## Appendix IV: Northern Mariana Fluid Results

| Fluids | Rb, ppm | Ba, ppm | Sr, ppm | Li, ppm | B, ppm | La, ppm | Ce, ppm | Pr, ppm | Nd, pm | Sm, ppm | Eu, ppm | Gd, ppm | Tb, ppm |
|---|---|---|---|---|---|---|---|---|---|---|---|---|---|
| **1st** | 535.10 | 0.0542 | 1.2162 | 0.0000 | 1.2610 | 0.0360 | 0.0506 | 0.0070 | 0.0340 | 0.0086 | 0.0036 | 0.0097 | 0.0024 |
| **2nd** | 615.39 | 0.0765 | 1.4107 | 0.0000 | 1.4198 | 0.0406 | 0.0576 | 0.0079 | 0.0378 | 0.0092 | 0.0038 | 0.0101 | 0.0025 |
| **3rd** | 700.13 | 0.1040 | 1.5876 | 0.0001 | 1.5464 | 0.0454 | 0.0654 | 0.0088 | 0.0414 | 0.0095 | 0.0039 | 0.0101 | 0.0025 |
| **4th** | 787.13 | 0.1362 | 1.9026 | 0.0003 | 1.7769 | 0.0514 | 0.0746 | 0.0100 | 0.0466 | 0.0106 | 0.0043 | 0.0110 | 0.0027 |
| **5th** | 874.43 | 0.1727 | 2.2110 | 0.0008 | 1.9759 | 0.0580 | 0.0848 | 0.0113 | 0.0519 | 0.0114 | 0.0045 | 0.0115 | 0.0028 |
| **6th** | 960.59 | 0.2143 | 2.5691 | 0.0022 | 2.1921 | 0.0653 | 0.0964 | 0.0128 | 0.0577 | 0.0123 | 0.0048 | 0.0121 | 0.0029 |
| **7th** | 1028.00 | 0.2623 | 2.9818 | 0.0061 | 2.4190 | 0.0737 | 0.1094 | 0.0144 | 0.0641 | 0.0133 | 0.0051 | 0.0128 | 0.0030 |
| **8th** | 1087.90 | 0.3212 | 3.4583 | 0.0172 | 2.6674 | 0.0829 | 0.1237 | 0.0162 | 0.0713 | 0.0144 | 0.0055 | 0.0135 | 0.0031 |
| **9th** | 1117.40 | 0.3969 | 3.9978 | 0.0491 | 2.9261 | 0.0934 | 0.1400 | 0.0182 | 0.0791 | 0.0156 | 0.0058 | 0.0142 | 0.0032 |
| **10th** | 1144.60 | 0.5099 | 4.6164 | 0.1395 | 3.2185 | 0.1047 | 0.1572 | 0.0203 | 0.0877 | 0.0169 | 0.0062 | 0.0150 | 0.0034 |
| **11th** | 1126.80 | 0.6957 | 5.3095 | 0.3973 | 3.5267 | 0.1172 | 0.1763 | 0.0227 | 0.0971 | 0.0183 | 0.0066 | 0.0159 | 0.0035 |
| **12th** | 1094.50 | 1.0930 | 6.0788 | 1.0918 | 3.8593 | 0.1308 | 0.1967 | 0.0253 | 0.1071 | 0.0198 | 0.0071 | 0.0167 | 0.0036 |
| **13th** | 1059.70 | 2.6121 | 6.9273 | 2.6319 | 4.2236 | 0.1455 | 0.2182 | 0.0280 | 0.1178 | 0.0214 | 0.0076 | 0.0176 | 0.0038 |
| **14th** | 1142.60 | 6.9829 | 7.9763 | 4.7506 | 4.6108 | 0.1650 | 0.2477 | 0.0317 | 0.1319 | 0.0233 | 0.0081 | 0.0187 | 0.0040 |
| **15th** | 1016.50 | 8.3041 | 9.2878 | 6.4745 | 4.9773 | 0.1907 | 0.2876 | 0.0367 | 0.1501 | 0.0257 | 0.0088 | 0.0201 | 0.0042 |
| **16th** | 1150.70 | 9.7821 | 10.7718 | 7.4296 | 5.3900 | 0.2202 | 0.3331 | 0.0423 | 0.1705 | 0.0283 | 0.0095 | 0.0215 | 0.0044 |
| **17th** | 1140.20 | 11.4487 | 12.4830 | 7.9103 | 5.7941 | 0.2546 | 0.3863 | 0.0489 | 0.1939 | 0.0311 | 0.0103 | 0.0230 | 0.0046 |
| **18th** | 1104.80 | 13.3261 | 14.4466 | 8.2019 | 6.2014 | 0.2947 | 0.4482 | 0.0566 | 0.2205 | 0.0343 | 0.0111 | 0.0246 | 0.0048 |
| **19th** | 1178.00 | 15.4388 | 16.6760 | 8.4284 | 6.6465 | 0.3407 | 0.5191 | 0.0654 | 0.2507 | 0.0378 | 0.0120 | 0.0264 | 0.0051 |

**Table 32: Trace element composition of the fluids that result from my models, for Northern Mariana.**

| Fluids | Dy, ppm | Y, ppm | Ho, ppm | Er, ppm | Tm, ppm | Yb, ppm | Lu, ppm | Th, ppm | U, ppm | Zr, ppm | Hf, ppm |
|---|---|---|---|---|---|---|---|---|---|---|---|
| **1st** | 0.0181 | 0.2714 | 0.0033 | 0.0115 | 0.0012 | 0.0073 | 0.0012 | 0.00058801 | 0.0039 | 0.0979 | 0.0029 |
| **2nd** | 0.0186 | 0.289 | 0.0034 | 0.0119 | 0.0013 | 0.0074 | 0.0012 | 0.00066916 | 0.0042 | 0.1124 | 0.0033 |
| **3rd** | 0.0184 | 0.3062 | 0.0033 | 0.0118 | 0.0013 | 0.0073 | 0.0012 | 0.00075718 | 0.0044 | 0.1273 | 0.0037 |
| **4th** | 0.0196 | 0.3251 | 0.0035 | 0.0125 | 0.0014 | 0.0077 | 0.0013 | 0.00086527 | 0.005 | 0.1472 | 0.0042 |
| **5th** | 0.0202 | 0.3433 | 0.0036 | 0.0128 | 0.0014 | 0.0079 | 0.0013 | 0.00098463 | 0.0054 | 0.168 | 0.0047 |
| **6th** | 0.0207 | 0.3617 | 0.0037 | 0.013 | 0.0014 | 0.008 | 0.0013 | 0.0011 | 0.0059 | 0.1914 | 0.0053 |
| **7th** | 0.0212 | 0.3802 | 0.0038 | 0.0132 | 0.0015 | 0.0082 | 0.0014 | 0.0013 | 0.0064 | 0.2175 | 0.0059 |
| **8th** | 0.0218 | 0.3987 | 0.0039 | 0.0134 | 0.0015 | 0.0083 | 0.0014 | 0.0014 | 0.007 | 0.2467 | 0.0066 |
| **9th** | 0.0224 | 0.4174 | 0.004 | 0.0136 | 0.0015 | 0.0084 | 0.0014 | 0.0016 | 0.0076 | 0.279 | 0.0073 |
| **10th** | 0.023 | 0.4362 | 0.0041 | 0.0138 | 0.0016 | 0.0086 | 0.0015 | 0.0018 | 0.0083 | 0.3151 | 0.0081 |
| **11th** | 0.0237 | 0.4553 | 0.0043 | 0.014 | 0.0016 | 0.0087 | 0.0015 | 0.0021 | 0.0091 | 0.3549 | 0.009 |
| **12th** | 0.0243 | 0.4746 | 0.0044 | 0.0142 | 0.0016 | 0.0089 | 0.0015 | 0.0023 | 0.0099 | 0.3984 | 0.0099 |
| **13th** | 0.0249 | 0.4941 | 0.0045 | 0.0143 | 0.0016 | 0.009 | 0.0015 | 0.0026 | 0.0109 | 0.4456 | 0.0108 |
| **14th** | 0.0255 | 0.5069 | 0.0046 | 0.0144 | 0.0017 | 0.0091 | 0.0016 | 0.003 | 0.0121 | 0.4983 | 0.0121 |
| **15th** | 0.0264 | 0.5163 | 0.0048 | 0.0146 | 0.0017 | 0.0093 | 0.0016 | 0.0034 | 0.0135 | 0.5595 | 0.0139 |
| **16th** | 0.0272 | 0.524 | 0.0049 | 0.0147 | 0.0017 | 0.0095 | 0.0016 | 0.004 | 0.0152 | 0.6259 | 0.0158 |
| **17th** | 0.0281 | 0.532 | 0.0051 | 0.0149 | 0.0018 | 0.0096 | 0.0016 | 0.0047 | 0.0172 | 0.7001 | 0.0181 |
| **18th** | 0.029 | 0.5396 | 0.0053 | 0.015 | 0.0018 | 0.0098 | 0.0016 | 0.0055 | 0.0197 | 0.7824 | 0.0207 |
| **19th** | 0.03 | 0.5462 | 0.0054 | 0.0152 | 0.0018 | 0.01 | 0.0017 | 0.0064 | 0.0227 | 0.8732 | 0.0236 |

**Table 20: Continuation.**

| Fluids | 'Nb' | 'Ta' | 'Pb' | 'Be' |
|---|---|---|---|---|
| **1st** | 0.00018397 | 0.000020845 | 0.0156 | 0.00029212 |
| **2nd** | 0.00028334 | 0.00002492 | 0.0176 | 0.00045438 |
| **3rd** | 0.0004329 | 0.000028612 | 0.0198 | 0.00070892 |
| **4th** | 0.00065357 | 0.000035852 | 0.0225 | 0.0011 |
| **5th** | 0.00097508 | 0.000043122 | 0.0255 | 0.0017 |
| **6th** | 0.0014 | 0.000051985 | 0.0293 | 0.0028 |
| **7th** | 0.0021 | 0.000062677 | 0.0335 | 0.0044 |
| **8th** | 0.0029 | 0.000075785 | 0.0387 | 0.0069 |
| **9th** | 0.0041 | 0.000091328 | 0.0454 | 0.0112 |
| **10th** | 0.0055 | 0.00011072 | 0.0532 | 0.0179 |
| **11th** | 0.0072 | 0.00013378 | 0.0637 | 0.0289 |
| **12th** | 0.0093 | 0.00016124 | 0.0782 | 0.0472 |
| **13th** | 0.0117 | 0.00019386 | 0.0992 | 0.0771 |
| **14th** | 0.0148 | 0.00023521 | 0.1261 | 0.12 |
| **15th** | 0.0189 | 0.00028838 | 0.1611 | 0.1768 |
| **16th** | 0.0239 | 0.00035244 | 0.2141 | 0.2482 |
| **17th** | 0.0298 | 0.00043083 | 0.3018 | 0.3287 |
| **18th** | 0.037 | 0.00052632 | 0.471 | 0.4096 |
| **19th** | 0.0453 | 0.00064273 | 0.8698 | 0.4803 |

**Table 20: Continuation.**

## Appendix V: Northern Vanuatu Fluid Results

| Fluids | Rb, ppm | Ba, ppm | Sr, ppm | Li, ppm | B, ppm | La, ppm | Ce, ppm | Pr, ppm | Nd, pm | Sm, ppm | Eu, ppm | Gd, ppm |
|---|---|---|---|---|---|---|---|---|---|---|---|---|
| **1st** | 674.91 | 0.1205 | 1.9248 | 0.0001 | 1.7324 | 0.0483 | 0.0682 | 0.0095 | 0.0455 | 0.0113 | 0.0046 | 0.0122 |
| **2nd** | 741.53 | 0.1588 | 2.2161 | 0.0004 | 1.9350 | 0.0543 | 0.0775 | 0.0107 | 0.0505 | 0.0121 | 0.0049 | 0.0127 |
| **3rd** | 819.79 | 0.2035 | 2.5507 | 0.0011 | 2.1526 | 0.0610 | 0.0879 | 0.0120 | 0.0561 | 0.0130 | 0.0052 | 0.0133 |
| **4th** | 893.84 | 0.2559 | 2.9356 | 0.0028 | 2.3857 | 0.0686 | 0.0997 | 0.0135 | 0.0622 | 0.0140 | 0.0055 | 0.0139 |
| **5th** | 960.82 | 0.3187 | 3.3756 | 0.0076 | 2.6342 | 0.0772 | 0.1130 | 0.0152 | 0.0690 | 0.0151 | 0.0058 | 0.0145 |
| **6th** | 1014.11 | 0.3982 | 3.8788 | 0.0207 | 2.9020 | 0.0867 | 0.1277 | 0.0170 | 0.0766 | 0.0162 | 0.0062 | 0.0152 |
| **7th** | 1051.83 | 0.5057 | 4.4477 | 0.0564 | 3.1861 | 0.0974 | 0.1442 | 0.0191 | 0.0848 | 0.0175 | 0.0065 | 0.0160 |
| **8th** | 1068.89 | 0.6685 | 5.0885 | 0.1544 | 3.4899 | 0.1092 | 0.1623 | 0.0214 | 0.0939 | 0.0188 | 0.0069 | 0.0168 |
| **9th** | 1065.43 | 0.9633 | 5.8028 | 0.4204 | 3.8146 | 0.1221 | 0.1819 | 0.0239 | 0.1036 | 0.0203 | 0.0074 | 0.0176 |
| **10th** | 1091.76 | 1.7042 | 6.5894 | 1.1011 | 4.1664 | 0.1361 | 0.2030 | 0.0265 | 0.1140 | 0.0218 | 0.0078 | 0.0185 |
| **11th** | 1003.11 | 1.5855 | 7.3903 | 2.5018 | 4.4332 | 0.1507 | 0.2258 | 0.0294 | 0.1252 | 0.0235 | 0.0083 | 0.0194 |
| **12th** | 1114.25 | 7.3908 | 8.6118 | 4.6043 | 4.9079 | 0.1741 | 0.2610 | 0.0338 | 0.1416 | 0.0255 | 0.0089 | 0.0205 |
| **13th** | 1078.04 | 8.7745 | 9.9236 | 6.4455 | 5.2721 | 0.2001 | 0.3015 | 0.0388 | 0.1599 | 0.0278 | 0.0095 | 0.0217 |
| **14th** | 716.82 | 2.5370 | 0.0004 | 8.1730 | 5.7568 | 0.2396 | 0.3616 | 0.0457 | 0.1849 | 0.0307 | 0.0103 | 0.0232 |
| **15th** | 1232.52 | 4.4042 | 0.0014 | 8.6501 | 7.3376 | 0.3523 | 0.5335 | 0.0681 | 0.2696 | 0.0429 | 0.0137 | 0.0302 |
| **16th** | 1161.50 | 5.9232 | 0.0028 | 8.9979 | 8.4093 | 0.4608 | 0.6996 | 0.0899 | 0.3530 | 0.0549 | 0.0171 | 0.0371 |
| **17th** | 1133.46 | 8.4099 | 0.0054 | 9.1249 | 8.7722 | 0.5256 | 0.8000 | 0.1029 | 0.3989 | 0.0606 | 0.0185 | 0.0399 |
| **18th** | 1102.78 | 10.5197 | 0.0088 | 9.2755 | 9.2012 | 0.6008 | 0.9163 | 0.1181 | 0.4546 | 0.0679 | 0.0204 | 0.0437 |
| **19th** | 1071.04 | 13.3143 | 0.0146 | 9.4249 | 9.5899 | 0.6871 | 1.0503 | 0.1356 | 0.5180 | 0.0760 | 0.0225 | 0.0477 |
| **20th** | 1041.26 | 17.0435 | 0.0250 | 9.5738 | 9.9378 | 0.7863 | 1.2047 | 0.1557 | 0.5902 | 0.0850 | 0.0248 | 0.0521 |
| **21st** | 1014.75 | 22.1570 | 0.0451 | 9.7238 | 10.2433 | 0.9003 | 1.3827 | 0.1790 | 0.6723 | 0.0950 | 0.0272 | 0.0569 |
| **22nd** | 989.54 | 28.0825 | 0.0794 | 9.8848 | 10.5184 | 1.0324 | 1.5894 | 0.2060 | 0.7668 | 0.1063 | 0.0300 | 0.0621 |
| **23rd** | 959.71 | 40.6214 | 0.2170 | 10.0363 | 10.7143 | 1.1844 | 1.8274 | 0.2385 | 0.8719 | 0.1182 | 0.0328 | 0.0673 |
| **24th** | 915.72 | 73.6132 | 67.2303 | 10.3908 | 11.0575 | 1.5682 | 2.4298 | 0.3219 | 1.1342 | 0.1471 | 0.0395 | 0.0796 |

**Table 33: Trace element composition of the fluids that result from my models, for Northern Vanuatu.**

| Fluids | Dy, ppm | Y, ppm | Ho, ppm | Er, ppm | Tm, ppm | Yb, ppm | Lu, ppm | Th, ppm | U, ppm | Zr, ppm | Hf, ppm |
|---|---|---|---|---|---|---|---|---|---|---|---|
| **1st** | 0.02191 | 0.32611 | 0.00395 | 0.01393 | 0.00151 | 0.00869 | 0.00143 | 0.00081 | 0.00515 | 0.14609 | 0.00391 |
| **2nd** | 0.02244 | 0.34539 | 0.00404 | 0.01423 | 0.00155 | 0.00883 | 0.00147 | 0.00092 | 0.00557 | 0.16654 | 0.00439 |
| **3rd** | 0.02296 | 0.36453 | 0.00413 | 0.01448 | 0.00158 | 0.00897 | 0.00150 | 0.00104 | 0.00601 | 0.18933 | 0.00492 |
| **4th** | 0.02348 | 0.38368 | 0.00422 | 0.01470 | 0.00161 | 0.00909 | 0.00153 | 0.00118 | 0.00650 | 0.21476 | 0.00552 |
| **5th** | 0.02399 | 0.40283 | 0.00431 | 0.01488 | 0.00164 | 0.00921 | 0.00156 | 0.00134 | 0.00702 | 0.24304 | 0.00617 |
| **6th** | 0.02454 | 0.42195 | 0.00441 | 0.01506 | 0.00167 | 0.00933 | 0.00158 | 0.00151 | 0.00760 | 0.27449 | 0.00689 |
| **7th** | 0.02507 | 0.44098 | 0.00451 | 0.01520 | 0.00170 | 0.00944 | 0.00161 | 0.00171 | 0.00821 | 0.30916 | 0.00767 |
| **8th** | 0.02561 | 0.45990 | 0.00461 | 0.01533 | 0.00173 | 0.00954 | 0.00163 | 0.00193 | 0.00888 | 0.34731 | 0.00851 |
| **9th** | 0.02613 | 0.47871 | 0.00471 | 0.01542 | 0.00175 | 0.00964 | 0.00165 | 0.00217 | 0.00961 | 0.38898 | 0.00941 |
| **10th** | 0.02661 | 0.49709 | 0.00480 | 0.01548 | 0.00177 | 0.00971 | 0.00166 | 0.00243 | 0.01040 | 0.43391 | 0.01033 |
| **11th** | 0.02702 | 0.48526 | 0.00488 | 0.01539 | 0.00177 | 0.00973 | 0.00166 | 0.00271 | 0.01130 | 0.47121 | 0.01141 |
| **12th** | 0.02768 | 0.52274 | 0.00500 | 0.01552 | 0.00180 | 0.00986 | 0.00168 | 0.00314 | 0.01247 | 0.53766 | 0.01290 |
| **13th** | 0.02829 | 0.53071 | 0.00512 | 0.01554 | 0.00182 | 0.00994 | 0.00169 | 0.00365 | 0.01382 | 0.59846 | 0.01469 |
| **14th** | 0.02915 | 0.54930 | 0.00528 | 0.01567 | 0.00185 | 0.01009 | 0.00171 | 0.00435 | 0.01768 | 0.67619 | 0.01708 |
| **15th** | 0.03432 | 0.56639 | 0.00625 | 0.01737 | 0.00211 | 0.01144 | 0.00191 | 0.00664 | 0.02515 | 0.95521 | 0.02486 |
| **16th** | 0.03929 | 0.58475 | 0.00717 | 0.01910 | 0.00236 | 0.01276 | 0.00212 | 0.00890 | 0.03222 | 1.22350 | 0.03236 |
| **17th** | 0.04077 | 0.58901 | 0.00745 | 0.01942 | 0.00242 | 0.01307 | 0.00216 | 0.01028 | 0.03571 | 1.35974 | 0.03659 |
| **18th** | 0.04313 | 0.59666 | 0.00790 | 0.02013 | 0.00253 | 0.01365 | 0.00225 | 0.01190 | 0.03997 | 1.52687 | 0.04160 |
| **19th** | 0.04555 | 0.60427 | 0.00836 | 0.02084 | 0.00264 | 0.01423 | 0.00233 | 0.01378 | 0.04461 | 1.71191 | 0.04726 |
| **20th** | 0.04805 | 0.61181 | 0.00883 | 0.02154 | 0.00276 | 0.01482 | 0.00242 | 0.01598 | 0.04964 | 1.91657 | 0.05366 |
| **21st** | 0.05062 | 0.61924 | 0.00931 | 0.02223 | 0.00287 | 0.01541 | 0.00251 | 0.01853 | 0.05506 | 2.14202 | 0.06087 |
| **22nd** | 0.05338 | 0.62736 | 0.00984 | 0.02298 | 0.00299 | 0.01605 | 0.00260 | 0.02152 | 0.06097 | 2.39391 | 0.06909 |
| **23rd** | 0.05585 | 0.63355 | 0.01031 | 0.02356 | 0.00309 | 0.01657 | 0.00268 | 0.02498 | 0.06707 | 2.65924 | 0.07813 |
| **24th** | 0.06161 | 0.64882 | 0.01140 | 0.02495 | 0.00333 | 0.01781 | 0.00285 | 0.03385 | 0.08079 | 3.28693 | 0.10013 |

**Table 21: Continuation.**

| Fluids | Nb, ppm | Ta, ppm | Pb, ppm | Be, ppm |
|---|---|---|---|---|
| **1st** | 0.00047 | 0.00004 | 0.01784 | 0.00075 |
| **2nd** | 0.00069 | 0.00004 | 0.02002 | 0.00115 |
| **3rd** | 0.00102 | 0.00005 | 0.02251 | 0.00177 |
| **4th** | 0.00148 | 0.00006 | 0.02541 | 0.00273 |
| **5th** | 0.00212 | 0.00007 | 0.02884 | 0.00424 |
| **6th** | 0.00297 | 0.00009 | 0.03288 | 0.00659 |
| **7th** | 0.00410 | 0.00011 | 0.03782 | 0.01032 |
| **8th** | 0.00554 | 0.00013 | 0.04394 | 0.01622 |
| **9th** | 0.00732 | 0.00015 | 0.05178 | 0.02568 |
| **10th** | 0.00948 | 0.00018 | 0.06223 | 0.04087 |
| **11th** | 0.01203 | 0.00022 | 0.07494 | 0.06368 |
| **12th** | 0.01551 | 0.00026 | 0.09417 | 0.09981 |
| **13th** | 0.01979 | 0.00032 | 0.11949 | 0.15028 |
| **14th** | 0.02670 | 0.00040 | 0.02602 | 0.41033 |
| **15th** | 0.04628 | 0.00074 | 0.05057 | 0.49882 |
| **16th** | 0.06583 | 0.00114 | 0.07163 | 0.56804 |
| **17th** | 0.07798 | 0.00138 | 0.11163 | 0.60193 |
| **18th** | 0.09173 | 0.00169 | 0.14739 | 0.63915 |
| **19th** | 0.10725 | 0.00206 | 0.19836 | 0.67801 |
| **20th** | 0.12461 | 0.00249 | 0.27245 | 0.71865 |
| **21st** | 0.14385 | 0.00301 | 0.38558 | 0.76127 |
| **22nd** | 0.16503 | 0.00362 | 0.52757 | 0.80666 |
| **23rd** | 0.18809 | 0.00432 | 0.93022 | 0.85361 |
| **24th** | 0.23993 | 0.00612 | 2.56524 | 0.95843 |

**Table 21: Continuation.**